GRØNLANDS GEOLOGISKE UNDERSØGELSE
Bulletin No. 152

Reaction between picrite magma and continental crust: early Tertiary silicic basalts and magnesian andesites from Disko, West Greenland

by

Asger Ken Pedersen

KØBENHAVN 1985

Grønlands Geologiske Undersøgelse

(The Geological Survey of Greenland)

Øster Voldgade 10, DK-1350 Copenhagen K

Bulletins

No. 138 Silurian stratigraphy and facies distribution in Washington Land and western Hall Land, North Greenland. 1980 *by* J. M. Hurst. D.kr. 120.00

No. 139 Triassic lithostratigraphy of East Greenland between Scoresby Sund and Kejser Franz Josephs Fjord. 1980 *by* L. B. Clemmensen. D.kr. 53.00

No. 140 Upper Pleistocene and Holocene marine deposits and faunas on the north coast of Nûgssuaq, West Greenland. 1981 *by* Leifur A. Símonarson. D.kr. 160.00

No. 141 Dresbachian trilobites and stratigraphy of the Cass Fjord Formation, western North Greenland. 1981 *by* A. R. Palmer & J. S. Peel. D.kr. 90.00

No. 142 Silurian graptolites from Washington Land, western North Greenland. 1981 *by* M. Bjerreskov. D.kr. 112.00

No. 143 Stratabound copper-lead-zinc mineralisation in the Permo-Triassic of central East Greenland. 1982 *by* B. Thomassen, L. B. Clemmensen & H. K. Schønwandt. D.kr. 90.00

No. 144 Upper Jurassic bivalves from Milne Land, East Greenland. 1982 *by* F. T. Fürsich. D.kr. 205.00

No. 145 Stratigraphy of the Silurian turbidite sequence of North Greenland. 1982 *by* J. M. Hurst & F. Surlyk. D.kr. 280.00

No. 146 Paleocene gastropods from Nûgssuaq, West Greenland. 1983 *by* H. A. Kollmann & J. S. Peel. D.kr. 280.00

No. 147 The stratigraphy of the Upper Jurassic and Lower Cretaceous sediments of Milne Land, central East Greenland. *by* T. Birkelund, J. H. Callomon & F. T. Fürsich. D.kr. 106.00

No. 148 Upper Ordovician and Silurian carbonate shelf stratigraphy, facies and evolution, eastern North Greenland. 1984 *by* J. M. Hurst. D.kr. 125.00

No. 149 Benthic macroinvertebrate associations from the Boreal Upper Jurassic of Milne Land, central East Greenland. 1984 *by* F. T. Fürsich. D.kr 135.00

No. 150 Stratigraphy and structure of the Fiskenæsset Complex, southern West Greenland. 1985 *by* J. S. Myers. D.kr. 200.00

No. 151 The geology of the Qôrqut granite complex north of Qôrqut, Godthåbsfjord, southern West Greenland. 1985 *by* C. R. L. Friend, M. Brown, W. T. Perkins & A. D. M. Burwell. D.kr. 155.00

No. 152 Reaction between picrite magma and continental crust: early Tertiary silicic basalts and magnesian andesites from Disko, West Greenland. 1985 *by* A. K. Pedersen.

Bulletins up to no. 114 were also issued as parts of *Meddelelser om Grønland,* and are available from Nyt Nordisk Forlag – Arnold Busck, Købmagergade 49, DK–1150 Copenhagen K, Denmark.

GRØNLANDS GEOLOGISKE UNDERSØGELSE
Bulletin No. 152

Reaction between picrite magma and continental crust: early Tertiary silicic basalts and magnesian andesites from Disko, West Greenland

by

Asger Ken Pedersen

1985

Abstract

The Kûgánguaq Member is a lava and tuff sequence comprising about 7.5 km^3 of magnesian silicic basalts (92%), magnesian andesites (7%) and feldspar-phyric silicic basalts (< 1%) found in the middle part of the predominantly picritic Vaigat Formation of lower Tertiary age in northern Disko. The Kûgánguaq Member rocks contain high normative orthopyroxene and usually abundant modal low-Ca pyroxene while modal Fe-Ti oxides are very sparse. The rocks show chemical similarities to boninites and to high-Mg continental dolerites. Comparison with regional picritic to olivine-poor tholeiitic basalts from the Vaigat Formation reveals that the Kûgánguaq Member rocks were derived from picritic parents (MgO > 18%) through reaction with crustal rocks, presumably Cretaceous sand or siltstones. The reaction led to sulphide fractionation and to magma modification which cannot be explained in terms of crystal fractionation or by simple mixing between magma and contaminants.

The transition element (Fe, Ti, V and Cr) concentrations in rocks, glasses and minerals indicate that the Kûgánguaq Member rocks equilibrated at oxygen fugacities several orders of magnitude below the FMQ buffer, but above the IW-buffer. The partitioning of vanadium between olivine and glass and between chromite and glass shows particularly large variations and appears to be the most sensitive recorder of f_{O_2} variations in the range between the FMQ and IW buffers at high igneous temperatures.

Author's address:
Asger Ken Pedersen
Geologisk Museum
Øster Voldgade 5–7
DK-1350 København K

CONTENTS

INTRODUCTION

The lower Tertiary volcanic province of West Greenland is particularly notable for its large volumes of picritic volcanic rocks (Clarke & Pedersen, 1976) and for its contaminated and strongly reduced volcanic rocks which share many features with extratelluric materials (see Bøggild, 1953; Pauly, 1969; Pedersen, 1975, 1981).

In the Disko and Nûgssuaq regions (fig. 1) the early volcanic sequence – the Vaigat Formation (Hald & Pedersen, 1975; Pedersen, 1985) – is largely composed of picritic lavas and hyaloclastites with minor interlayered sequences of contaminated lavas. The lavas formed as the result of major geotectonic processes leading to crustal foundering in the Baffin Bay region (e.g. Clarke & Upton, 1971; Van der Linden, 1975; Henderson *et al.*, 1981).

The magmatism was preceded by graben formation and accumulation of up to several kilometres of Mesozoic to early Tertiary sediments (Henderson *et al.*, 1976, 1981). As the volcanism progressed increasing igneous diversification took place (Clarke & Pedersen, 1976), but in the early stages of activity, corresponding to the lower part of the Vaigat Formation, the magmatism seems to have been very simple: primitive mantle-derived picritic melts low in LIL elements ascended rapidly through a continental crust composed of a Precambrian substratum and a cover of Mesozoic to early Tertiary sediments.

Most of the volcanic products were not notably affected by reaction with the crust and were erupted as picritic basalts and subordinate olivine-poor tholeiitic basalts derived from picrite magma by removal of olivine at low pressures.

A minor amount of the melt, however, reacted with the crust and formed contaminated sequences composed of silicic basalts and magnesian andesites. At least six contaminated sequences are known from the Vaigat Formation on Disko, while many poorly known occurrences are present on Nûgssuaq (e.g. Pedersen, 1978a). Some contaminated sequences contain extremely reduced basalts and andesites with metallic iron and graphitic pyrometamorphosed shale xenoliths, as described from the Asuk Member (Pedersen, 1978b, 1979a, 1985). However, most of the contaminated rocks are poor in xenoliths and cannot give direct information as to the nature of the contaminants, except that these contained insufficient reducing components to allow the precipitation of metallic iron (or the magmas became oxidized prior to eruption). In order to be able to characterize all these rocks in terms of their predominant contaminants, the best exposed and most variable iron-free contaminated lava sequence in the Vaigat Formation has been selected for a detailed study; this is a minor volcanic system on Disko, formalized as the Kûgánguaq Member (Pedersen, 1985).

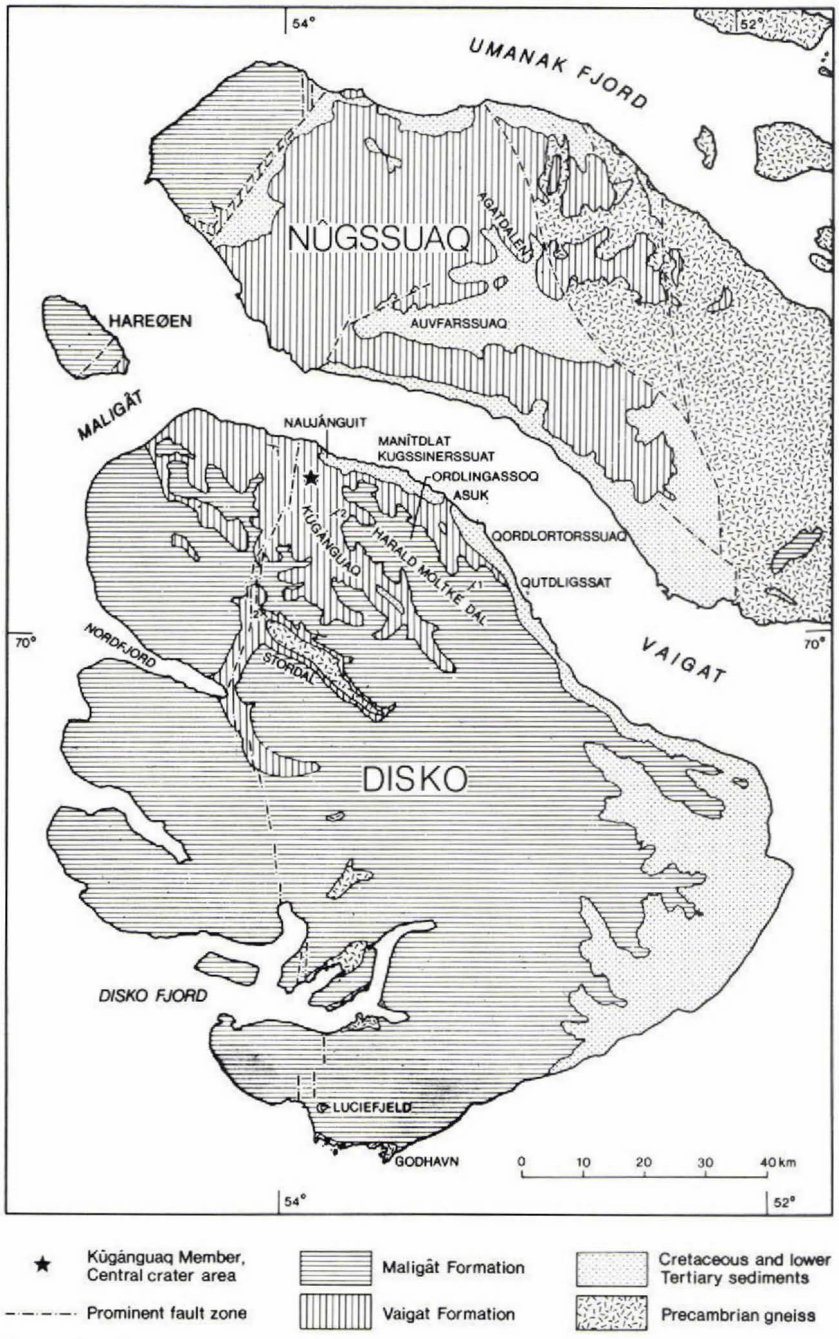

Fig. 1. Generalized geological map of Disko and Nûgssuaq. Type localities for the members of the Vaigat Formation are shown together with the Kûgánguaq Member central crater area.

The Kûgánguaq Member rocks were derived when picritic parents reacted with the crust and exemplify empirically the formation of andesitic rocks by that process. The rocks do not carry metallic iron, but are nevertheless distinctly reduced compared to the normal rocks produced by the regional Vaigat Formation volcanism. For this reason the Kûgánguaq Member rocks offer a rare opportunity to study the behaviour of the lithophile transition metal elements in natural rocks in the range of oxygen fugacities between the FMQ and IW f_{O_2} buffers at high igneous temperatures. Therefore the paper will focus on the characterization of ferromagnesian silicates and oxides and the glass phases in the Kûgánguaq Member rocks.

In order to characterize the igneous environment of the regional volcanism this study also includes the first descriptions of picrite glass rocks from Disko.

The present paper on silicic basalts and magnesian andesites from the Kûgánguaq Member forms part of the current investigation on Disko and Nûgssuaq of the contaminated volcanic rocks and their xenoliths, with particular emphasis on their unusual and strongly reduced igneous and pyrometamorphic character.

Earlier papers have dealt with xenolithic material from the extremely reduced volcanic rocks from the Asuk Member (Pedersen, 1978b, 1979a); with the less reduced iron-bearing graphitic magnesian andesite and basalt tuffs from the Abraham Member on Nûgssuaq (Pedersen, 1978a); with the slightly iron-bearing basaltic dyke glass at Luciefjeld (Pedersen, 1979b) and with the iron-bearing andesitic to dacitic lavas with their unusual lunar-like oxide mineralogies from the Maligât Formation of north-west Disko (Pedersen, 1981).

GEOLOGICAL SETTING

A subdivision of the Vaigat Formation into members (fig. 2) was presented by Pedersen (1985). Briefly, the Vaigat Formation volcanism seems to record two major thermal events. The first event led to regional picritic volcanism (Naujánguit Member) with olivine-poor tholeiitic basalts in its waning stage (Qordlortorssuaq Member). A temporary decline of volcanism then led to a widespread transgression. The second thermal event again produced regional picritic volcanism (Ordlingassoq Member), including minor alkaline basaltic lavas. A separate sequence of alkaline basaltic rocks within the Ordlingassoq Member has been formalized as a separate member (Manîtdlat Member).

Two distinctive volcanic systems, each consisting of silicic basalts and magnesian andesites, were formed in the first thermal event and have been formalized as the older Asuk Member, which contains metallic iron, and the younger Kûgánguaq Member, which does not contain metallic iron.

The Kûgánguaq Member volcanics are continuously exposed in the steep and deeply dissected lava plateau in the northern part of the Kûgánguaq valley (fig. 3) and can be followed in the coastal mountains to Manîtdlat kugssinerssuat. Considerable parts of the exposures are inaccessible. Parts of the central eruption area were removed when the Kûgánguaq valley was carved out in the basalt plateau.

The Kûgánguaq Member comprises about 7.5 km^3 of lavas and tuffs which cover an area of about 200 km^2 along the north coast of Disko (fig. 4b). The Kûgánguaq Member lies on top of a regular sequence of picritic pahoehoe lavas, which form

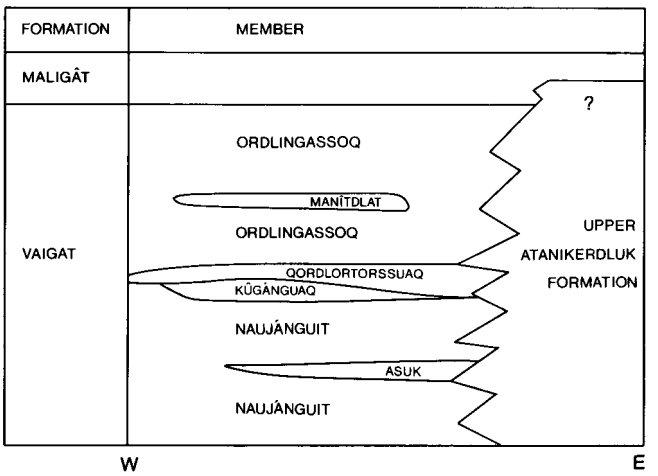

Fig. 2. Lithostratigraphic scheme of the Vaigat Formation on Disko, from Pedersen (1985).

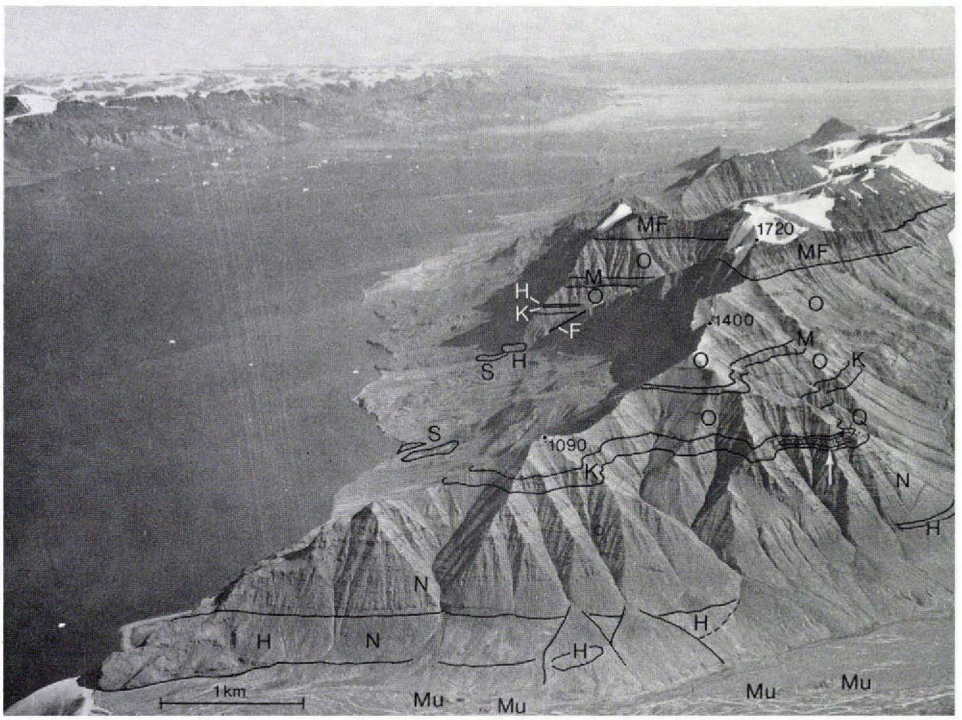

Fig. 3. Oblique aerial photograph of the central crater area of the Kûgánguaq Member in the north-eastern part of Kûgánguaq valley seen from the west. The north coast of Disko and Vaigat are seen to the left with Nûgssuaq in the background. The tuff shield in the Kûgánguaq Member is marked by the white arrow and by a stippled signature. The photo covers the type areas for the lower part of the Vaigat Formation and for the Naujánguit and Kûgánguaq Members. H: hyaloclastite, N: Naujánguit Member, K: Kûgánguaq Member, Q: Qordlortorssuaq Member, M: Manîtdlat Member, O: Ordlingassoq Member, MF: Maligât Formation, F: Feeder dyke in the Kûgánguaq Member, S: Cretaceous sandstone, Mu: Mud volcano. Copyright Geodætisk Institut, Denmark, published with permission A.695/79.

the top of the Naujánguit Member in this area, and is covered partly by the Qordlortorssuaq Member basalts, and partly by picritic lavas and hyaloclastites from the Ordlingassoq Member. Most of the Kûgánguaq Member volcanic rocks were erupted from within a small area in the eastern side of Kûgánguaq valley, just north of the entrance to Harald Moltke Dal.

The central eruption area is situated just east of an irregular, north–south, major fault zone which extends roughly 120 km from Kûgánguaq in the north to the south coast of Disko (fig. 1).

The fault, which cuts through all the exposed Tertiary rocks, separates downthrown areas to the west from a stable, subhorizontal, plateau to the east.

A few kilometres north of the eruptive centre, coastal exposures of the pre-volcanic basement of Cretaceous sediments (fig. 1) have revealed an old escarpment

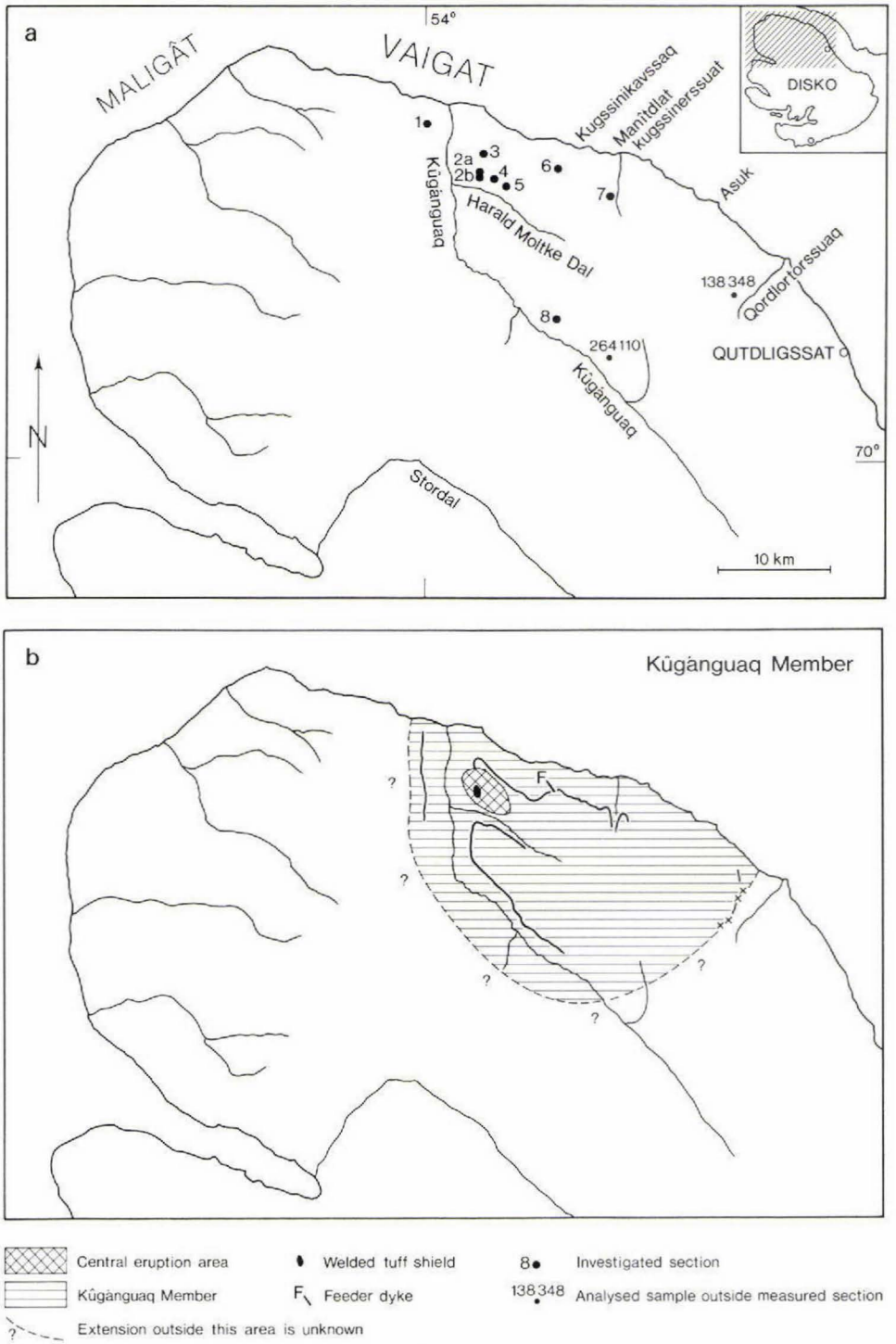

Fig. 4. a: Investigated localities for Kûgânguaq Member rocks on the northern part of Disko. The single numbers refer to sections shown in fig. 5. The six figure (GGU) numbers show the locations of a few individual samples for which only brief information is given in the text. b: Areal extent of the Kûgânguaq Member.

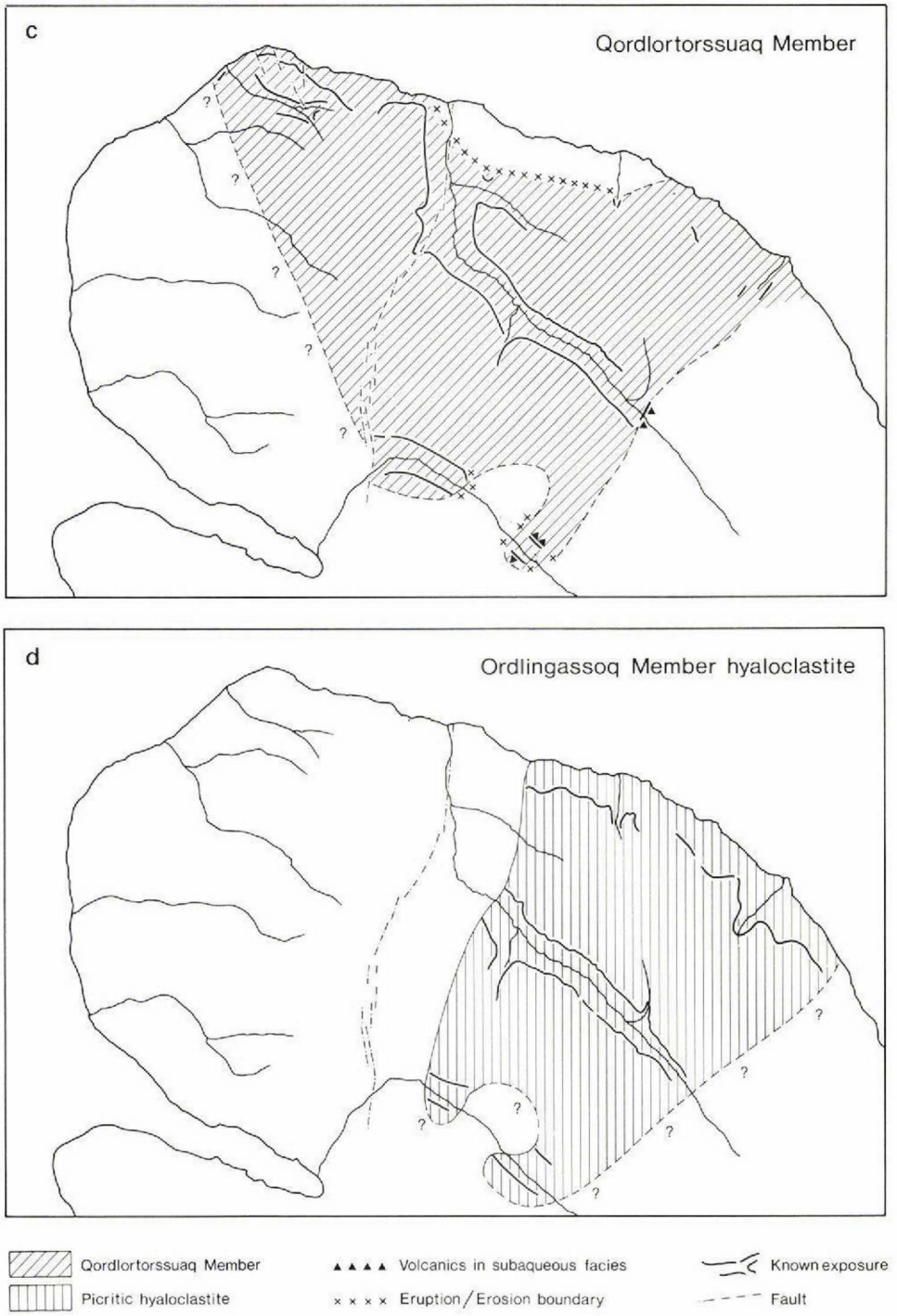

Fig.4 *cont.* c: Areal extent of the Qordlortorssuaq Member, d: Areal extent of hyaloclastites from the base of the Ordlingassoq Member.

more than 300 m high with the low-lying areas towards the west (Pedersen, 1973). This is taken to indicate that large-scale fault movements were also active prior to the onset of volcanism. Detailed mapping of the distribution of volcanic marker horizons in areas covered by the Kûgánguaq Member (Pedersen, 1973; GGU, 1976) has demonstrated large-scale movements during the volcanism (relative to the palaeo-sea level). These movements are best described as combined down-sagging and gradual tilting of a large block towards the south-east.

It is highly probable that this large structure controlled the location of the eruptive sites for the Kûgánguaq Member volcanism.

Substratum to the Kûgánguaq Member

Precambrian amphibolite facies gneisses and amphibolites are exposed from southern to central Disko (fig. 1). These are known as the Disko Gneiss Ridge which, according to seismic data, continues northwards at a depth of less than 500 m into a limited area south of the entrance of Auvfarssuaq valley on Nûgssuaq (Elder, 1975). The Kûgánguaq Member crater area is situated about 5 to 10 km to the east of the supposed extension of the Disko Gneiss Ridge between Nûgssuaq and the northernmost gneiss exposures on Disko, found in Stordal.

Cretaceous sandstone and minor carbonaceous shales from the Atane Formation (Henderson *et al.*, 1976) are exposed a few kilometres north of the central crater area, just below the Vaigat Formation rocks. There are about 300 m of sediments present above sea level and as they extend at least down to the deepest part of the Vaigat north of Kûgánguaq (– 565 m, Denham, 1974) they must be at least 900 m thick.

Depending on the prevolcanic topography, the Kûgánguaq Member crater area is underlain by between 450 and 700 m of predominantly picritic lavas and minor hyaloclastite breccias of the Naujánguit Member.

VOLCANIC LITHOLOGY

The Kûgánguaq Member eruption products form an irregular shield which thins gradually towards the south but rapidly towards the north and north-west, because the magma erupted on a subhorizontal plane of picritic pahoehoe lavas, which slowly sagged towards the south-east. The Kûgánguaq Member deposits now reach a thickness of only 90 m, but the tops of some crater structures were eroded before they were inundated by younger picritic lavas. A number of detailed sections (fig. 5) and some photographs (figs 6 to 8) illustrate the volcanic lithology of the Kûgánguaq and Qordlortorssuaq Members. Only the central eruption area and a feeder dyke location, with associated lavas, will be described in some detail.

Central eruption area

The central eruption area around 70°12′40″N, 53°51′50″W at the junction between Kûgánguaq and Harald Moltke Dal covers an area of roughly 20 km^2 (fig. 4b) and is represented by sections 2a, 2b, 3, 4 and 5 in fig. 5. Everywhere a decimetre thick layer of red bole on top of the underlying picritic lavas marks a temporary decline in volcanic activity just prior to the Kûgánguaq Member volcanism.

Five units, A to E, some of which have only a limited areal extent, are found above the red bole. A: about 20 m of thin olivine microporphyritic basalt lavas. B: a shield-like crater structure composed of several units of basaltic welded tuffs. This unit extends to the top of the Kûgánguaq Member in some areas. C: up to 40 m of olivine microporphyritic basalt lavas, very similar to unit A, overlie unit B in the northern and eastern part of the area. They will not be described separately. D: thick and irregular, blocky, magnesian andesite lavas with an andesite tuff on top. E: a few flows of feldspar-phyric silicic basalt.

A single feldspar-phyric basalt lava from the Qordlortorssuaq Member occurs above the Kûgánguaq Member in the southern part of the central area, whereas picrite lavas form the cover in the northern part (fig. 6).

Olivine microporphyritic basalt lavas (units A and C)

This oldest unit is composed of five olivine microporphyritic basaltic aa lava flows, varying in thickness from 1.5 to 3 m and with a total thickness of 12 to 15 m. They are characterized by light grey-brown weathering colours. On top of these

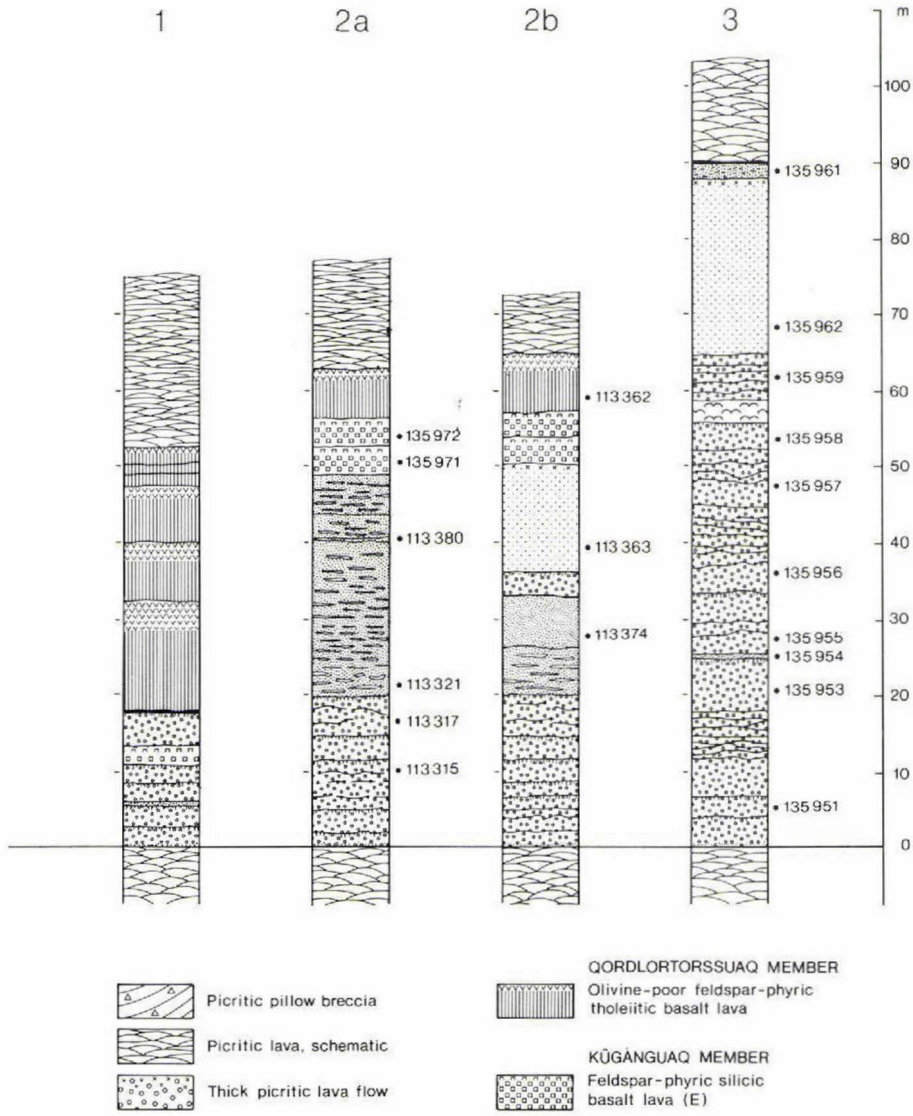

Fig. 5. Sections through the Kûgánguaq Member at the localities shown in fig. 4a from the northern part of Disko. Heights are given relative to the base of the Kûgánguaq Member.

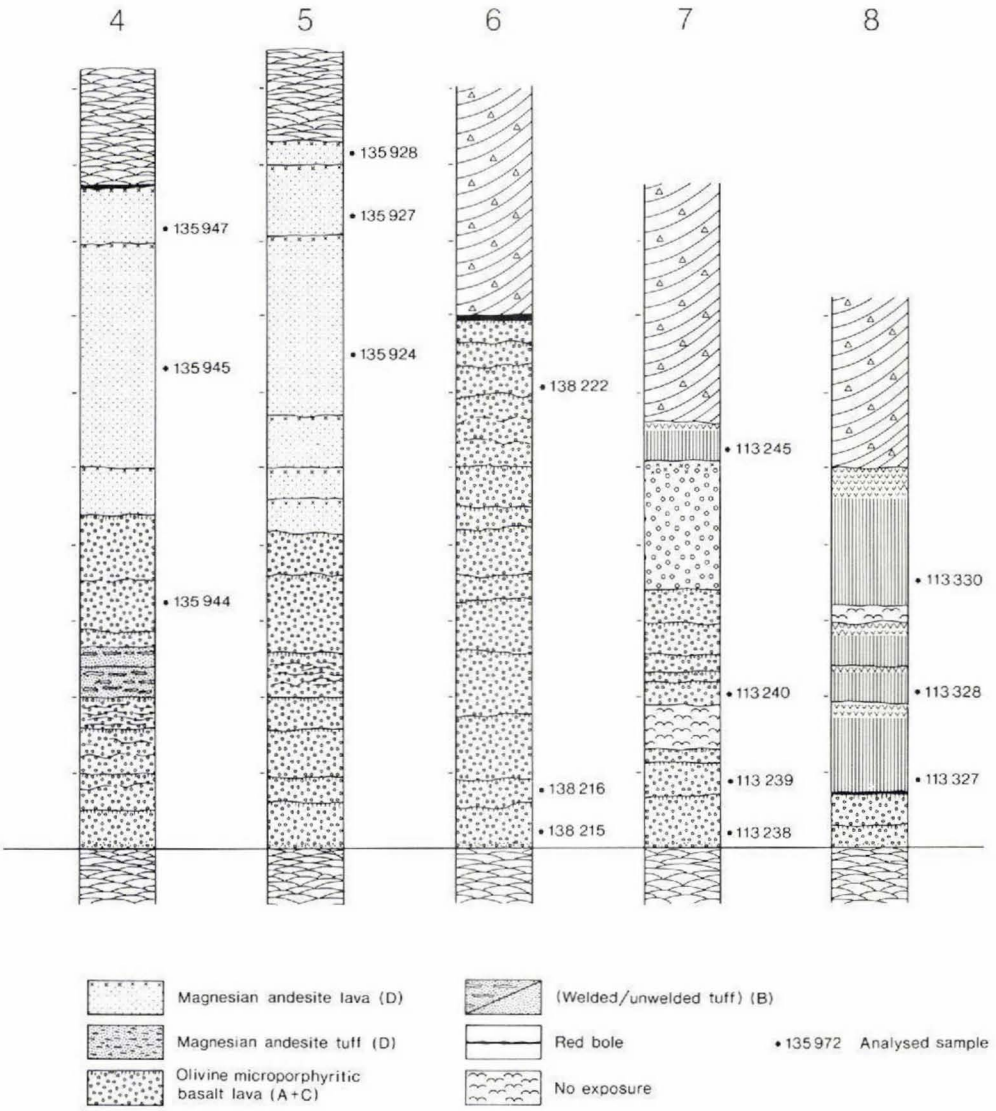

Fig. 5 *cont.* The position of the analysed samples is indicated on the sections, and their coordinates are given in Tables 15, 17, 18 and 19. For A–E see text.

Fig. 6. Section 3 (fig. 5) in the Kûgánguaq Member in the northern part of the central crater area. A and C: olivine microporphyritic basalt lava, B: basalt tuff from the unit which a few kilometres further south forms the tuff shield, D: magnesian andesite lava covered by T: andesite tuff. The Kûgánguaq Member is directly overlain by P: picrite lavas in this area.

lavas rests a 5 m thick olivine microporphyritic basalt flow consisting of lava tongues and pillow-like bodies. Both grain size and vesiculation vary strongly in this lava, and numerous tiny pegmatitic patches are developed.

Welded basalt tuffs (unit B)

This volcanic sequence is described in detail because of its unusual nature. The welded tuffs build up a shield-like body which covers an area of roughly 300 by 500 m. Outside this area the tuffs decrease in thickness from several metres to less than one decimetre, and cover an area of 10 km^2 surrounding the central body. Its intense red oxidation colours can be observed from distances of more than 30 km, but by volume it constitutes no more than about 0.005 to 0.01 km^3, accounting for

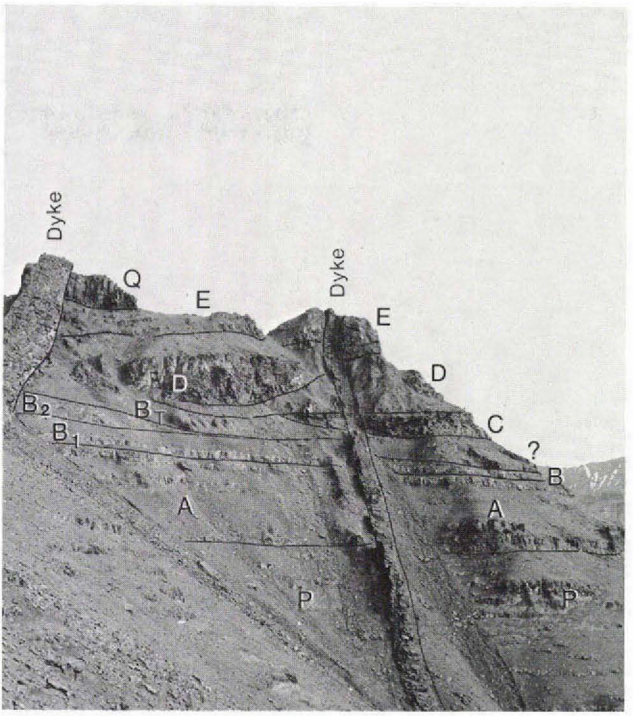

Fig. 7. Section 2b (fig. 5) in the Kûgánguaq Member in the southern part of the central crater area as seen from the north. P: picrite lava, A and C: olivine microporphyritic basalt lava, B_1 and B_2: lower and upper units in the basaltic tuff shield, B_T: a separate olivine microporphyritic basalt tuff unit which is partly of phreatic origin. D: magnesian andesite lava; the flow to the right is highly scoriaceous, E: feldspar-phyric silicic basalt lava, Q: Qordlortorssuaq Member basalt lava.

only a very small proportion of the Kûgánguaq Member volcanics. The shield centre marks an eruption site, but no feeder dyke or neck has yet been found. The welded tuff comprises two units which must have been emplaced within a very short span of time.

The lower unit (figs 8 to 10) which is up to 30 to 40 m thick, was deposited on the crumbling scoria-top of the uppermost of the unit A lavas (olivine microporphyritic basalt). The basal 30 to 40 cm of the tuff consist of red unwelded tuff with a particle size range from dust to lapilli. The particles are achneliths (Walker & Croasdale, 1973), which are fine-vesiculated and generally have smooth sphaeroidal forms. They are mostly black to dark grey in the cores and have a red-oxidized surface. From the base upwards the degree of welding increases rapidly, and the droplets become glassy and enclosed in red welded tuff. Some 30 to 40 cm upwards from the base the tuff has become a columnarly-jointed basaltic glassy rock (fig. 8a) with a bluish grey colour. The glass zone (3 m) shows a very distinct subhorizontal layering, indicated by slightly varying oxidation colouring, while flow-fold patterns are absent. Rounded inclusions, which reach a size of a few centimetres and are common in the glass layer, consist of partially melted sandstone xenoliths with very abundant carbonate-filled vesicles.

Oxidation becomes more pronounced in the upper part of the glass layer, and

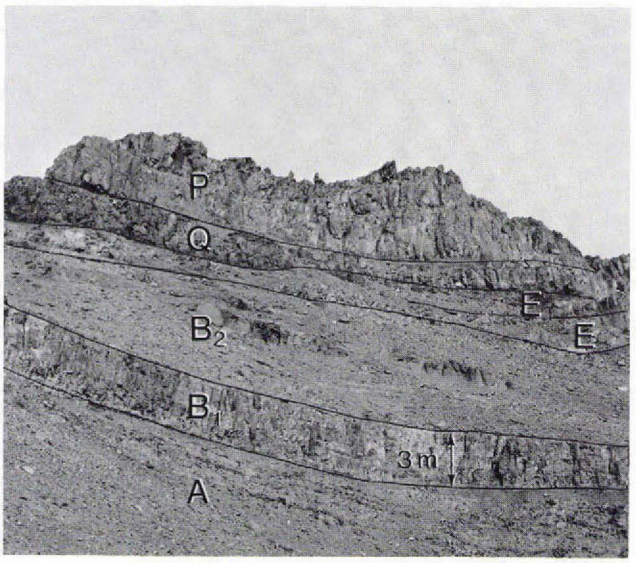

Fig. 8. a: Section just south of the central part of the basaltic tuff shield. A: olivine microporphyritic basaltic pahoehoe lava. B_1: the basal glassy tuff rock with columnar jointing, shown in detail in fig. 8b. B_2: oxidized less welded fiamme tuff which also includes the upper tuff unit. E: feldspar-phyric silicic basalt lava flows, Q: Qordlortorssuaq Member basalt lava, P: picrite lava from the Ordlingassoq Member.

Fig. 8 *cont.* b: The base of the lower unit in the tuff shield. A: vesiculated upper part of an olivine microporphyritic basalt lava flow, B_1: oxidized achnelith-rich basaltic tuff, unwelded at the base and increasingly welded upwards, B_2: strongly welded glassy basalt tuff with columnar jointing.

there is an upward gradation into highly oxidized, less welded, tuff which constitutes the upper part of the lower tuff unit. Numerous subhorizontal black basaltic 'fiammes', surrounded by oxidized fine-vesicular tuff (fig. 9), occur in this part of the unit.

The glassy layer gradually disappears about 100 to 200 m south of the supposed eruption site, and only a compact achnelith-rich basaltic tuff is found. In an area

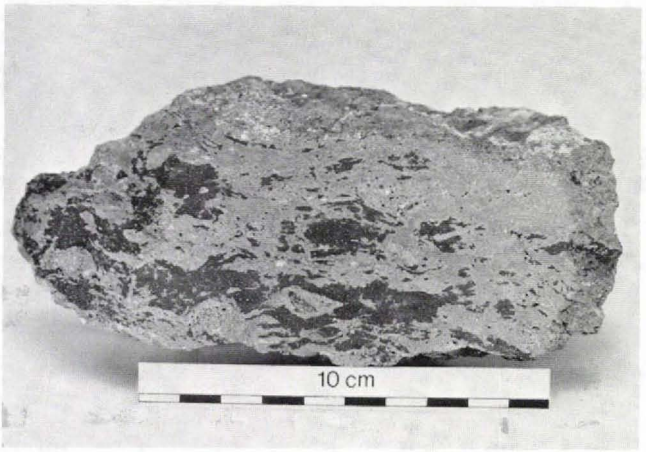

Fig. 9. Basaltic welded tuff with fiamme structure from the uppermost part of the lower tuff unit in the tuff shield. The fiammes are black while the tuff matrix is red. Sample GGU 113379.

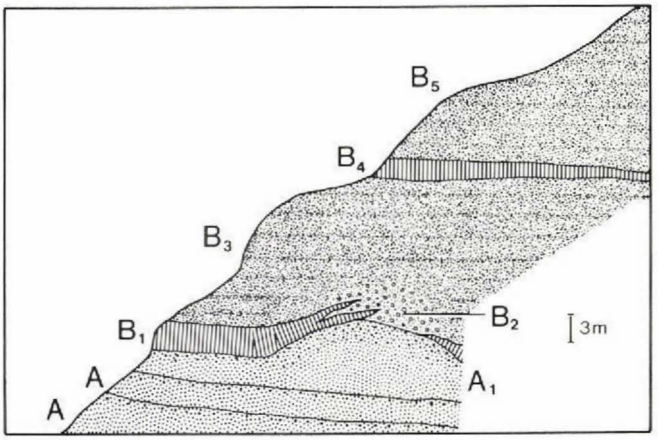

Fig. 10. Section through the central part of the basaltic tuff shield. A: olivine microporphyritic basalt lava. The uppermost of these flows (A_1) forms a local updoming. B_1: intensely welded basalt tuff with columnar jointing which became welded into a glassy rock and then recrystallized to a basaltic hornfels. Where deposited on the lava dome, the tuff welding is less intense and an oxidized less welded fiamme tuff (B_2) was formed. B_3: oxidized basaltic tuff unit. B_4: basaltic hornfels tuff forming the base of the upper tuff unit. B_5: basaltic fiamme tuff from the upper part of the upper tuff unit. Drawn from photograph.

close to the supposed eruption centre, the glassy lower layer has completely recrystallized and appears as an extremely fine-grained olivine microporphyritic basalt with regular columnar jointing. Where this crystalline basalt layer was deposited on local updomings of the underlying lava flow, contact relations clearly show that the basalt was emplaced as a tephra deposit (fig. 10).

The upper unit of welded tuff (10–30 m), which forms a tongue on the northern flank of the crater shield, was deposited directly on the lower tuff unit. Its lower part is a non-vesicular, dense, olivine microporphyritic basalt (strongly welded tuff) which grades upwards, without intrusive contact features, into a red to purple fiamme-textured basaltic welded tuff, very similar to the lower welded tuff unit. The crystalline basalt layer reaches its maximum thickness of more than 10 m

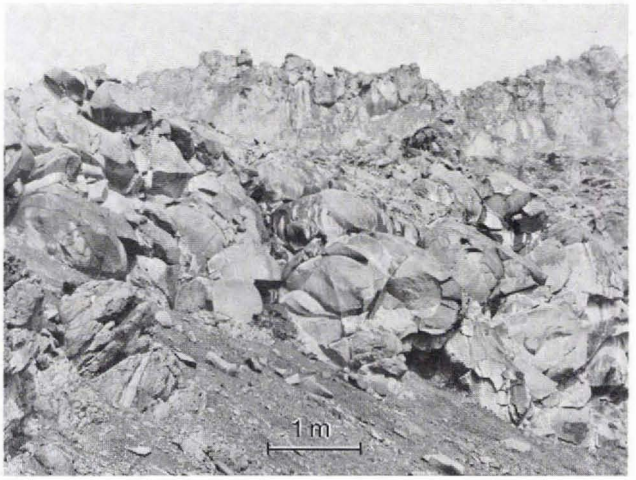

Fig. 11. Magnesian andesite lava with the characteristic sphaeroidal fracture pattern which distinguishes these more silicic rocks from the basalts. From section 5 (fig. 5) in Harald Moltke Dal.

around its supposed centre, which is inaccessible due to topography. The top of the upper welded tuff unit, which is eroded and levelled, is covered by picritic lavas younger than the Kûgánguaq Member in the central part of the crater structure, while the flanks are covered by lavas from units C and D towards the north and units D and E towards the south.

Magnesian andesites (unit D)

Outside the central parts of the welded tuff crater structure, from 1 to 4 magnesian andesite flows are found above the welded tuff level. Their cumulative thickness is up to 45 m (SE of the crater structure), and the individual flows range in thickness from 1 to 25 m. The andesites form blocky aa lavas with piles of highly oxidized massive and scoriaceous inclusions and with very irregular lava surfaces. From a distance these heaps resemble craters, but no specific eruption sites have been identified although most of these lavas must have erupted within the central area. The massive, vesicle-poor, lower parts of the andesite lavas appear as dark grey rocks with a basaltic appearance, but are distinct from most basalts by a characteristic sphaeroidal jointing (fig. 11) and a generally more fine-grained groundmass. Macroscopic xenoliths have not been found, and tuff layers are very subordinate within the magnesian andesite lavas. The largest tuff layer found is a few metres thick, coarse olivine and orthopyroxene-bearing andesite tuff, deposited as the top layer of the Kûgánguaq Member in the northern part of the central eruption area.

Feldspar-phyric silicic basalts (unit E)

The youngest volcanic products from the Kûgánguaq Member are a few feldspar-phyric basaltic lava flows, which overlie magnesian andesites and part of the welded tuff shield in the southern part of the central area. One of these flows has also been recognized on the western side of Kûgánguaq valley, 6 km north-west of the tuff shield.

The lava flows, which are each about 3 to 4 m thick, are characterized by a light yellow-grey weathering colour and contain numerous vesicles, up to decimetre size, which are now partly filled with agate, quartz and calcite. Xenoliths have not been found in these lavas.

Basaltic feeder dyke and its associated lavas

The only known Kûgánguaq Member feeder channel is exposed at Kugssinikavsaq (70°12′10″N, 53°31′36″W) about 5 km east of the central crater area (fig. 3). It is a vertical basaltic dyke from 1.5 to 4 m thick, which strikes NW–SE, following a persistent regional dyke trend (Pedersen, 1977a). At levels more than 80 m below the palaeosurface, the dyke is non-vesicular and appears as an olivine microporphyritic, fine-grained basalt with regular columnar jointing. From about 80 to 20 m below the surface, the dyke becomes gradually more vesicular, grading upwards into a vesiculated heap of scoria, which is strongly oxidized in the top zone. Apart from a scoria pile, which is a few metres thick, there is no crater-like body, and the eruption site is inconspicuous from a distance.

There are about 13 flows here totalling 70 m in thickness (fig. 5, section 6), all of which are olivine microporphyritic basalt with uniform lava morphology. These flows correlate with units A + C in the central crater area. On top of the Kûgánguaq Member is a layer of red bole, a few centimetres thick, which is covered by a picritic hyaloclastite horizon from the Ordlingassoq Member.

GEOLOGICAL SUMMARY

The Kûgánguaq Member volcanism can be briefly summarized as follows.

(1) Just prior to the onset of this volcanic phase northern Disko was a subhorizontal plain covered by picritic pahoehoe lavas, probably erupted from a NW–SE trending fissure system. The surface was slightly weathered and covered by a thin layer of red bole. The lava plateau, which dipped slightly towards the south-east, was limited by a water-filled basin towards the east. Further south, in the Stordal area, weathered gneiss surfaces occurred as 'islands' in the surrounding lava plain.

(2) The Kûgánguaq Member volcanism was initiated by extrusion of olivine microporphyritic basalt lavas which were probably erupted over considerable areas through NW–SE trending fissures.

(3) A minor volcanic centre was established in the northern part of Kûgánguaq, near a persistent N–S trending hinge-structure. Two unusual basaltic welded tuffs were erupted here to form a small tuff shield. This tuff shield represents the largest subaerial tephra deposit yet found within the Vaigat Formation on Disko.

(4) The tuff shield was partly inundated by olivine microporphyritic basalt lavas in the northern parts of the area.

(5) Eruption of magnesian andesitic aa lavas followed in the eastern part of the crater area. The andesite lavas were only accompanied by minor tephra-producing activity.

(6) One or a few feldspar-phyric silicic basalt lavas with estimated origin to the west and south of the central crater area, mark the final Kûgánguaq Member activity. At this stage, parts of the central tuff shield still rose above the surrounding lavas. Subsequent erosion levelled the upper surfaces of these features.

(7) Phenocryst-poor tholeiitic basalts from the Qordlortorssuaq Member were later erupted over parts of the area (fig. 4c).

(8) A temporary decline in igneous activity followed, and a major transgression took place, marked by the extent of the basal hyaloclastite in the overlying Ordlingassoq Member (fig. 4d).

The total volume proportions of the volcanic rocks which make up the Kûgánguaq Member can be roughly estimated as follows.

(1) Olivine microporphyritic basalt lavas and tuffs	92%
(2) Magnesian andesites	7%
(3) Feldspar-phyric silicic basalts	<1%

PETROGRAPHY

Within the Kûgánguaq Member, rock chemistry (Tables 17 to 21) shows that broadly three magma types are present: (1) olivine microporphyritic basalts, (2) magnesian andesites and (3) feldspar-phyric silicic basalts. However, both groundmass texture and mineralogy vary considerably for nearly isochemical rock compositions, indicating that the rocks experienced a diversity of cooling histories. Modal analyses of selected samples are presented in Table 1.

Olivine microporphyritic basalts

These basalts are very uniform in chemical composition and in early phenocryst mineralogy. Most lava samples show groundmass textures typical for igneous rocks while some samples show additional metamorphic features. The tuffaceous rocks have either glassy air-quench ash-textures or are glassy welded tuffs; some are nearly holocrystalline hornfelses.

Lavas and the feeder dyke

Olivine (< 1 mm) is invariably the dominant phenocryst phase, constituting between 4 and 9 vol.% of the rocks, and showing stout and often skeletal morphology. Except for the dyke samples and one lava sample, the olivine is pseudomorphosed to green smectite. When fresh it exhibits normal zoning. In very fine-grained samples (fig. 12a) the olivine is not rimmed by other phases, whereas in coarser rocks it tends to be resorbed and rimmed by ortho- or clinopyroxene.

Brown chromite octahedra, occasionally reaching 0.06 mm in size, are found as inclusions in olivine as well as in groundmass plagioclase and pyroxene. Where in contact with residuum they are distinctly zoned (Table 8 nos 1 to 4) and have opaque rims of chromian titanomagnetite (fig. 13a). The modal abundance varies from 0.05 to 0.019 vol.% with the higher values in samples with much groundmass-equilibrated chromite.

A few flows carry traces of microphenocrystic plagioclase and/or orthopyroxene which always constitute less than 1 vol.%.

The groundmass is composed of pyroxene, plagioclase, Fe-Ti oxides and residuum, with traces of silica, carbonate, zeolites, late sheet silicates and sulphides. In fine-grained groundmasses, pigeonite and subcalcic augite predominate greatly over orthopyroxene, whereas coarser grained rocks (fig. 12b) show up to 20 vol.% orthopyroxene, often mantled by pigeonite or subcalcic augite.

Table 1. Modal analyses of volcanic rocks from the Kûgánguaq Member

Rock type	Olivine microporphyritic basalt						Magnesian andesite									Feldspar-phyric silicic basalt
	Feeder dyke	Lavas					Welded tuffs			Pillow Lavas						Lava
GGU No.	138229	135951	135953	135955	135956	135958	113321	135975	113380	264110	113363	135927	135945	135924	135962	135972
In vol. % *Phenocrysts*	7	5.5	4.5	8.5	5.0	5.0	9.0	8.5	7.5	9.5	18.5	18.5	0.5¶	20.5	26.5	9.0
Olivine	5.0						1.7		1.0	9.5					0.5	
Olivine pseudomorphs	2.0	5.5	4.5	8.5	5.0	5.0	7.3	7.5	3.0		2.0	1.5	0.5	2.0	2.0	tr.
Orthopyroxene			tr.			tr.					16.0	17.0	¶	18.0	22.0	tr.
Clinopyroxene								1.0‡	3.5‡							tr.
Plagioclase		tr.									0.5	tr.	¶	0.5	2.0	9.0
Chromite*	0.10	0.05	0.05	0.19	0.07	0.07	0.06	0.13	0.15	0.15	<0.01	tr.	tr.	tr.	<0.01	0.01
Groundmass																
Total pyroxene in groundmass	29.0	37.5	35.5	32.0	32.5	34.0			38.0	tr.	14.0	12.5	25.5¶	13.5	14.0	29.5
Orthopyroxene		13.5	20.0	tr.	17.0	18.0$							19.5			
Clinopyroxene	29.0	24.0	15.5	32.0	15.5	16.0	tr.						6.0			29.5
Plagioclase	45.0	41.0	43.0	43.0	43.0	45.0	tr.		50.0	tr.	33.0	43.0	38.0¶	37.0	41.0	37.5
Very fine-grained groundmass or glass							87.0	90.0		88.0						
Residuum†	15.0	8.0	11.5	10.0	7.0	6.5			0.5		22.5	20.5	23.5	25.0	17.0	13.5
Fe-Ti oxides	0.45	1.1	0.8	0.95	0.95	1.3			0.80		0.35	0.07	0.60	0.12	0.60	2.0
Late subsolidus oxides			<0.01	0.04	0.10	0.03										
Silica		tr.				tr.			tr.		7.5	2.5	9.0	tr.		0.5
Late sheet silicate	1.0	6.0	4.0	5.0	11.5	8.0	4.0	1.5	2.5	2.0	4.0	2.5	2.5	3.0	1.0	8.0
Carbonate	2.0															tr.
Sulphide	0.03	0.03	0.008	<0.005	0.01	0.04	0.02	0.01	<0.005	0.03	<0.005	0.03	<0.005	0.04	0.02	0.007
	99.6	99.2	99.5	99.7	100.11	99.9	100.1	100.11	99.5	99.7	99.9	99.6	99.6	99.2	100.1	100.0
Points counted for major phases	1592	1554	1516	1542	1566	1703	1570	1689	1588	1516	1491	1588	1509	1503	1613	1651
Points counted with grid ocular for analyses of chromite, Fe-Ti oxides and sulphides	58564	37268	46948	40172	43318	42955	119790	67639	53845	100793	31707	54759	48763	39326	42587	41866

Trace of phlogopite in 113380 and 135927; trace of apatite in 135945; trace of xenocrysts in 113321, 113363, 135927, 135924 and 135962; trace of zeolites in 135953 and 135972.

* Includes all chromite in the rocks.

† In several rocks residuum includes light rhyolite glass, Fe-Ti-Ca-P-rich silicate glass and traces of apatite.

‡ Reaction rims on olivine phenocrysts.

$ Includes traces of orthopyroxene phenocrysts.

¶ Microphenocrysts and groundmass difficult to distinguish, therefore all counted as groundmass.

Modal analyses have been performed in two separate countings. In both an instrumentation with simultaneously transmitted and reflected light was applied. First a grid (*c.* 1500 points) covering about 370 mm^2 was counted using a spacing of about 0.5 mm. For olivine phenocrysts with typical radius around 0.3 mm and modal abundances of about 9 vol% a standard deviation (1 σ) was estimated from the work of Solomon (1963) to be 1.0%.

In the second step chromite, sulphide and Fe-Ti oxides, which occur as tiny dispersed grains were determined. Grid ocular countings with a typical spacing of 0.016 mm and with total grid points ranging from 35000 to 120000 were used. For sulphides with a mean radius below 0.005 mm 1 σ values of about 0.004 vol% were obtained, while chromites with mean radii estimated at around 0.015 mm (conservative high estimate) gave 1 σ values between 0.01 and 0.02 vol%.

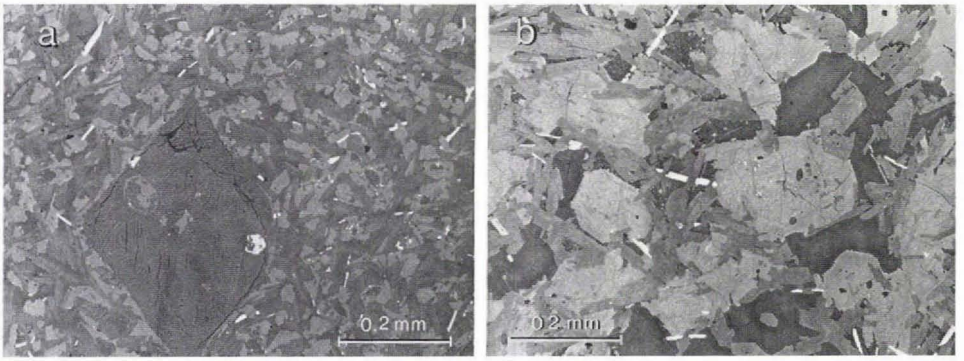

Fig. 12. a: Olivine microporphyritic basalt lava. Euhedral phenocrystic olivine pseudomorph with altered glass inclusion and chromite enclosed in a very fine-grained basaltic groundmass which shows intergranular to subophitic texture. Sample GGU 135955. Mode in Table 1. Reflected light. b: Olivine microporphyritic basalt lava. In this fairly coarse-textured rock subhedral to subophitic clino- and orthopyroxene (often mantled by clinopyroxene) and plagioclase are surrounded by intersertal patches of altered residuum with ilmenite and scarce sanidine. Numerous vugs are filled entirely with smectite. Tiny chromite crystals are enclosed in the orthopyroxene shown in the centre. Sample GGU 135956. Mode in Table 1. Reflected light.

Some lava samples show unusual ophimottled groundmass textures (fig. 14a and b) in which orthopyroxene crystals include abundant tiny plagioclase laths; porphyroblast growth has occasionally continued around early clear orthopyroxene phenocrysts (fig. 14b) or around olivine pseudomorphs. Calcic, subcalcic and pigeonitic clinopyroxene occurs as minor poikilitic grains in the groundmass and as prisms bording small vugs.

Plagioclase crystals are generally unremarkable and show normal zonation. They show only a very limited range in modal abundance from 41 to 45 vol.%.

The Fe-Ti oxides vary from as little as 0.4 vol.% in the feeder dyke to between 0.8 and 1.3 vol.% in the lavas (oxides found in iron-rich immiscible blebs excluded). Titanomagnetite seems to be the dominant Fe-Ti oxide in the feeder dyke (fig. 13) whereas ilmenite is most common in the lavas where late stage ferrioxides also occur. Groundmass oxides in the lavas show evidence of deuteric oxidation. Ilmenite in the rocks with partly metamorphic texture tends to show porphyroblastic growth (fig. 14a, b).

Residuum reaches 15 vol.% in the feeder dyke, varying from 6 to 11 vol.% in the lavas. In the least oxidized rocks, such as the dyke, the residuum consists of two coexisting melt-phases as well as scattered tiny crystals of pyroxene, plagioclase, apatite, and Fe-Ti oxides (fig. 13b to d).

The liquids were (a) light coloured rhyolite which is mostly glassy and (b) globular dark low-silica 'melt'. The dark blebs, which contain several phases among

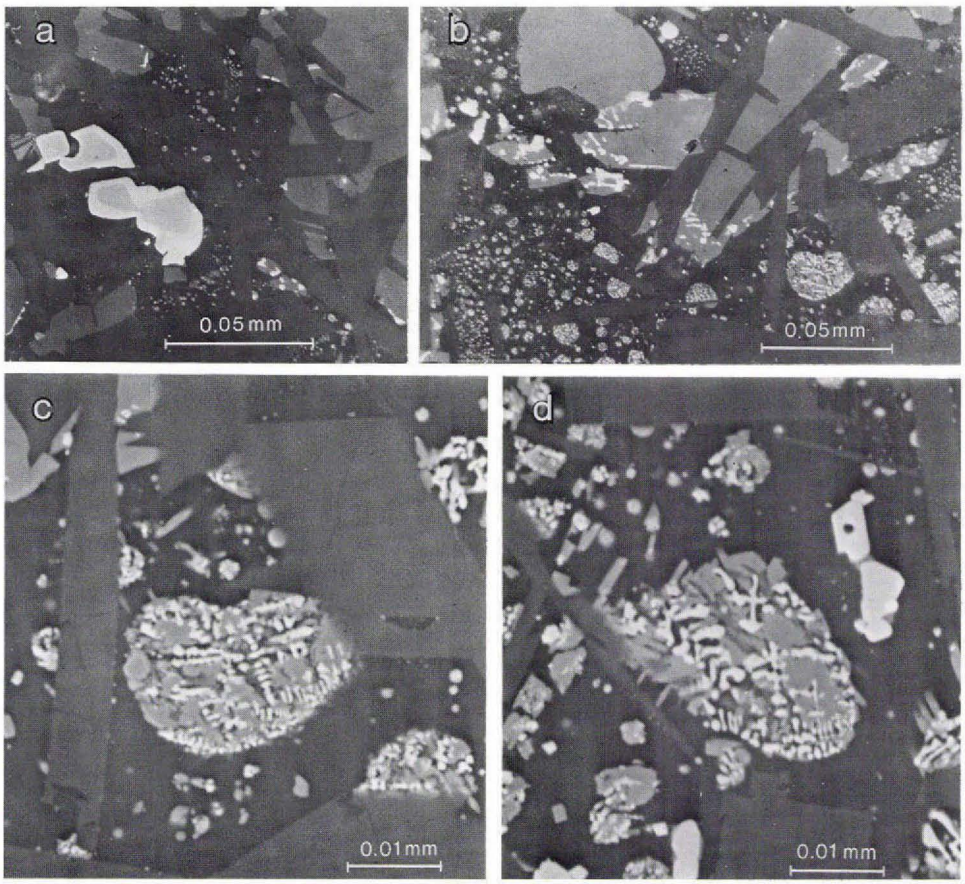

Fig. 13a to d. Groundmass in olivine microporphyritic basaltic feeder dyke sample GGU 138229. a: chromite crystal mantled by chromian titanomagnetite and surrounded by residuum and plagioclase, reflected light. b: residuum patch with strongly zoned groundmass pyroxenes which enclose titanomagnetite close to their margins. The residuum contains globular bodies of immiscible mafic 'melt' set in rhyolitic glass, reflected light. c: electron image of the largest mafic body in b which consists of calcic clinopyroxene, titanomagnetite and traces of phosphate, sulphide and residuum. d: electron image of a large mafic bleb which shows cross skeletal titanomagnetite. The light crystals outside the mafic body are ulvöspinel-rich titanomagnetite (Table 11, no. 1).

which tiny grains of skeletal titanomagnetite, calcic clinopyroxene and a phosphate can be distinguished. Tiny crystals of groundmass pyroxene are sometimes surrounded by a light rim of rhyolite glass and seem to have grown at the expense of several of the dark blebs. Traces of a residuum of dark globules in pale glass are also found in the lavas, but these features have usually been obliterated through crystallization, deuteric oxidation and later weathering.

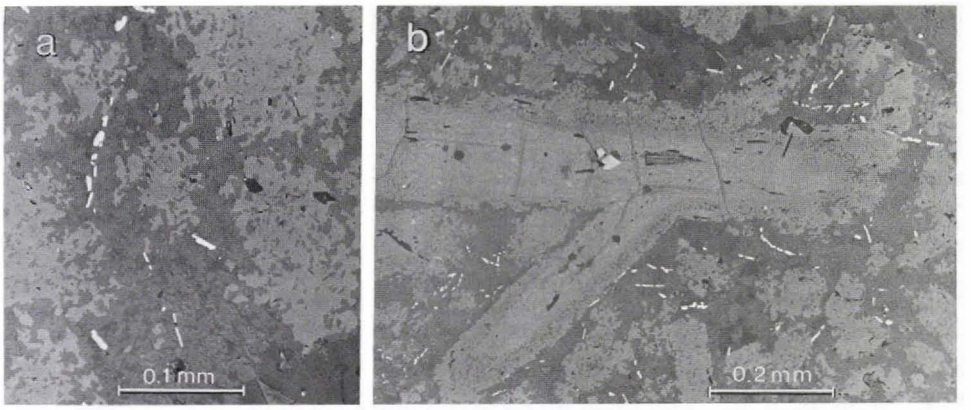

Fig. 14. Olivine microporphyritic basalt lava with ophimottled texture which is a characteristic feature of this rock. a: groundmass characterized by poikilitic orthopyroxene which encloses abundant tiny plagioclase crystals, and by minor irregular clinopyroxenes, surrounded by plagioclase and residuum-rich areas. Ilmenite forms sieve-textured plates. b: early phenocrystic orthopyroxene enclosing euhedral chromite crystals and surrounded by a spongy poikilitic mantle of orthopyroxene. Note the euhedral microphenocryst-like outline of some of the spongy orthopyroxenes in the groundmass. Sample GGU 135953. Reflected light.

Sulphides occur in very small amounts from less than 0.005 to 0.04 vol.%. Parts of these are enclosed as tiny globules in phenocryst phases, but most are interstitial pyrrhotite and pyrite precipitated from solutions.

Despite careful search, neither native iron nor graphite have been found.

Basaltic tuffs

Four petrographical types can be distinguished among the basaltic tuffs, which are all olivine microporphyritic basalts. In order of increasing degree of welding these are: (1) unwelded tuff, (2) moderately welded fiamme tuff, (3) strongly welded basaltic glass tuff, (4) recrystallized basaltic hornfels tuff.

(1) The unwelded tuff from the southern part of the tuff shield is a crumbling and altered coarse tuff. Fresh, often skeletal, olivine phenocrysts (< 1 mm) contain scattered fresh, brown euhedral chromite crystals (Table 6, no. 1) which also occur in the groundmass. The tuff clasts are highly altered and only patches of hydrated glass remain, most of the glass now consisting of green sheet silicates. The tuff consists of zeolites (mostly phillipsite, Table 12, no. 3), carbonate and green sheet silicates, which also fill the abundant vesicles. The tuff morphology is partly obscured by the alteration, but both achneliths and sharp-edged clasts can be identified. The tuff, which is probably partly phreatic in origin, differs from the typical tuffs of the shield.

Fig. 15. a: Strongly welded basaltic tuff with glassy matrix. The outline of deformed tephra clasts can still be seen. Sample GGU 113321, transmitted light. b: small immiscible sulphide droplet, composed of pyrrhotite with tiny flames of a Cu or Ni bearing sulphide phase. The droplet, which is enclosed in a glassy tuff matrix, has a slightly corroded outline. Sample GGU 113321, reflected light.

Unwelded tuff at the base of the tuff shield is composed of oxidized often shattered achneliths. This shows that the crater shield was not formed as the result of high-level phreatic activity, and indicates an initial Hawaiian to Vulcanian eruption phase (Heiken, 1974).

(2) Moderately welded fiamme tuff constitutes the upper part of the tephra units in the tuff shield (fig. 9). Where the tuff is least altered, abundant well preserved achneliths are recognizable. The often very smooth surface of the achneliths and the surrounding very fine-grained tuff matrix are highly oxidized. Olivine is altered to sheet silicate, chromite is strongly oxidized, and fine-grained ferrioxide is found throughout the nearly cryptocrystalline groundmass in the clasts.

With increasing welding the proportion of fiammes increases and their cores become more glassy and less oxidized.

(3) Strongly welded basaltic glass tuff constitutes the columnarly-jointed base of the tuff shield. The welding has here produced a glass rock in which the fiammes have become nearly coherent (fig. 15a) and flattened basaltic tephra fragments can still be discerned. Very high magnification reveals that the 'glass' is microcrystalline (particle size < 0.001 mm). Olivine, (*c.* 9 vol.%) is partly altered and contains sporadic fresh chromite grains, which also occur in the glassy matrix. A few tiny pyroxene and plagioclase microliths occur, and immiscible pyrrhotite blebs with very minor ? Ni and Cu-rich phases (fig. 15b) constitute roughly half of the sulphides in the rocks, while late pyrite is found in veins and vesicles.

(4) Recrystallized basaltic hornfels tuffs occur in the central part of the tuff shield where the tephra rocks have passed through a process of complete welding to be-

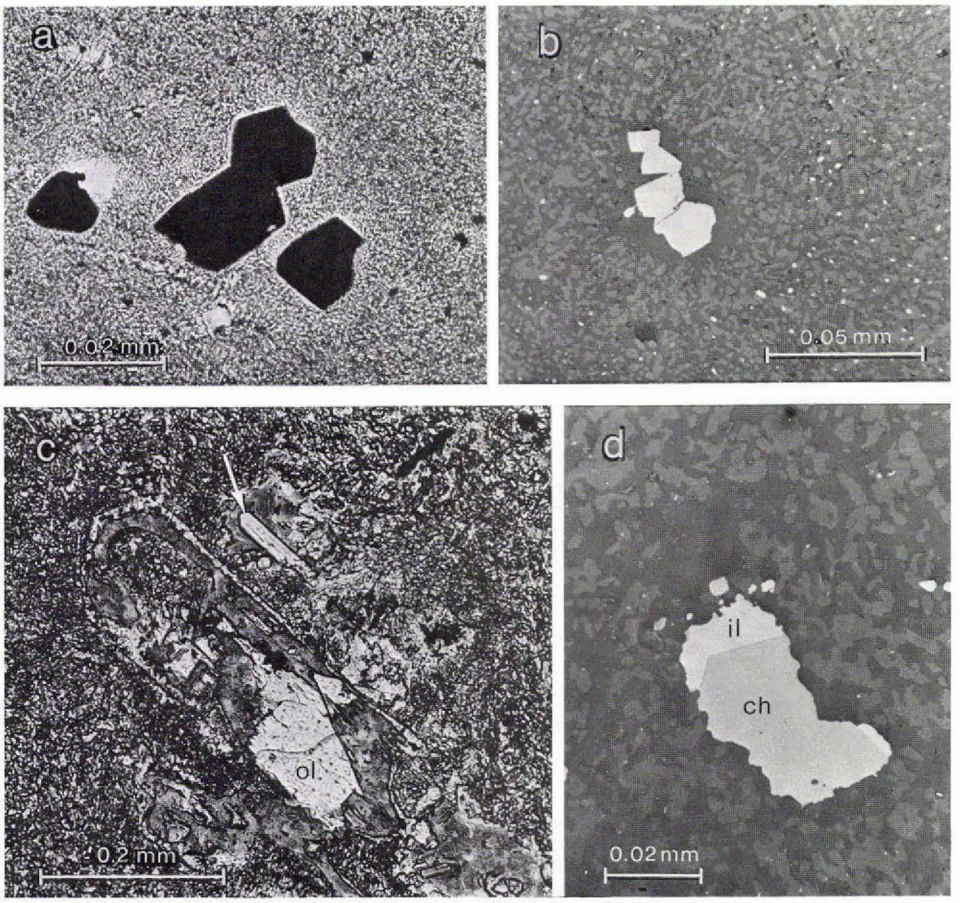

Fig. 16. a: Chromite crystals surrounded by extremely fine-grained basaltic hornfels matrix. Note that high-temperature metamorphic equilibration has depleted the hornfels in mafic components in a narrow zone surrounding the chromite. From the base of the lower tuff shield at the locality shown in fig. 10. Sample GGU 135975, transmitted light. b: another view of the same sample showing low-reflecting material surrounding the chromites, and a non-igneous rock texture. c: Basaltic hornfels with olivine phenocryst (ol) which is partly altered to smectite. The olivine carries a thin mantle of lamellar twinned pigeonite. A euhedral Ca-poor orthopyroxene crystal (arrow) has grown into one of the smectite-filled vugs. Sample no. GGU 113380. d: reequilibrated chromite (ch) partly overgrown by ilmenite (il) in basaltic hornfels from the upper tuff unit in the tuff shield. Sample GGU 113380.

come high-temperature metamorphosed crystalline rocks. This metamorphism not only induced crystallization of the glassy matrix, but also led to substantial compositional re-equilibration of the phenocrystic phases, olivine and chromite. In the lower tephra unit this metamorphism has transformed the groundmass into a nearly holocrystalline rock (grain size < 0.004 mm) with an entirely metamorphic texture

(fig. 16a and b). This process has advanced further in the basal layer of the upper tuff unit in the tuff shield, where patches of the welded tuff rock seem to have been remelted and have crystallized with partly igneous textures. Most of the rock, however, crystallized to an intergranular hornfels-textured basalt. The groundmass (*c.* 0.005 mm) is composed of pyroxene and plagioclase with small ilmenite porphyroblasts. Small vugs occur throughout the rock and are now filled by late green smectite, but, lining and projecting into the vugs (fig. 16c), are also found orthopyroxene, pigeonite, calcic augite, plagioclase, ilmenite, and phlogopite (Table 14).

Olivine phenocrysts are partly altered to smectite and carry reaction mantles of pigeonite and occasionally orthopyroxene. Around chromite microphenocrysts the very fine-grained groundmass is depleted in mafic components (fig. 16a, b), and the chromite has been greatly enriched in magnetite and ulvöspinel components (Table 6, no. 8), relative to chromite in the glassy welded tuff. Chromite has often become intergrown with ilmenite (fig. 16d).

Magnesian andesites

The magnesian andesites all carry phenocrystic olivine (pseudomorphosed except in one lava flow and one tuff layer), chromite, orthopyroxene and plagioclase.

The phenocrysts and microphenocrysts vary from 18 to 26 vol.%, and prismatic pyroxene microphenocrysts together with plagioclase define a distinct flow lamination in most rocks. The trachytic-textured groundmass (figs 17b, c) consists of pyroxene, plagioclase, glassy residuum, Fe-Ti oxides and traces of sulphides.

Olivine is a scarce phenocryst phase (0.5 to 2.5 vol%) and is always strongly resorbed and reaction-mantled by orthopyroxene. In the quenched tuff olivine is only slightly zoned, whereas in the lava a strong zonation is observed, thought to have been caused by partial metamorphic equilibration. Phenocrystic chromite (fig. 17a), (<0.02 vol.%) occurs mostly as inclusions in olivine and orthopyroxene; when in contact with the groundmass it is zoned to chromian titanomagnetite at the margin.

Orthopyroxene is the dominant phenocryst and microphenocryst phase, constituting between 16 and 22 vol.% of the rocks. Up to a few volume percent are early, millimetre-sized, macrophenocrysts while the remainder are less than 1 mm sized prisms, often mantled by clinopyroxene. A single large orthopyroxene crystal has been found to contain a few tiny flakes of graphite, otherwise this phase appears to be absent. Orthopyroxene in the tuff (135961) often shows skeletal outlines (fig. 18) and does not carry reaction mantles.

Plagioclase microphenocrysts (2 vol.%) mostly occur as thin plates.

In some andesites the groundmass is too fine-grained to allow microprobe analysis of individual phases.

Groundmass pyroxenes, constituting about 12 to 14 vol.% of the rocks, include augite, subcalcic augite, pigeonite and orthopyroxene.

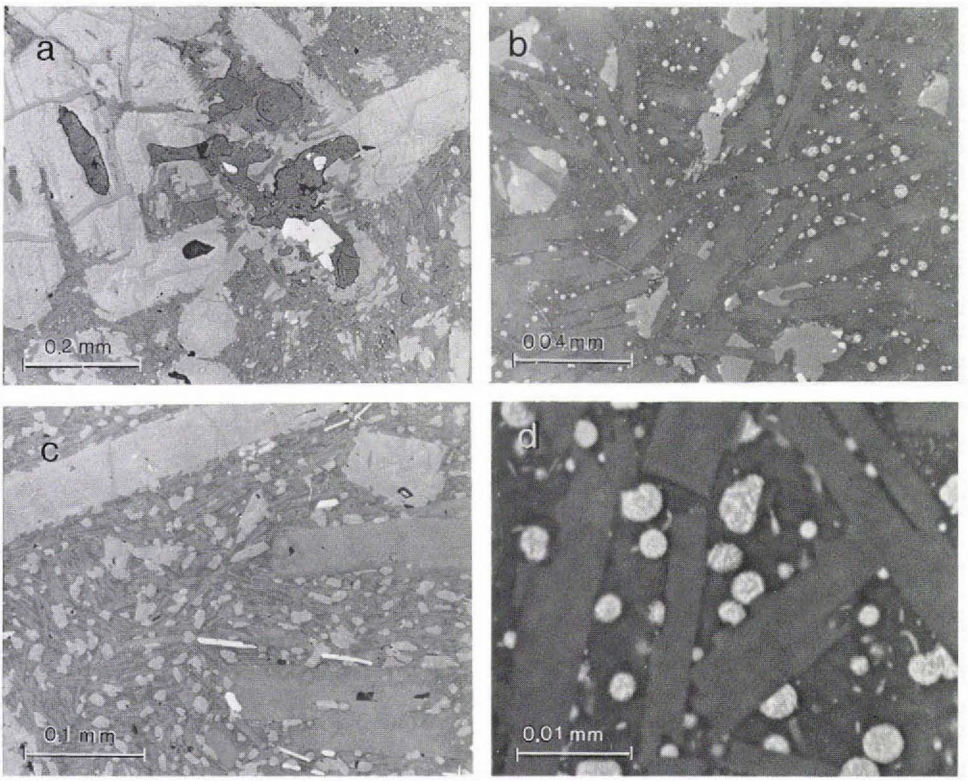

Fig. 17. Magnesian andesites. a: phenocrysts of orthopyroxene and olivine, the latter pseudomorphosed by smectite. The olivine pseudomorphs which enclose chromite show resorbed outlines and are mantled by orthopyroxene. Sample GGU 135924, reflected light. b: trachytic-textured groundmass consisting of plagioclase, pyroxene and a residuum which consists of rhyolitic glass coexisting with an exsolved Fe-Ti-Ca-P-rich mafic glass phase, which has crystallized later, sample GGU 135924, reflected light. c: trachytic-textured groundmass consisting of plagioclase, pyroxene and platy ilmenite set in a rhyolitic glassy residuum. Microphenocrystic plagioclase and orthopyroxene is also seen, sample GGU 135962, reflected light. d: electron image of the groundmass shown in b. The tiny mafic globular bodies can be seen to contain several phases with a mean atomic number much higher than plagioclase. Sample GGU 135924.

The groundmass plagioclase (33 to 41 vol.%) forms thin plates which are normally zoned. No sanidine or anorthoclase have been encountered.

The residuum which constitutes 17 to 24 vol% of the rocks, is extensively altered and quartz-rich in some samples (e.g. 135945). In those samples that are least affected by post-eruption processes (e.g. 135924 and 135927) the residuum consists of a light coloured rhyolitic glass and unmixed dark spheres (<0.003 mm) of a Fe-Ti-Ca-P silicate 'melt' which is now crystallized (fig. 17b and d). The dark spheres, which constitute about 6% of the residuum in the investigated rock, are treated separately in a later section.

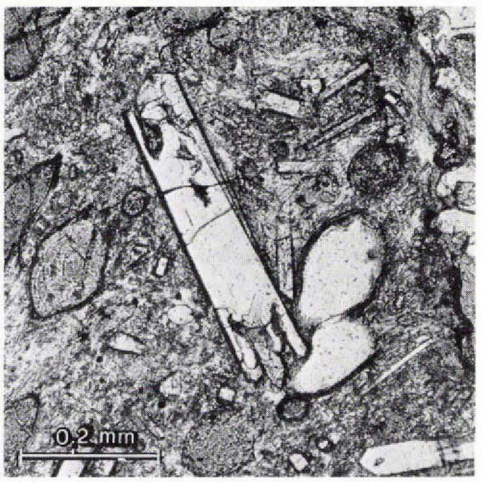

Fig. 18. Magnesian andesite tuff. A skeletal orthopyroxene microphenocryst together with other orthopyroxene crystals in a tuff matrix which has been metamorphosed to smectite and zeolites. Sample GGU 135961. Plane polarized light.

Associated with the residuum are found Fe-Ti oxides, pyroxene and traces of apatite. Fe-Ti oxides show substantial modal variation in the andesites, reaching 0.6 vol.% in samples without preserved dark spheres, whereas in samples where these spheres are preserved only 0.07 to 0.12 vol.% of well crystallized oxides are found outside the dark spheres. The oxides occur as ilmenite plates, and as titanomagnetite reaction rims on scarce chromite. Titanomagnetite is also found as isolated grains in residuum, or enclosed in late groundmass pyroxene. In the samples with dark spheres, a major part of the Fe-Ti oxides in the rock occurs as tiny skeletal grains inside the spheres, far too small to be quantitatively analysed. Up to 0.04 vol.% sulphides is found in the least oxide-rich samples whereas less than 0.005 vol.% is present in the oxidized rocks. Only very little sulphide is present as immiscible blebs in silicate phenocrysts, but the dark immiscible silicate blebs contain substantial amounts of sulphur (Table 24), which must be present as sulphides.

Feldspar-phyric silicic basalt

This rock is a glomeroporphyritic basalt with an intersertal texture which contains about 9 vol.% phenocrysts of plagioclase with minor Cr-rich augite, orthopyroxene, chromite and traces of olivine pseudomorphs. The glomerophyres are up to 1 to 2 mm in size and may include more than 20 stout plagioclase phenocrysts which tend to show oscillatory zoning (An_{79} to An_{68}). Chromite (0.01 vol.%) occurs as tiny brown octahedra enclosed in phenocrysts and in groundmass silicates. The groundmass is composed of pyroxene, plagioclase (zoned from An_{68} to An_{53}), Fe-Ti oxides and altered residuum. The groundmass pyroxenes are augite, subcalcic augite and pigeonite (fig. 26b) which display extensive zoning; pigeonite and subcalcic augite have often nucleated on each other.

Fe-Ti oxides are more abundant in the groundmass (2 vol.%) than in other Kûgánguaq Member rocks and include extensively oxidized ilmenite and titanomagnetite. Sulphides (<0.01 vol.%) are late and interstitial. About 13 vol.% of the rock is composed of altered residuum with green smectite, high silica zeolite, silica and carbonate. The numerous vesicles are filled with green sheet silicates, carbonate and silica.

Xenoliths and xenocrysts

In the olivine microporphyritic basalt lava neither xenoliths nor xenocrysts have yet been found. In the lower tuff unit in the basaltic tuff shield a number of rounded xenoliths, up to walnut-size, have been recognized, most of them in the moderately to poorly welded part of the tuff. The xenoliths which have abundant calcite-filled vesicles, are friable and extensively altered. A single xenolith from the lower glassy part of the tuff is moderately well preserved and can be recognized as a vesiculated, partially melted sandstone.

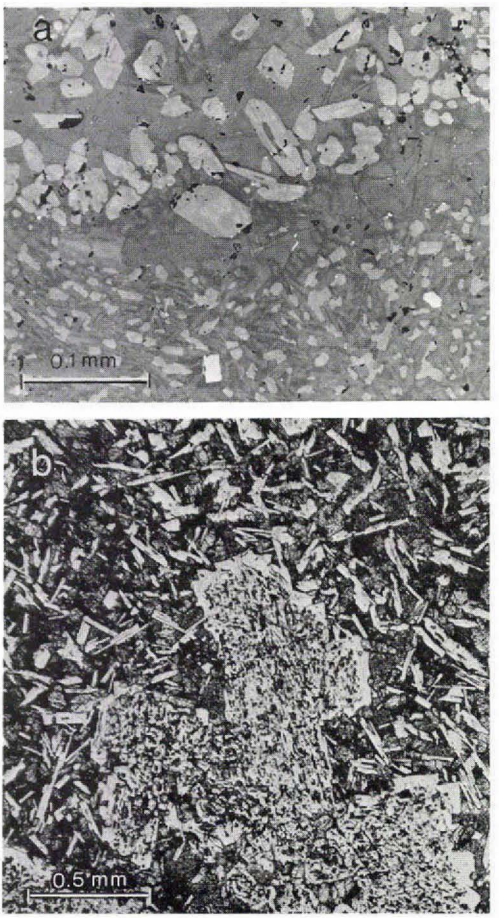

Fig. 19. a: Euhedral pyroxene crystals in glass rimming a quartz xenocryst (not shown) in a magnesian andesite. Tiny needles of an unidentified Fe-Ti oxide are seen in the glass. The trachytic-textured groundmass of the host andesite is seen outside the glass zone. Sample GGU 135962, reflected light. b: sieve-textured aggregate of plagioclase xenocrysts in feldspar-phyric silicic basalt. The groundmass shows intersertal texture. Sample GGU 135972.

In the magnesian andesites xenocrystic quartz is widespread, but never abundant. The quartz occurs as strongly resorbed grains, which tend to be surrounded by rhyolitic glass with many enclosed euhedral pyroxene crystals (fig. 19a). Xenocrystic plagioclase occurs as a 2 mm aggregate and as scattered grains in one andesite. The plagioclase is devoid of graphite or red spinel, which is characteristic of xenocrystic plagioclase from the iron metal-bearing volcanic rocks from Disko (e.g. Törnebohm, 1878). Scattered spongy and sieve-textured plagioclase xenocrysts occur in the feldspar-phyric silicic basalts (fig. 19b).

All xenoliths and xenocrysts therefore seem to be derived from sandstones, but disaggregated gneiss cannot be excluded as a source for some of them. Contrary to the evidence from the older Asuk Member lavas (e.g. Pedersen, 1979a), no traces of xenoliths or xenocrysts which could point to an origin from shales have been found.

Petrographical summary

The main petrographical features of the three rock types in the Kûgánguaq Member can be summarized as follows.

The olivine microporphyritic basalts contain early crystallized olivine (often pseudomorphosed) and chromite, and none of the rocks appear to be cumulative in these phases. A few of the samples contain scarce early orthopyroxene. The groundmasses show substantial textural variation from magmatic to metamorphic textures. In well crystallized groundmasses abundance in low-Ca pyroxene and scarcity in Fe-Ti oxides are characteristic features.

The magnesian andesites contain abundant early crystallized orthopyroxene, scarce olivine (often pseudomorphosed), chromite and plagioclase, and none of the rocks appear to be cumulative. The groundmasses contain substantial amounts of low-Ca pyroxene, and some rocks are extremely scarce in Fe-Ti oxides.

The feldspar-phyric silicic basalts contain abundant glomerophyritic plagioclase, very scarce olivine (pseudomorphosed) and scattered orthopyroxene and augite phenocrysts. Scarce early chromite is enclosed in all the other phenocryst phases. The well crystallized groundmasses contain calcic and subcalcic augite and pigeonite. The widespread Fe-Ti oxides show marked subsolidus oxidation.

Evidence for contamination in the Kûgánguaq Member rocks is found in the form of scattered sandstone xenoliths in basaltic tuffs, widespread quartz xenocrysts and sieve-textured plagioclase xenocrysts in magnesian andesites, and scattered sieve-textured plagioclase xenocrysts in feldspar-phyric silicic basalts.

Most of the rocks in the Kûgánguaq Member show evidence of low zeolite facies metamorphism and contain smectite and various low temperature zeolites.

MINERAL CHEMISTRY

This account is based on microprobe analyses made at the Grant Institute of Geology, University of Edinburgh (Microscan 5 microprobe), Research School of Earth Sciences, Canberra (T.P.D. microprobe), and Institute of Mineralogy, Copenhagen University (Jeol 733 Superprobe). Institutions and type of analysis are indicated for the individual analyses in the microprobe tables.

Of particular importance for this study are the trace and minor element analyses made at the Jeol 733 instrument in Copenhagen. Details of the analytical tech-

Table 2. Detection limits for microprobe analyses

Sample	Analysed phase	Element	No. of duplicate analyses	Acceleration potential in Kv.	Beam-current in n.A.	Lower limit of detection (2σ) based on t-test* in ppm	Lower limit of detection for 1 analysis based on theoretical counting statistics in ppm†
138228	Glass	Ni	6	20	100	21	64
138228	Olivine	Ni	7	20	100	15	60
138228	Glass	Cr	6	20	100	9	32
St. Johns olivine	Olivine	Cr	6	20	100	12	30
136943	Olivine	P	9	20	100	12	50
Synthetic forsterite	Olivine	V	4	20	500	17	24
176671	Olivine	V	12	20	500	5	26
Synthetic forsterite	Olivine	Ti	4	20	500	5	23
176671	Olivine	Ti	12	20	500	4	14

Lower limits of detection in olivine and glass based on 90 seconds of grid counting on each of top and backgrounds.

* Lower limits of detection (l.l.d.) based on t-test at 95% confidence level. Formula: l.l.d. (in ppm) = $\frac{\sqrt{2}}{m \cdot a} \cdot t_f^{0.95} \cdot \frac{\sigma}{\sqrt{n}}$; m = cps/1 ppm, a: counting time in sec. per analysis; σ: pooled standard deviation based on $\sigma^2 = \frac{\sigma^2 \text{ peak} + \sigma^2 \text{ background}}{2}$; n: number of duplicate analyse; t: t-distribution factor at 95% confidence level and at f degrees of freedom; $f = 2n - 2$.

† Lower limit of detection at the 2σ (c. 95% confidence) for one analysis based on theoretical statistics.

Formula: l.l.d. = $4/m \cdot \sqrt{C_b/T}$; C_b: count rate in cps on the background; T: time of analysis on peak in seconds.

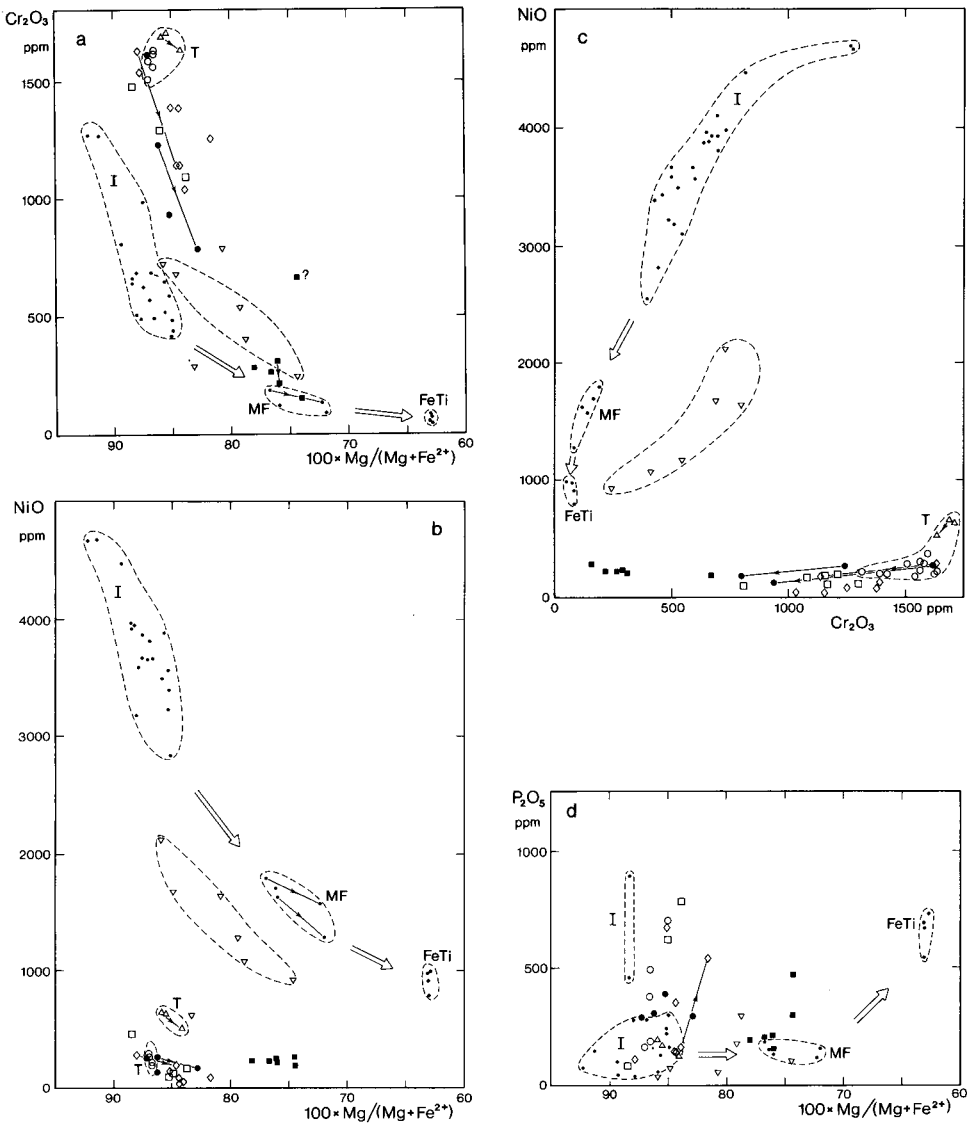

niques will be published in a separate paper. Briefly, trace element analyses were made with an automated grid-counting procedure counting for 90 sec. on both peak and backgrounds. With total electron fluxes increased by factors of 30 (Cr, Ni, P) and 150 (Ti and V) as compared to routine spectrometer analyses, detection limits were greatly improved. Detection limits as currently estimated at the microprobe laboratory are obtained by comparison of peak and background populations for series of duplicate analyses with a students t-test at the 2 σ level. Table 2 gives detection limits and applied formulae, together with detection limits for individual

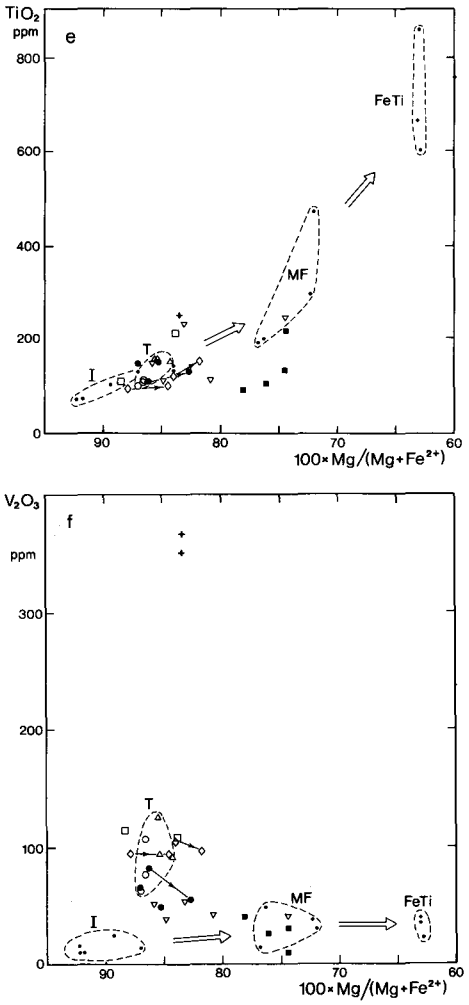

←

Fig. 20. Composition of olivines from the Kûgánguaq Member and related rocks. For comparison are shown olivines from the Vaigat Formation picrite glasses (field I, representing samples GGU 136943, 264104 and 264137), from a basaltic pillow from the Maligât Formation (field MF, sample GGU 176765) and from a Fe-Ti basalt glass from a late dyke (field FeTi, sample GGU 176554). Lines with arrows connect core and margin of olivine crystals, while the broad double arrows show the trend indicated for olivines in uncontaminated quenched basaltic rocks from Disko. Field T represents olivines in quenched basaltic and andesitic tuff from the Kûgánguaq Member. a: Cr_2O_3 *v.* 100 × Mg/(Mg+Fe^{2+}) (atomic ratio). b: NiO *v.* 100 × Mg/(Mg+Fe^{2+}). c: NiO *v.* Cr_2O_3. d: P_2O_5 *v.* 100 × Mg/(Mg+Fe^{2+}). e: TiO_2 *v.* 100 × Mg/(Mg+Fe^{2+}); cross: olivine cores in the iron metal-bearing basalt glass (sample GGU 176671) from the Kitdlît dyke at Luciefjeld, south Disko (Pedersen, 1979b). f: V_2O_3 *v.* 100 × Mg/(Mg+Fe^{2+}); cross as in e. Note the high V_2O_3 in olivine in the iron metal-bearing glass rocks (sample GGU 176671), and the distinctly enriched V_2O_3-level in quenched Kûgánguaq Member samples (field T) as compared to the uncontaminated rocks (fields I, MF and FeTi). Total vanadium is reported as V_2O_3, but the states of valency have not been determined.

• Olivine from picrites (I), glass rock from Maligât Formation (MF) and Fe-Ti rich basalt glass (FeTi)

KÛGÁNGUAQ MEMBER AND RELATED ROCKS

Basalts: Feeder dyke ◇ 138229
Pillow glass □ 264110
Tuffs, increasingly metamorphosed
○ 113374
● 113321
■ 113380

Andesites: Lava ▽ 135962
Tuff △ 135961

analyses based on theoretical counting statistics. In general duplicate analyses indicate that contributions to the analytical signals from external noise, instrumental drift etc. are negligible. Most determinations were made as averages of between 2 and 4 analyses, but because of the reconnaissance nature of this work some single determinations have also been used, when the values obtained exceeded the detection limits based on 4 to 6 analyses on a similar phase.

In the following section, microprobe-based descriptions are given of the phases olivine, chromite, pyroxenes, Fe-Ti oxides, feldspar, smectite, zeolite, carbonate and late stage residuum, such as rhyolite and exsolved Fe-Ti-Ca-P-rich silicate. Probe work on basalt glass and very fine-grained groundmass is reported together with the bulk rock chemical analyses. In order to provide comparative material,

Table 3. Olivine from the Kûgánguaq Member rocks

Analysis	1	2†	3	4	5	6	7	8	9
GGU no.	138229	264110	113374	113321	113321	113380	135961	135962	135962
SiO_2	40.0	40.4	39.7	40.3	40.0	39.00	39.8	39.8	38.5
TiO_2	0.02	0	<0.02	0.02	0.02	0.02	0	<0.02	0.02
Al_2O_3	0.02	0	0.05	0.05	0.03	0.09	0.05	0.09	0.03
Cr_2O_3	0.130‡	0.137‡	0.165‡	0.133‡	0.075‡	0.025‡	0.126‡	0.120‡	0.078‡
FeO*	11.7	11.2	12.8	12.4	14.1	20.2	13.5	12.6	20.5
MnO	0.17	0.2	0.17	0.15	0.17	0.24	0.18	0.17	0.26
NiO	0.028‡	0.031‡	0.028‡	0.028‡	0.013‡	0.022‡	0.059‡	0.244‡	0.131‡
MgO	47.5	47.7	46.6	47.2	45.9	40.3	45.9	46.9	40.3
CaO	0.17	0.2	0.18	0.20	0.19	0.18	0.22	0.22	0.16
	99.74	99.87	99.69	100.48	100.50	100.08	99.84	100.14	99.98
mg	87.9	88.4	86.6	87.2	85.3	78.0	85.8	86.9	77.8
Cations based on 4 oxygens									
Si	0.9929	0.9986	0.9912	0.9953	0.9955	1.0027	0.9952	0.9894	0.9943
Ti	0.0004		0.0000	0.0004	0.0004	0.0004	0.0000	0.0000	0.0004
Al	0.0006		0.0015	0.0015	0.0009	0.0027	0.0015	0.0026	0.0009
Cr	0.0026	0.0027	0.0033	0.0026	0.0015	0.0005	0.0025	0.0024	0.0016
Fe^{2+}	0.2429	0.2315	0.2673	0.2561	0.2935	0.4343	0.2823	0.2620	0.4428
Mn	0.0036	0.0042	0.0036	0.0031	0.0036	0.0052	0.0038	0.0036	0.0057
Ni	0.0006	0.0006	0.0008	0.0006	0.0003	0.0005	0.0012	0.0049	0.0027
Mg	1.7572	1.7572	1.7340	1.7374	1.7024	1.5441	1.7105	1.7375	1.5512
Ca	0.0045	0.0053	0.0048	0.0053	0.0051	0.0050	0.0059	0.0059	0.0044
	3.0053	3.0001	3.0065	3.0023	3.0032	2.9954	3.0029	3.0083	3.0040

*Total iron as FeO.
$mg = 100 \times Mg/(Mg + Fe^{2+})$.
† = by energy dispersive analysis (e.d.a.) except for Cr and Ni; all other analyses by w.d.a.
‡ = separate trace element analyses by wavelength dispersive analysis (w.d.a.).
Analyses 1 to 4 and 6 to 9 made at Institute of Mineralogy, Copenhagen.
Analysis 5 made at Grant Institute of Geology, Edinburgh.
1. Core of phenocryst in olivine microporphyritic basaltic feeder dyke.
2. Core of olivine phenocryst in glassy margin of basaltic pillow.
3. Core of large skeletal olivine phenocryst in basaltic tuff.
4. Core of olivine phenocryst in glassy base of lower tuff unit in the tuff shield.
5. Margin of same phenocryst as analysis 4.
6. Core of olivine phenocryst rimmed by clinopyroxene in basaltic hornfels tuff.
7. Core of olivine phenocryst rimmed by orthopyroxene in andesitic air fall tuff.
8. Core of olivine phenocryst rimmed by orthopyroxene in andesitic lava.
9. Olivine margin of same phenocryst as analysis 8.

some work is also reported on selected uncontaminated picritic glass samples and olivine-poor tholeiitic basalts from outside the Kûgánguaq Member.

Particularly detailed work has been done on olivine, pyroxenes, chromite and glasses because of their importance in a redox context.

Olivine

Olivine, originally present as a phenocryst phase in all Kûgánguaq Member rocks, is only preserved in a few of the investigated rocks: in the basaltic feeder dyke, in one basalt lava, in parts of the strongly welded layers in the basaltic tuff shield, in one unwelded basalt tuff, in one andesite lava and in an andesite tuff.

The Kûgánguaq Member olivine shows a total compositional variation from *mg* = 88 to 74 (Table 3 and figs 20 and 22a to c), but only the limited range of *mg* = 88 to 83 reflects primary magmatic crystallization, the more iron-rich compositions being due to high-temperature autometamorphic equilibration.

The olivine is unremarkable with respect to Mn and Ca. The olivine compositions (Tables 3 and 4) reflect the lower Ca-content of Kûgánguaq Member magmas compared with picritic glasses.

Cr shows some unusual, petrogenetically significant features (fig. 20a). Cr in olivine from uncontaminated picritic and tholeiitic glass samples decreases with *mg*. The quenched Kûgánguaq Member olivine, represented by one basaltic (113374) and one andesitic (135961) tuff, is two to three times higher in Cr than picritic olivines with similar *mg* values. Further, comparison between quenched and autometamorphosed olivine in both basaltic and andesitic rocks shows that subsolidus, or near-solidus, equilibration has led to both decreasing *mg* and strongly decreasing Cr (fig. 20a and Table 3, nos 3 and 6).

Considerable Cr-zoning has been found in olivine crystals from the glassy welded tuff (113321) and the feeder dyke.

Ni shows unusual features (fig. 20b) in the Kûgánguaq Member rocks. The Ni-contents of olivine from uncontaminated picritic to tholeiitic rocks are much higher than those from Kûgánguaq Member olivine at comparable *mg* levels (fig. 20b, Table 4). Within each rock group Ni decreases with *mg* in the olivine. Ni in olivine is distinctly lower in the basalts than in the andesites (Table 3, nos 1 and 8), which leads to anomalously low Ni/Cr ratios in olivine from the Kûgánguaq Member rocks (fig. 20d), particularly in those from quenched basalts. Similar features in the iron-bearing basaltic glass rock at Luciefjeld, south Disko (Pedersen, 1979b) are ascribed to the effects of sulphide and metal fractionation.

Variation of P_2O_5 in magmatic olivine is generally poorly known, but in certain pallasites up to 4.9 wt.% P_2O_5 has been reported to enter olivine without disturbing its stoichiometry (Buseck, 1977). Recently, similar olivine has been reported from Uivfaq, south Disko by Goodrich (1983, 1984). In the uncontaminated picritic to moderately evolved tholeiitic rocks most olivine contains below 250 ppm P_2O_5 (fig. 20e), the lowest values occurring in the olivine cores ($\ll$ 100 ppm). However, one picrite sample shows anomalously high P_2O_5 values (up to 900 ppm) in some olivine cores. The Kûgánguaq Member andesitic olivines are P_2O_5-poor, whereas those in Kûgánguaq Member basalt and other related basalts show considerable variation. Large cores generally show low values whereas outer zones, and small microphe-

Table 4. Olivine from the Vaigat Formation picrite glasses

Analysis	1	2	3	4	5	6
GGU No.	136943	136943	136943	136943	264104	264104
SiO_2	40.9	40.5	40.3	39.8	40.5	40.3
TiO_2	0.04	0.06	0.05	<0.02	<0.02	<0.02
Al_2O_3	0.07	0.09	0.05	0.04	0.05	0.05
Cr_2O_3	0.097‡	0.078‡	0.041‡	0.060‡	0.046‡	0.052‡
FeO*	7.58	10.2	12.5	13.5	10.8	13.4
MnO	0.09	0.18	0.15	0.16	0.19	0.14
NiO	0.42‡	0.42‡	0.32‡	0.24‡	0.38‡	0.35‡
MgO	50.7	48.5	47.1	45.9	48.3	45.7
CaO	0.28	0.28	0.34	0.38	0.28	0.32
	100.18	100.31	100.85	100.08	100.55	100.18
mg	92.3	89.4	87.0	85.8	88.8	85.9
Cations based on 4 oxygens						
Si	0.9932	0.9942	0.9938	0.9939	0.9943	1.0025
Ti	0.0007	0.0011	0.0009			
Al	0.0020	0.0026	0.0015	0.0012	0.0015	0.0015
Cr	0.0019	0.0015	0.0008	0.0012	0.0009	0.0011
Fe^{2+}	0.1540	0.2094	0.2578	0.2820	0.2218	0.2788
Mn	0.0019	0.0037	0.0031	0.0034	0.0040	0.0030
Ni	0.0082	0.0083	0.0064	0.0048	0.0075	0.0068
Mg	1.8350	1.7744	1.7310	1.7083	1.7673	1.6942
Ca	0.0073	0.0074	0.0090	0.0102	0.0074	0.0085
	3.0042	3.0026	3.0043	3.0050	3.0047	2.9964

* total iron as FeO.
‡ = separate trace element analyses by w.d.a.
All analyses at Institute of Mineralogy, Copenhagen.

mg = 100 × Mg/(Mg + Fe^{2+}).
Analyses 1 to 5 by w.d.a., no. 6 by e.d.a.

1. Core of large phenocryst.
2. Core zone of olivine with inclusion filled healed fractures.
3. Euhedral olivine phenocryst.
4. Euhedral small olivine microphenocryst.
5. Clear outer zone of olivine with strong inclusion rich core.
6. Margin of olivine phenocryst.

nocrysts, have P_2O_5 levels which may exceed 900 ppm (fig. 20e). High values are often found in skeletal crystals, which may suggest at least a partial kinetic control of P_2O_5 concentrations.

In order to find other possibly redox-controlled anomalies a limited number of olivine crystals were analysed for Ti and V. Ti (as TiO_2) varies from less than 100 ppm in the most magnesian olivine in picrite glass up to 800 ppm in Fe-Ti basalt glass (176554) (fig. 20e). The Kûgánguaq Member olivine is not notably anomalous compared to the other basaltic glass rocks, except that olivine from the basaltic hornfels tuff (113380) is low in TiO_2 at comparable *mg* values. The reanalysed olivine from the iron-bearing glass rocks at Luciefjeld (Pedersen, 1979b, Table 2) is slightly higher in TiO_2 (250 ppm) than other olivine with *mg*: 80–85.

On the other hand V (as V_2O_3) in the olivine appears to be strongly f_{O_2}-sensitive as the uncontaminated picritic to tholeiitic olivine has low concentrations (< 50 ppm), whereas the quenched Kûgánguaq Member basaltic and andesitic olivine is V-enriched (100–130 ppm) (fig. 20f). Olivine in the basaltic hornfels tuff and the andesite showing autometamorphic textures (135962) has low V levels, characteristic of the uncontaminated rocks. That from the iron-bearing Luciefjeld basalt glass (Pedersen, 1979b) is several times higher in V_2O_3 (about 350 ppm) than any other olivine reported here, indicating that the stability of V in olivine increases markedly as the stability field of metallic iron is approached.

Chromite

Chromite is present in small amounts in all Kûgánguaq Member rocks and has been analysed in detail. Tables 5 to 8 give the chemical compositions of selected chromite grains, and their substitution patterns are illustrated by figs 21 to 25.

The quenched chromite from Kûgánguaq Member and related glasses (fig. 21 c–d, Tables 6–7) shows limited chemical variation and closely approximates (Mg, Fe^{2+})(Cr, Al)$_2O_4$ compositions. The most magnesian chromite (*mg* = 65) is enclosed in early olivine while the most iron-rich grains (*mg* = 52 to 56) are found as euhedral crystals in glass. Chromite from other rocks shows slightly different Cr/Cr + Al ratios and is rather poor in Ti and Mn. Calculations based on 24 cations and 32 oxygens indicate very low Fe_2O_3 contents in quenched chromite, generally between 1 and 2 wt.% (figs 22 and 23). V, as V_2O_3, is invariably high in chromite from the basalts and lower and more variable in that from the andesites.

Quenched chromite from the uncontaminated picritic glasses (fig. 21a, Table 5) is not very different from that in the Kûgánguaq Member rocks in terms of (Mg, Fe) (Cr,Al)$_2$ components, but varies more within individual samples where there is a rough correlation between the composition of chromite and host olivine or glass. The most magnesian chromite (*mg* = 76) (Table 5, no. 1) is enclosed in very magnesian olivine (*mg* = 92.5–91) and has high Cr/Cr + Al ratios (0.70–0.62) whereas chromite from the glass has *mg* = 0.60 and Cr/Cr + Al = 0.60 to 0.52. More aluminous chromian spinel, which characterizes MOR picrite glass and spinel lherzolite (e.g. Sigurdsson & Schilling, 1976) seems to be missing or rare. The chromite is generally poor in Ti and Mn and differs distinctly from the Kûgánguaq Member chromite by being poor in V (except for one single anomalous grain in an olivine xenocryst, fig. 23a) and by its much higher calculated Fe_2O_3 (figs 22 and 23). Chromite grains from the picrite glasses show a crude correlation of Fe^{3+} to Fe^{2+} = 2 (fig. 22) which indicates a predominant magnetite component. In addition, some chromites in anomalous olivine grains with inclusion-filled cores (often with abundant healed cracks and with clear unfractured margins) show anomalous Fe_2O_3 enrichment and may compositionally approach magnesioferrites.

In summary, quenched chromites from the Kûgánguaq Member and from picrite

Table 5. Chromites and related oxides in picritic glasses from the Vaigat Formation

Analysis	1	2	3	4	5	6	7	8	9
GGU no.	136943	136943	136943	136943	136943	136943	264104	264104	264104
SiO_2	0.16	0.18	0.11	0.17	0.11	0.15	0.09	0.12	0.11
TiO_2	0.50	0.59	0.74	0.97	1.01	0.93	0.98	1.03	1.09
Al_2O_3	18.5	17.9	14.9	25.0	17.4	7.90	19.8	20.3	20.2
Cr_2O_3	46.6	47.7	45.0	33.6	35.3	22.0	40.8	38.9	34.0
V_2O_3	0.12	0.15	0.09	0.15	0.12	0.07	0.14	0.20	0.16
FeO*	15.2	15.8	22.5	23.8	30.7	54.2	21.9	25.6	29.3
MnO	0.19	0.16	0.18	0.14	0.24	0.20	0.24	0.19	0.15
NiO	0.23‡	0.18	0.26‡	0.22‡	0.15‡	0.24	0.24‡	0.20‡	0.11
MgO	16.6	16.3	14.5	14.3	12.9	10.2	14.6	13.2	13.0
CaO	0.02‡	0.02	0.11	n.a.	0.02‡	0.05	0.09	0.03‡	0.13
	98.12	98.98	98.39	98.35	97.95	95.94	98.88	99.77	98.25
Fe_2O_3	6.53	6.28	11.49	10.31	17.05	40.63	9.80	10.83	15.03
FeO	9.32	10.14	12.16	14.53	15.36	17.64	13.09	15.86	15.78
	98.77	99.60	99.54	99.39	99.66	100.01	99.87	100.86	99.76
mg	76.0	74.5	68.0	63.7	60.0	50.8	66.5	59.7	59.5
Cations based on 24 cations and 32 oxygens									
Si	0.0396	0.0444	0.0279	0.0414	0.0279	0.0407	0.0222	0.0296	0.0275
Ti	0.0929	0.1094	0.1409	0.1776	0.1926	0.1896	0.1822	0.1913	0.2050
Al	5.3907	5.2018	4.4478	7.1764	5.2025	2.5241	5.7694	5.9107	5.9545
Cr	9.1056	9.2952	9.0077	6.4677	7.0775	4.7135	7.9719	7.5951	6.7208
V	0.0237	0.0297	0.0182	0.0293	0.0244	0.0152	0.0278	0.0396	0.0321
Fe^{3+}	1.2150	1.1658	2.1888	1.8886	3.2545	8.2869	1.8221	2.0127	2.8277
Fe^{2+}	1.9270	2.0914	2.5758	2.9579	3.2571	3.9977	2.7048	3.2750	3.2994
Mn	0.0398	0.0334	0.0386	0.0289	0.0516	0.0459	0.0503	0.0398	0.0318
Ni	0.0457	0.0357	0.0530	0.0431	0.0306	0.0523	0.0477	0.0397	0.0221
Mg	6.1147	5.9880	5.4716	5.1892	4.8758	4.1197	5.3779	4.8586	4.8443
Ca	0.0053	0.0053	0.0298		0.0054	0.0145	0.0238	0.0079	0.0348

$mg = 100 \times Mg/(Mg + Fe^{2+})$.
*Total iron as FeO.
W.d. analyses as Institute of Mineralogy, Copenhagen.
‡ = separate trace element w.d. analyses.

1. Chromite in glass inclusion in olivine (*mg* = 91.9) in picritic pillow glass.
2. Chromite enclosed in magnesian olivine grain (*mg* = 91.3).
3. Chromite in glass inclusion enclosed in olivine grain (*mg* = 89.5).
4. Chromite phenocryst in glass.
5. Margin of chromite phenocryst grown at the rim of oxidized olivine grain.
6. Chromian magnesio-ferrite enclosed in the core of oxidized olivine grain (*mg* = 88.1).
7. Chromite in the clear olivine zone (*mg*= 88.8) surrounding strongly inclusion-filled olivine core in picritic pillow glass.
8. Chromite in olivine phenocryst (*mg* = 87.3) in picritic pillow glass.
9. Chromite phenocryst in glass.

Table 6. Chromites in basaltic tuffs from the Kûgánguaq Member

Analysis	1	2	3	4	5	6	7	8
GGU no.	113374	138348	113321	113321	135975	135975	113380	113380
SiO_2	0.14	0.06	0.07	0.13	0.13	0.11	0.08	0.56
TiO_2	0.70	1.16	1.10	0.90	0.64	1.27	6.15	8.16
Al_2O_3	20.6	21.1	22.9	19.5	20.2	15.9	8.99	4.74
Cr_2O_3	48.0	44.5	41.7	45.9	40.6	39.4	34.6	23.8
V_2O_3	0.84	1.48	1.31	0.78	0.71	0.75	0.84	1.40
FeO*	15.9	18.2	20.5	22.9	27.8	32.7	42.0	53.7
MnO	0.18	0.21	0.20	0.29	0.24	0.24	0.26	0.22
NiO	n.a.	<0.02	0.007‡	<0.02	0.02	<0.02	<0.02	0.02
MgO	14.3	12.7	11.3	9.42	8.80	7.21	5.70	3.52
CaO	0.03	0.02	0.06	0.11	0.03	0.06	0.02	0.10
	100.69	99.43	99.15	99.93	99.17	97.64	98.64	96.22
Fe_2O_3	1.78	1.65	1.70	1.76	6.34	9.73	13.41	21.54
FeO	14.30	16.72	18.97	21.31	22.10	23.94	29.93	34.32
	100.87	99.60	99.32	100.10	99.81	98.61	99.98	98.38
mg	64.1	57.5	51.5	44.1	41.5	34.9	25.3	15.4
Cations based on 24 cations and 32 oxygens								
Si	0.0342	0.0149	0.0175	0.0331	0.0333	0.0294	0.0220	0.1625
Ti	0.1285	0.2169	0.2065	0.1723	0.1233	0.2549	1.2731	1.7812
Al	5.9254	6.1852	6.7398	5.8532	6.0992	5.0031	2.9173	1.6219
Cr	9.2584	8.7474	8.2301	9.2389	8.2204	8.3134	7.5290	5.4610
V	0.1643	0.2950	0.2622	0.1592	0.1458	0.1605	0.1854	0.3258
Fe^{3+}	0.3266	0.3087	0.3200	0.3378	1.2214	1.9544	2.7781	4.7038
Fe^{2+}	2.9178	3.4761	3.9601	4.5385	4.7332	5.3449	6.8904	8.3313
Mn	0.0372	0.0442	0.0423	0.0625	0.0521	0.0543	0.0606	0.0541
Ni			0.0014		0.0041			0.0047
Mg	5.1998	4.7062	4.2042	3.5744	3.3589	2.8680	2.3382	1.5226
Ca	0.0078	0.0053	0.0160	0.0300	0.0082	0.0172	0.0059	0.0311

mg = 100 × Mg/(Mg + Fe^{2+}).
*Total iron as FeO, n.a.: not analysed.
W.d. analyses as Institute of Mineralogy, Copenhagen.
‡ = separate trace element w.d. analyses.

1. Chromite enclosed in olivine phenocryst in unwelded basaltic tuff.
2. Chromite in basaltic glass grain in unwelded basaltic tuff.
3. Chromite enclosed in olivine phenocryst in glassy welded basaltic tuff.
4. Chromite in glassy groundmass.
5. Chromite core in the margin of a pseudomorphosed olivine phenocryst in welded crystalline basaltic hornfels tuff.
6. Early chromite in microcrystalline basaltic matrix.
7. Titanian chromite in the core of olivine in welded crystalline hornfels tuff.
8. Strongly autometamophic equilibrated early chromite rimmed by ilmenite in crystalline basaltic groundmass.

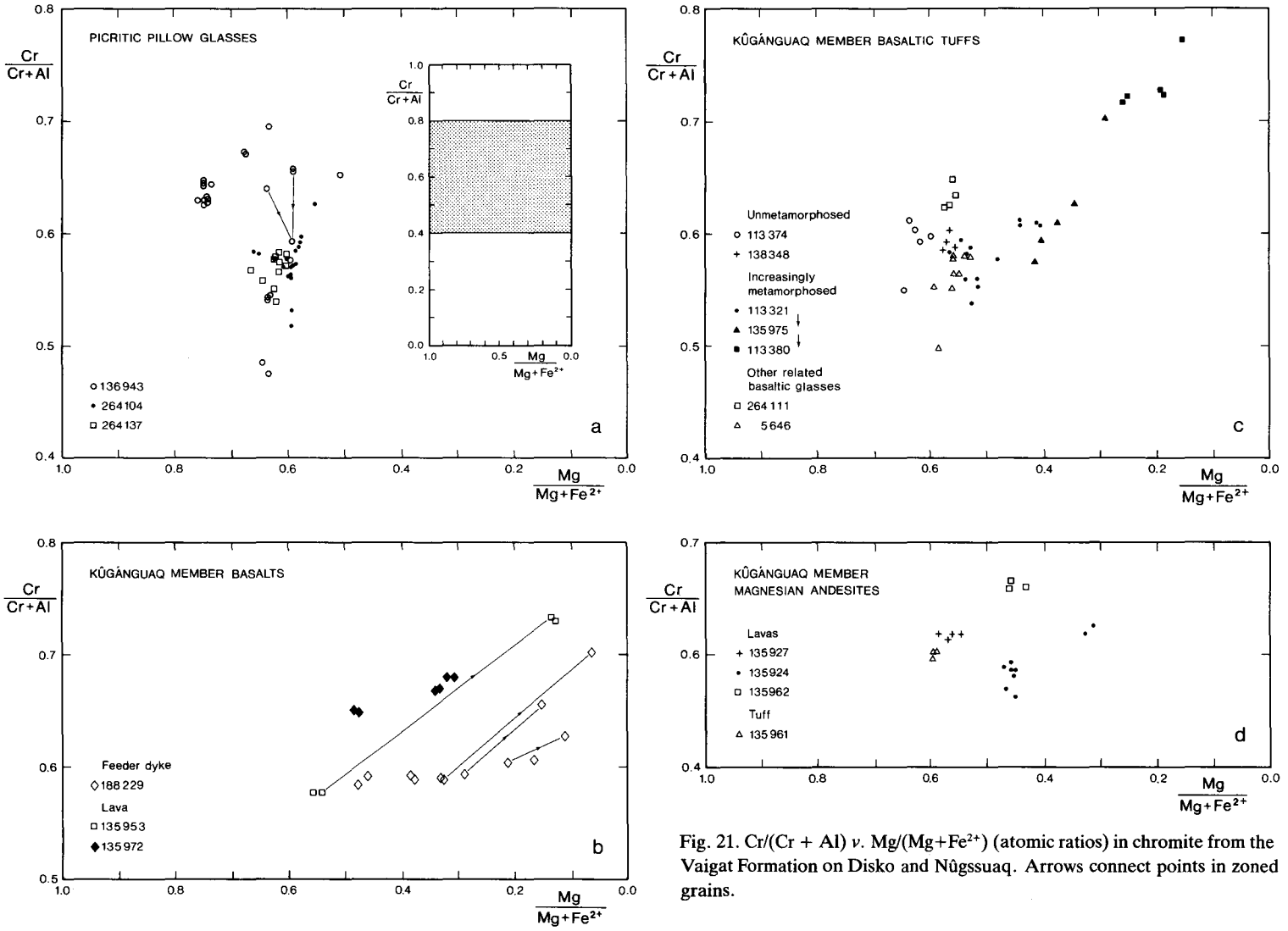

Fig. 21. Cr/(Cr + Al) *v.* Mg/(Mg+Fe^{2+}) (atomic ratios) in chromite from the Vaigat Formation on Disko and Nûgssuaq. Arrows connect points in zoned grains.

glasses have broadly similar major element compositions, but differ markedly in their V and Fe^{3+} contents and ratios (fig. 23). Both features are related to the contrasting T–f_{O_2} regime of crystallization, as discussed later.

The more slowly cooled Kûgánguaq Member chromite from the feeder dyke, from the lavas (Table 8) and from the welded tuffs (Table 6) reveal their different T–f_{O_2} histories by different chemical zonation trends (fig. 22b, c) and tend to retain the characteristically high V content found in the quenched chromites.

The highest V content (V_2O_3 = 1.8%) occurs in chromite in the feldspar-phyric silicic basalt lava (135972), which is also the most V-enriched rock in the Kûgánguaq Member.

The contrasting zoning, which is mainly in terms of Ti and Fe^{3+}, is well illustrated by comparison of the basaltic feeder dyke with the welded tuffs from the tuff shield. Two trends are apparent in the feeder dyke (138229), the first being shown by the cores of the chromites or by entire grains when enclosed in olivine or pyroxene. These chromites display a trend of mostly simple $Mg \rightleftarrows Fe^{2+}$ substitution with only very minor increase in Ti and Fe^{3+} (figs 21 and 24). The second trend is observed when the chromite is in contact with the late groundmass in which it is rimmed by an ulvöspinel-rich titanomagnetite (fig. 24, Table 8, no. 4) which is also the dominant late Fe-Ti oxide. This second trend is characterized by $2Ti/Fe^{3+}$ values $\gg 1$, in contrast to values $\ll 1$ in chromite from the welded tuffs (fig. 24). In the glassy welded tuff (113321) the chromite is not markedly different from that of the unwelded tuffs and glass rocks, but in the basalt hornfels tuffs (135975 and 113380) a strong zonation leads from the original chromite towards compositions with a marked magnetite enrichment with $2Ti/Fe^{3+}$ well below 1.0. Chromite in the magnesian andesite lavas shows distinct individual features (Table 7 and figs 23 and 24). In one lava sample (135927) it appears to be nearly identical to that of the andesitic tuff, except for lower V_2O_3, while in the other lava samples it shows a relative enrichment in Fe^{3+}. The most oxidized andesitic chromites, characterized by $2Ti/Fe^{3+}$ ratios below 0.2, are from andesite lava sample 135962 which shows autometamorphic equilibration textures and is devoid of any immiscible Fe-Ti-Ca-P-silicate melt.

Pyroxenes

In the Kûgánguaq Member rocks orthopyroxene forms scarce phenocrysts in a few basalts, but is invariably present as a phenocryst phase in the andesites. Augite has only been found as a phenocryst phase in the feldspar-phyric silicic basalts, whereas phenocrystic pigeonite appears to be completely absent. The groundmass pyroxenes show a considerable compositional variation. The Kûgánguaq Member pyroxenes closely approach the $(Ca,Mg,Fe^{2+})_2Si_2O_6$ ternary system (except for the very late iron-rich groundmass pyroxenes) (Tables 9 and 10). Calculations of the pyroxene formula based on 6 oxygens indicate that ferric iron must be a very minor

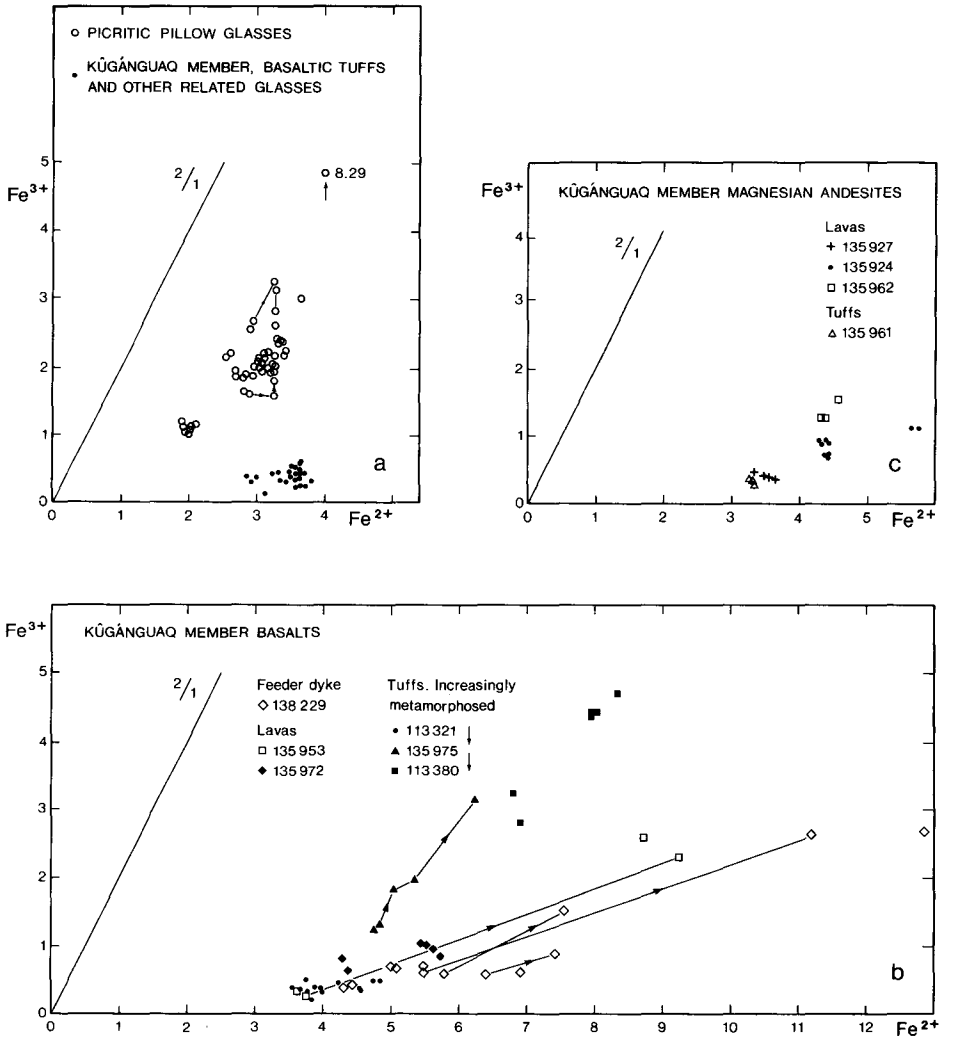

Fig. 22. Fe^{3+} *v.* Fe^{2+} (calculated assuming spinel stoichiometry based on 24 cations and 32 oxygens) in chromites from the Vaigat Formation on Disko and Nûgssuaq. Note that chromite from the quenched Kûgánguaq Member basalts is markedly more reduced than chromite from picritic pillow glasses.

Table 7. Chromites in magnesian andesite lavas and tuffs from the Kûgánguaq Member and in reduced Vaigat Formation basalt glasses

Analysis	1	2	3	4	5	6	7
GGU no.	135961	135927	135924	135924	135962	5646	264110
SiO_2	0.15	0.15	0.14	0.17	0.10	0.10	0.12
TiO_2	0.82	0.82	0.69	2.19	0.45	0.81	1.19
Al_2O_3	20.2	19.7	20.7	16.8	15.7	22.5	18.1
Cr_2O_3	45.4	46.7	43.7	40.5	46.3	43.5	46.7
V_2O_3	0.94	0.64	0.31	0.77	0.32	1.43	1.43
FeO*	17.3	18.7	23.6	30.5	25.8	18.8	19.6
MnO	0.21	0.12	0.24	0.21	0.20	0.24	0.24
NiO	n.a.	n.a.	0.16	n.a.	0.07	n.a.	n.a.
MgO	12.9	12.4	9.80	6.92	9.44	12.2	12.0
CaO	0.01	0.04	0.05	0.11	0.02	0.04	0.10
	97.93	99.27	99.39	98.17	98.40	99.62	99.48
Fe_2O_3	1.88	2.13	3.38	5.55	6.50	1.51	2.53
FeO	15.61	16.79	20.56	25.51	19.96	17.44	17.32
	98.12	99.49	99.73	98.73	99.06	99.77	99.73
mg	59.6	56.8	45.9	32.6	45.7	55.5	55.1
Cations based on 24 cations and 32 oxygens							
Si	0.0379	0.0376	0.0355	0.0452	0.0262	0.0248	0.0303
Ti	0.1556	0.1547	0.1317	0.4374	0.0886	0.1508	0.2261
Al	6.0094	5.8252	6.1921	5.2597	4.8443	6.5684	5.3905
Cr	9.0569	9.2599	8.7659	8.5026	9.5798	8.5155	9.3264
V	0.1902	0.1287	0.0630	0.1640	0.0671	0.2839	0.2896
Fe^{3+}	0.3565	0.4016	0.6446	1.1087	1.2793	0.2810	0.4807
Fe^{2+}	3.2945	3.5210	4.3635	5.6652	4.3680	3.6124	3.6602
Mn	0.0449	0.0255	0.0516	0.0472	0.0443	0.0503	0.0514
Ni			0.0327		0.0147		
Mg	4.8514	4.6351	3.7059	2.7388	3.6821	4.5023	4.5178
Ca	0.0027	0.0108	0.0136	0.0313	0.0056	0.0106	0.0271

$mg = 100 \times Mg/(Mg + Fe^{2+})$.
*Total iron as FeO, n.a.: not analysed.
W.d. analyses as Institute of Mineralogy, Copenhagen.

1. Chromite enclosed in olivine fragment in andesite tuff.
2. Chromite enclosed in pseudomorphosed olivine phenocryst in andesite lava.
3. Core of chromite crystal enclosed in pseudomorphosed olivine phenocryst in andesite lava.
4. Margin of chromite in pseudomorphosed olivine close to reaction rim of orthopyroxene.
5. Chromite enclosed in olivine phenocryst in andesite lava.
6. Chromite in reduced basaltic glass with traces of native iron. Lowermost tuff in sample GGU 5646 from Agatkløft, Nûgssuaq (Pedersen 1978a, p. 120 Fig. 3).
7. Chromite in olivine microporphyritic basalt glass in pillow rim.

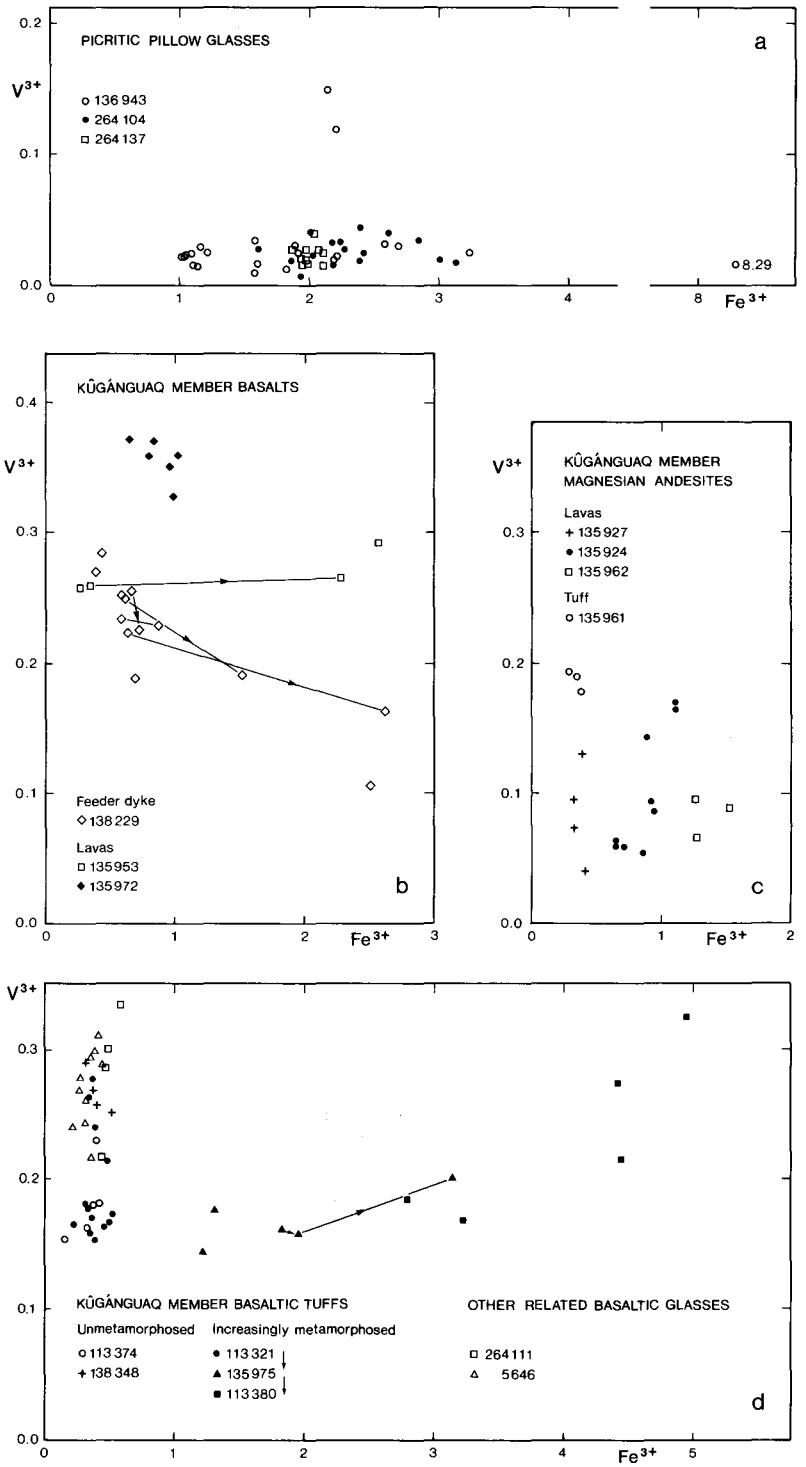
PICRITIC PILLOW GLASSES
a
V3+
o 136 943
• 264 104
□ 264 137
o 8.29
Fe3+
KÛGÁNGUAQ MEMBER BASALTS
b
Feeder dyke
◇ 138 229
Lavas
□ 135 953
◆ 135 972
KÛGÁNGUAQ MEMBER
MAGNESIAN ANDESITES
c
Lavas
+ 135 927
• 135 924
□ 135 962
Tuff
o 135 961
KÛGÁNGUAQ MEMBER BASALTIC TUFFS
Unmetamorphosed
Increasingly metamorphosed
o 113 374
+ 138 348
• 113 321
▲ 135 975
■ 113 380
OTHER RELATED BASALTIC GLASSES
□ 264 111
△ 5646
d

component at most (Tables 9 and 10) and no quantification of the oxidation ratio was therefore attempted. Some pyroxenes from all the three major rock types plot within the pyroxene solvus gap, though to a different extent, and calcic augite is notably absent (figs 26 and 27). Pyroxenes from two olivine-poor tholeiitic basalts from the Vaigat Formation (fig. 26c) are shown for comparison. Inspection of the pyroxene trends in individual rock types reveals the following.

Among the olivine microporphyritic basalts, the feeder dyke (138229) displays the most extensive pyroxene variation (fig. 26a). It contains a few scarce orthopyroxene crystals, *mg* = 80 (Table 9, no. 1), but is dominated by subcalcic augite and pigeonite which tends to show zonation towards more calcic compositions. The most evolved compositions are ferroaugite (*mg* = 36, Table 9, no. 4) which is associated with re-equilibrated former blebs of immiscible Fe-Ti-Ca-P-silicate melt. The hornfels tuff shows the smallest degree of pyroxene zonation, metamorphic equilibration having narrowly constrained the *mg* ratios (*mg* = 78 to 68), and low and high Ca pyroxenes are separated by a wide gap (fig. 26b). The twin-laminated pigeonite rims on olivine show the largest compositional scatter, whereas the late groundmass and vug pyroxenes are fairly calcic augite and Ca-poor orthopyroxene (Table 9, no. 9 and 10).

The lava trends lie between these extremes (fig. 26a). In the most coarse-textured rock (135951) the solvus was effective, and strongly zoned groundmass orthopyroxene (*mg* = 83 to 42) makes up about a third of the groundmass pyroxene.

Coexisting augite (*mg* = 82) and orthopyroxene (*mg* = 81) phenocrysts occur in the feldspar-phyric silicic basalt. The groundmass pyroxenes of this rock include augite, subcalcic augite and pigeonite and show very extensive compositional scatter. Individual pyroxene grains show zonation extending both from pigeonite to augite and from augite towards pigeonite (fig. 26b).

In the magnesian andesites orthopyroxene is the only pyroxene phenocryst phase, and it is the only pyroxene found in the andesite tuff (135961). Some orthopyroxene phenocryst cores (*mg* = 86–85) (Table 10, nos 1 and 2) are the most magnesian pyroxenes found in the Kûgánguaq Member. The orthopyroxene is invariably normally zoned and commonly rimmed by clinopyroxene.

←

Fig. 23. Vanadium (V^{3+}) *v.* ferric iron (Fe^{3+}) (calculated assuming spinel stoichiometry based on 24 cations and 32 oxygens) in chromites from the Vaigat Formation on Disko and Nûgssuaq. Note the following: in (a) the low V, except for one anomalous chromite crystal; in (b) the high V level is retained, or only slightly diminished in Fe^{3+}-enriched margins of the grains; among chromites in the magnesian andesites (c) the considerable variation in both V^{3+} and Fe^{3+} from sample to sample and the V^{3+}-rich and Fe^{3+}-poor chromites in the quenched tuff sample GGU 135961; in (d) the high V^{3+} and low Fe^{3+} which characterize the quenched rocks. Chromites from the metamorphosed tuffs show marked Fe^{3+} enrichment but retain their original high V.

Table 8. Chromite and chromian titanomagnetite from basaltic Kûgánguaq Member rocks

Analysis	1	2	3	4	5	6	7	8
GGU no.	138229	138229	138229	138229	135953	135953	135972	135972
SiO_2	0.11	0.21	0.14	0.44	0.14	0.08	0.09	0.10
TiO_2	1.26	0.90	6.02	24.0	1.03	10.2	1.91	1.70
Al_2O_3	20.6	19.1	12.6	2.38	21.7	7.06	16.2	14.3
Cr_2O_3	43.0	41.8	35.8	5.25	44.1	28.9	44.6	44.8
V_2O_3	1.32	1.19	0.88	0.44	1.29	1.29	1.78	1.64
FeO*	22.0	28.8	40.8	61.9	19.2	47.9	22.9	29.5
MnO	0.21	0.30	0.22	0.31	0.24	0.28	0.23	0.26
NiO	<0.02	0.03	<0.02	0.04	<0.02	<0.02	<0.02	<0.02
MgO	10.3	5.95	3.40	1.13	11.9	3.24	10.0	6.62
CaO	0.07	0.14	0.17	0.25	0.04	0.13	0.34	0.16
	98.87	98.42	100.03	96.14	99.64	99.08	98.05	99.08
Fe_2O_3	1.96	2.97	7.35	11.86	1.30	12.10	3.25	4.76
FeO	20.23	26.13	34.19	51.23	18.03	37.01	19.98	25.21
	99.06	98.72	100.77	97.33	99.77	100.29	98.38	99.55
mg	47.6	28.9	15.1	3.8	54.0	13.5	47.1	31.9
Cations based on 24 cations and 32 oxygens								
Si	0.0280	0.0555	0.0381	0.1323	0.0348	0.0225	0.0235	0.0267
Ti	0.2409	0.1789	1.2336	5.4276	0.1928	2.1603	0.3750	0.3413
Al	6.1745	5.9527	4.0473	0.8437	6.3670	2.3440	4.9863	4.5008
Cr	8.6427	8.7354	7.7112	1.2479	8.6766	6.4342	9.2054	9.4551
V	0.2691	0.2526	0.1917	0.1059	0.2574	0.2912	0.3726	0.3511
Fe^{3+}	0.3760	0.5904	1.5063	2.6827	0.2438	2.5648	0.6387	0.9570
Fe^{2+}	4.3019	5.7771	7.7907	12.8843	3.7526	8.7170	4.3616	5.6295
Mn	0.0452	0.0672	0.0508	0.0790	0.0506	0.0668	0.0509	0.0588
Ni		0.0064		0.0097				
Mg	3.9027	2.3442	1.3806	0.5064	4.4138	1.3599	3.8910	2.6339
Ca	0.0191	0.0397	0.0496	0.0806	0.0107	0.0392	0.0951	0.0458

$mg = 100 \times Mg/(Mg + Fe^{2+})$.
*Total iron as FeO, n.a.; not analysed.
W.d. analyses as Institute of Mineralogy, Copenhagen.

1. Chromite enclosed in pigeonite which rims olivine in basaltic feeder dyke.
2. Core of large chromite surrounded by groundmass.
3. Rim of Ti-enriched chromite around anal. (2).
4. Small chromian titanomagnetite in groundmass.
5. Chromite enclosed in core of early orthopyroxene phenocryst in partially autometamorphosed basalt lava.
6. Reequilibrated titanian chromite, partially enclosed in orthopyroxene rim around pseudomorphosed olivine.
7. Chromite enclosed in plagioclase phenocryst in feldspar-phyric silicic basalt lava.
8. Chromite enclosed in plagioclase phenocryst.

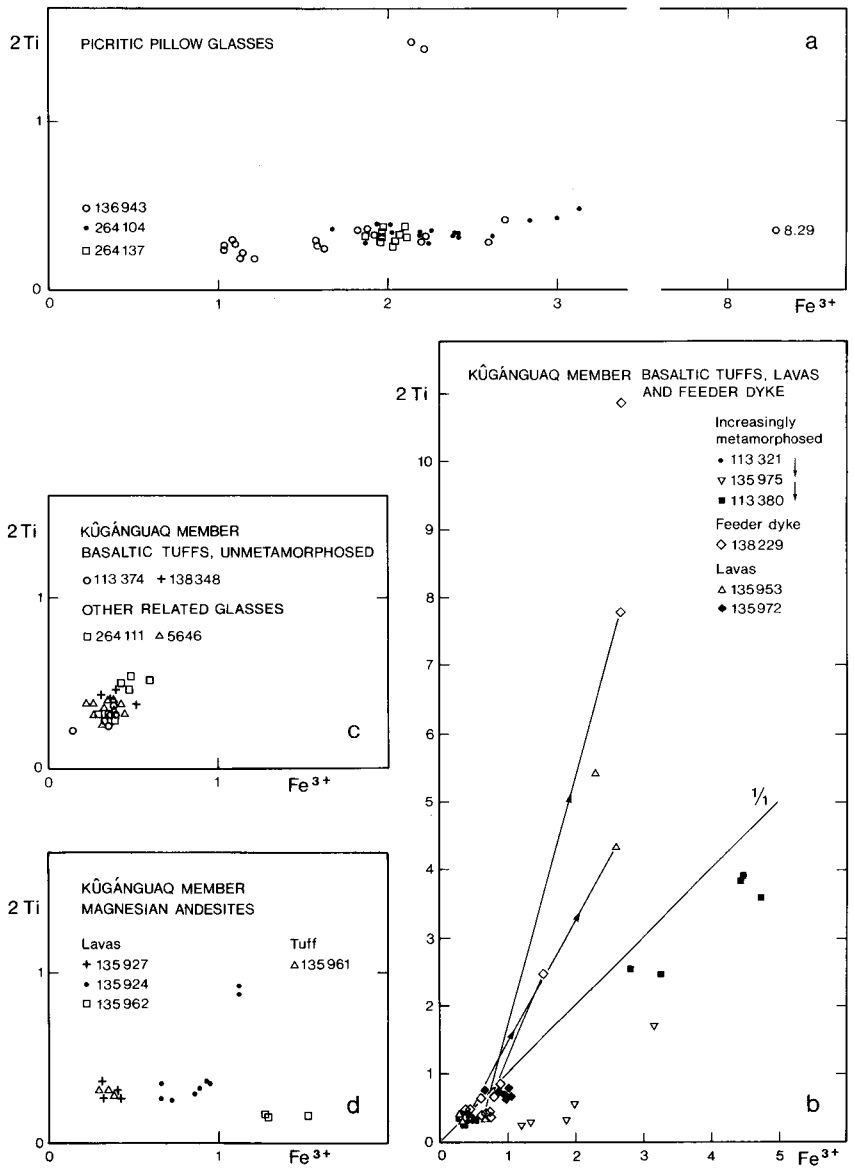

Fig. 24. 2Ti *v.* Fe^{3+} (based on 24 cations and 32 oxygens) in chromites from the Vaigat Formation on Disko and Nûgssuaq. The $2Ti/Fe^{3+}$ ratio shows the rate of M_2TiO_4 to $MFe_2^{3+}O_4$ substitution in the chromites.

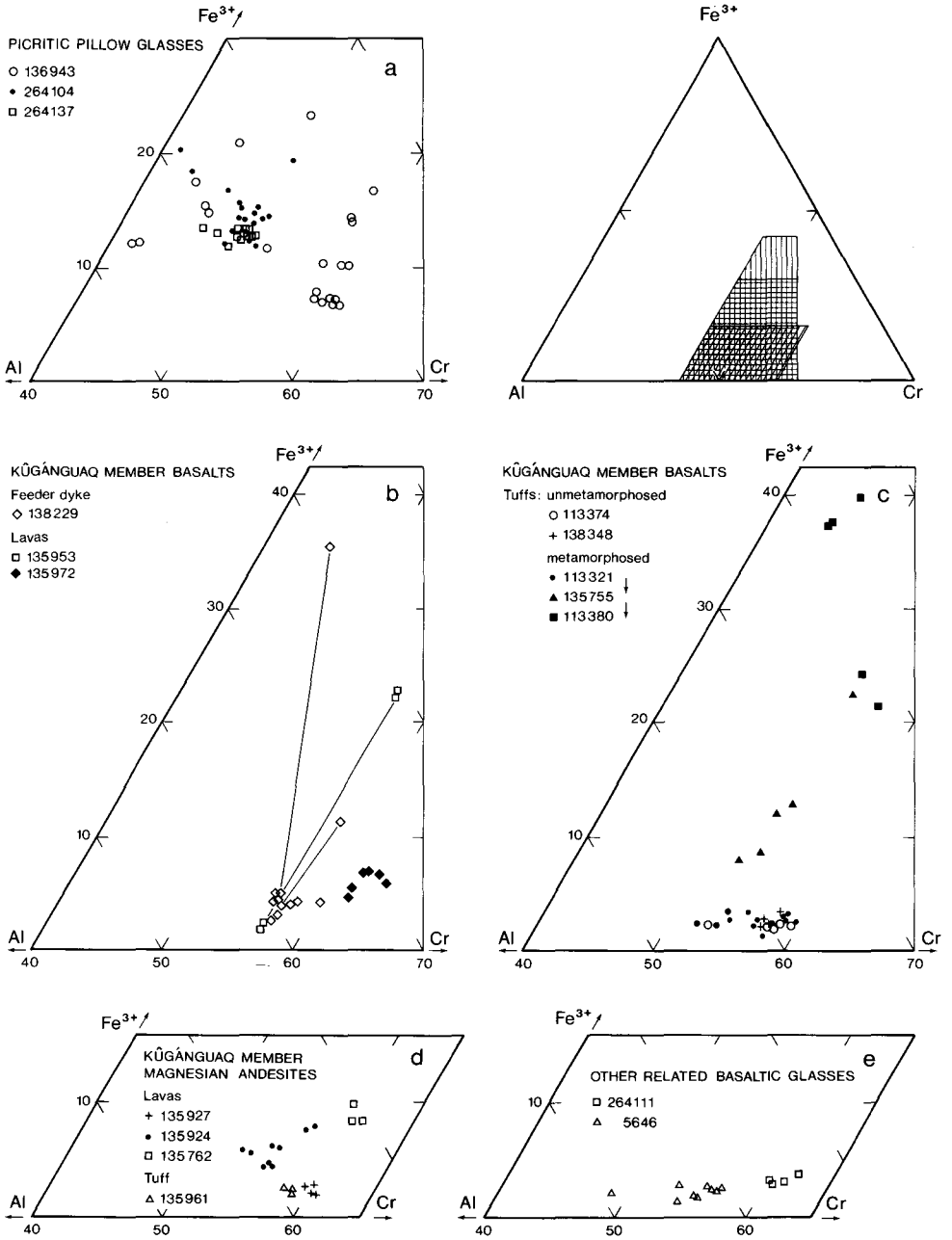

Fig. 25. Al–Cr–Fe^{3+} ratio diagrams for chromite in samples from the Vaigat Formation on Disko and Nûgssuaq. Note in (a) the generally oxidized nature of the chromites in picritic pillow glasses; and in (c) and (d) the reduced nature of chromite from the unmetamorphosed tuff samples from the Kûgánguaq Member and from the related basaltic glasses (e).

Table 9. Pyroxenes from the Kûgánguaq Member basalts

Analysis	1	2	3	4	5	6	7	8	9	10
GGU no.	138229	138229	138229	138229	135953	135972	135972	113380	113380	113380
SiO_2	53.5	53.5	49.8	44.8	56.0	52.8	54.8	53.4	50.9	54.2
TiO_2	0.35	0.42	1.63	3.35	0.31	0.39	0.25	0.65	1.19	0.30
Al_2O_3	2.57	1.61	1.77	3.40	2.34	2.10	1.13	0.99	1.98	0.59
Cr_2O_3	0.79	0.52	<0.05	n.d.	0.98	0.76	0.54	0.24	0.52	0.14
FeO*	11.9	13.7	20.5	22.2	9.61	6.97	12.1	15.9	10.7	18.6
MnO	0.27	0.40	0.22	0.34	0.25	0.21	0.29	0.29	0.22	0.30
MgO	27.7	25.3	13.4	7.09	30.5	18.1	28.8	24.2	16.0	24.9
CaO	2.02	4.14	12.2	16.5	1.57	17.7	2.30	4.03	17.2	1.55
Na_2O	0.07	0.05	0.17	0.5[a]	n.d.	0.18	0.05	0.04	n.d.	0.03
	99.37	99.64	99.69	98.18	101.56	99.21	100.26	99.74	98.71	100.61
mg	80.6	76.7	53.8	36.3	85.0	82.2	80.9	73.1	72.7	70.5
Cations based on 6 oxygens										
Si	1.928	1.944	1.919	1.813	1.940	1.944	1.952	1.956	1.919	1.975
Al^{IV}	0.072	0.056	0.080	0.162	0.060	0.056	0.047	0.043	0.081	0.025
Al^{VI}	0.037	0.013			0.036	0.035			0.007	
Ti	0.009	0.011	0.047	0.102	0.008	0.011	0.007	0.018	0.034	0.008
Cr	0.022	0.015			0.027	0.022	0.015	0.007	0.016	0.004
Fe	0.357	0.416	0.661	0.751	0.278	0.215	0.361	0.487	0.337	0.567
Mn	0.008	0.012	0.007	0.012	0.007	0.007	0.009	0.009	0.007	0.009
Mg	1.482	1.370	0.769	0.428	1.575	0.993	1.529	1.321	0.899	1.352
Ca	0.078	0.161	0.504	0.716	0.058	0.698	0.088	0.158	0.695	0.061
Na	0.005	0.004	0.013	0.039		0.013	0.003	0.003		0.002
	3.998	4.002	4.000	4.023	3.989	3.994	4.011	4.002	3.995	4.003

*Total iron as FeO.
mg = 100 × Mg/(Mg + Fe^{2+}).
a: analytical value probably too high.

Analyses 1 to 3: W.d. analyses, Institute of Mineralogy, Copenhagen.
Analyses 4 and 5: E.d. analyses, Institute of Mineralogy, Copenhagen.
Analyses 6 to 8 and 10: W.d. analyses, Grant Institute of Geology, Edinburgh.
Analysis 9: E.d. analysis, Research School of Earth Sciences, Canberra.

1. Early orthopyroxene in basaltic feeder dyke.
2. Early groundmass pigeonite in basaltic feeder dyke.
3. Subcalcic augite from the groundmass in basaltic feeder dyke.
4. Late groundmass calcic clinopyroxene intergrown with titanomagnetite. Associated with late immiscible mafic blebs.
5. Orthopyroxene phenocryst with enclosed chromite from basalt lava.
6. Augite phenocryst core in feldspar-phyric silicic basalt.
7. Orthopyroxene phenocryst core in feldspar-phyric silicic basalt.
8. Pigeonite rim on olivine phenocryst in basaltic hornfels tuff.
9. Late augite from vug in basaltic hornfels tuff.
10. Euhedral late orthopyroxene grown in vug in basaltic hornfels tuff (Fig. 16c).

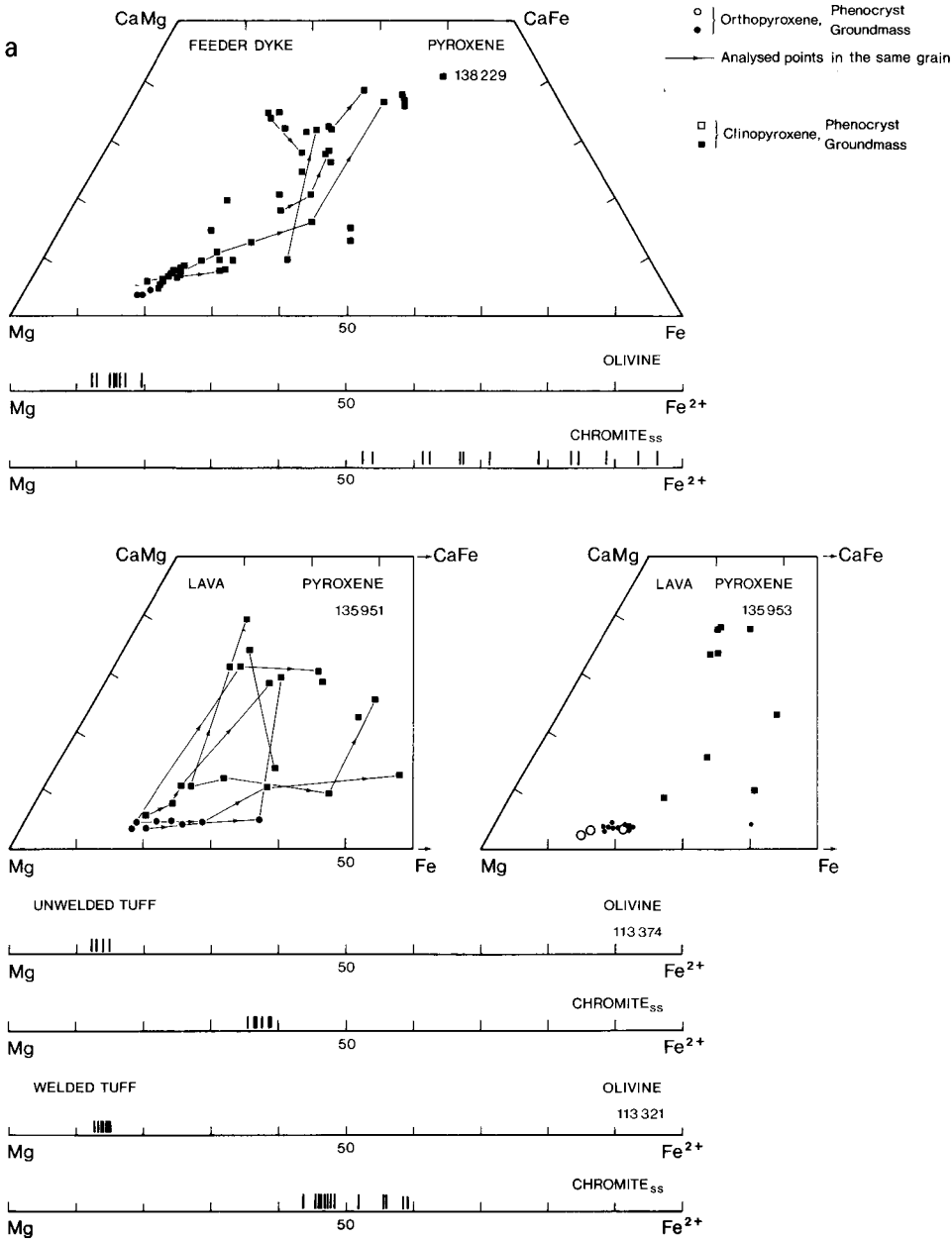

Fig. 26. Ca–Mg–Fe and Mg–Fe atomic ratio diagrams showing compositional variations of pyroxene, olivine and chromite. Arrows connect points in zoned grains. a: Olivine microporphyritic basalts from the Kûgánguaq Member.

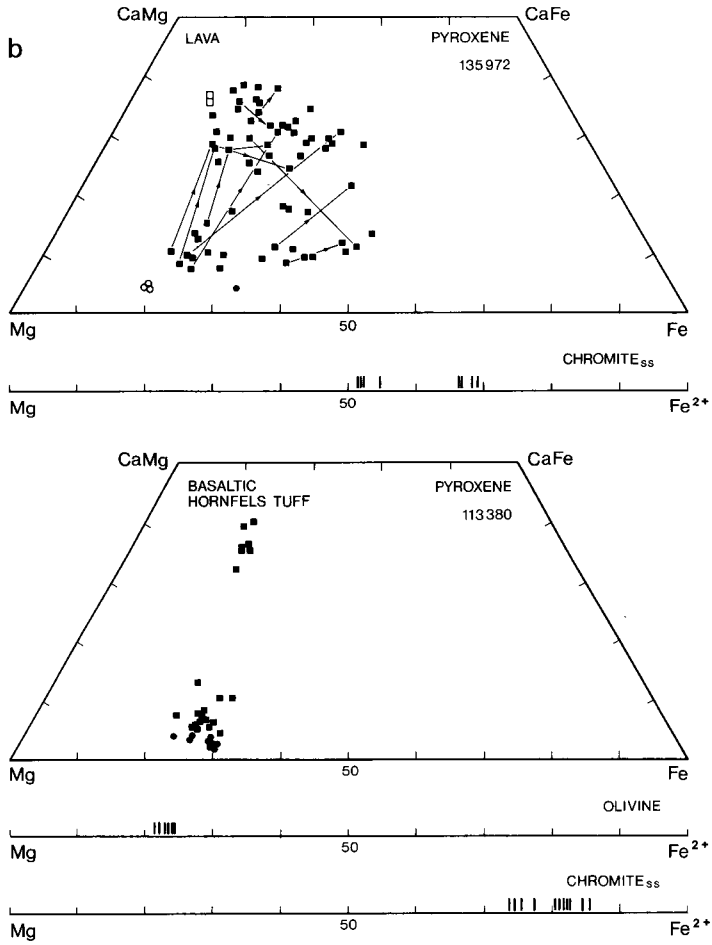

Fig. 26 *cont.* b: Basaltic hornfels tuff and feldspar-phyric silicic basalt from the Kûgánguaq Member.

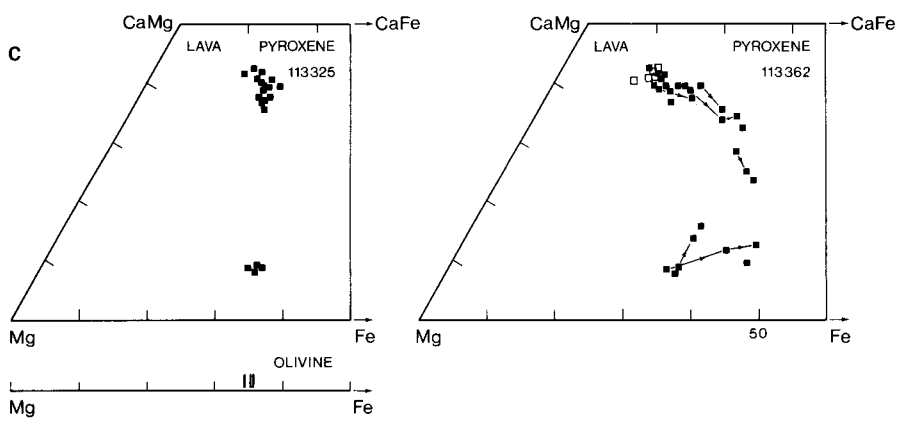

Fig. 26 *cont.* c: Olivine-poor tholeiitic basalt lavas from the Vaigat Formation. Note that the pyroxenes have re-equilibrated in sample GGU 113325.

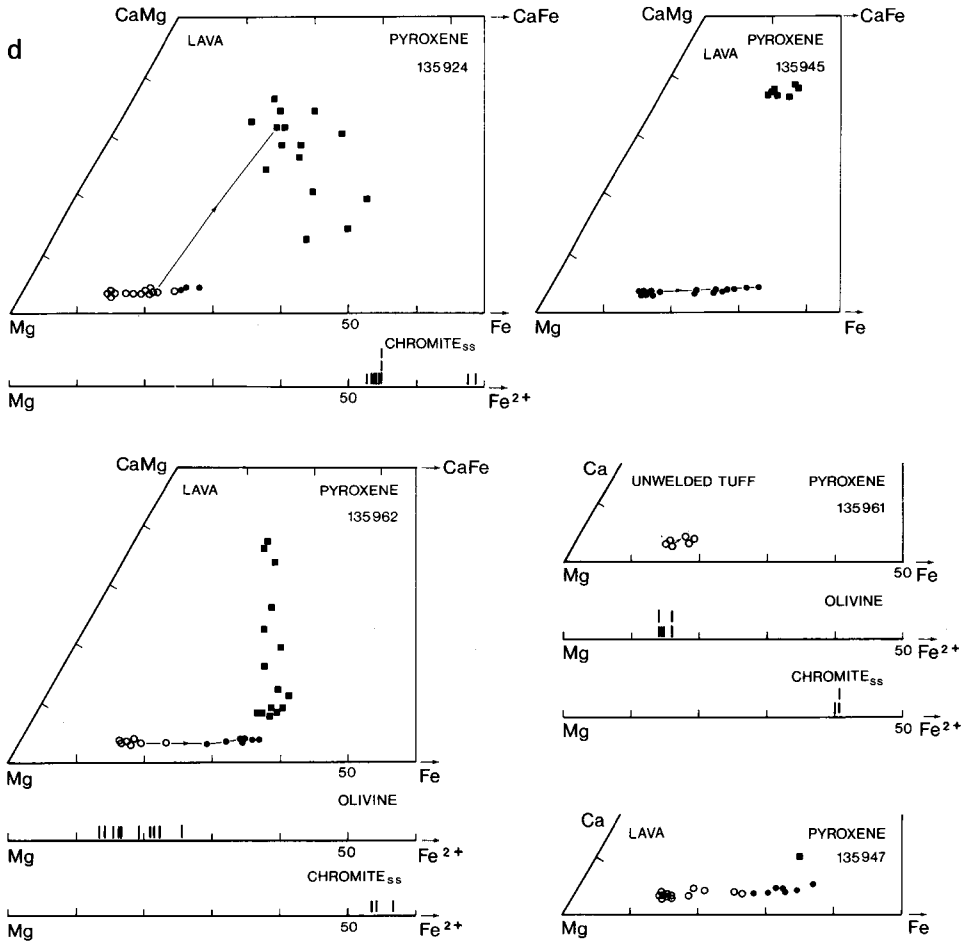

Fig. 26 *cont.* d: Magnesian andesite lava and unwelded tuff from the Kûgánguaq Member.

In the rapidly cooled samples (e.g. 135924) the groundmass pyroxenes scatter widely in composition (fig. 26d) and are Ca-poor augite, subcalcic augite and pigeonite, while in the coarsest sample (135945) they are separated by a wide compositional gap (fig. 26d). In the partly autometamorphosed andesite (135962) the groundmass pyroxenes straddle the solvus (fig. 26d), but their *mg* ratio appears to be narrowly constrained around *mg* = 65 (Table 10, nos 7 and 8).

Calcic augite predominates over pigeonite, and orthopyroxene is absent in the two Vaigat Formation uncontaminated olivine-poor tholeiitic basalts investigated (fig. 26c). In one sample (113325) from the Naujánguite Member the pyroxenes show a wide solvus gap and a narrow range in *mg* (75 to 65), controlled by re-equilibration during cooling, which also affected the olivine phenocrysts (fig. 26c). In the

Table 10. Pyroxenes from the Kûgánguaq Member andesites

Analysis	1	2	3	4	5	6	7	8
GGU no.	135961	135924	135924	135924	135924	135962	135962	135962
SiO_2	54.7	54.9	54.3	50.0	51.0	53.2	52.6	51.8
TiO_2	0.18	0.17	0.42	1.49	0.66	0.40	0.58	0.88
Al_2O_3	2.52	2.27	1.15	1.63	0.62	0.90	0.72	1.50
Cr_2O_3	0.97	0.94	0.32	0.14	n.d.	0.16	0.05	0.20
FeO*	8.88	8.55	14.9	16.5	25.6	20.4	16.5	12.3
MnO	0.15	0.15	0.25	0.40	0.44	0.34	0.26	0.22
MgO	30.6	30.1	26.2	12.5	14.7	22.2	17.8	15.2
CaO	1.65	1.69	2.03	16.1	6.74	1.97	10.8	17.4
Na_2O	0.03	0.07	n.d.	0.4	0.05	0.03	0.07	0.15
	99.68	98.84	99.57	99.16	99.81	99.60	99.38	99.68
mg	86.0	86.2	75.8	57.4	50.6	66.0	65.8	68.8
Cations based on 6 oxygens								
Si	1.928	1.947	1.968	1.927	1.974	1.978	1.978	1.946
Al^{IV}	0.072	0.053	0.032	0.073	0.026	0.022	0.022	0.054
Al^{VI}	0.033	0.042	0.017	0.001	0.002	0.017	0.010	0.012
Ti	0.005	0.005	0.011	0.043	0.019	0.011	0.016	0.025
Cr	0.027	0.026	0.009	0.004		0.005	0.001	0.006
Fe	0.262	0.254	0.452	0.532	0.829	0.634	0.519	0.386
Mn	0.004	0.005	0.008	0.013	0.014	0.011	0.008	0.007
Mg	1.607	1.591	1.415	0.718	0.848	1.230	0.997	0.851
Ca	0.062	0.064	0.079	0.665	0.279	0.078	0.435	0.700
Na	0.002	0.005		0.030	0.004	0.002	0.005	0.011
	4.002	3.992	3.991	4.006	3.995	3.988	3.991	3.998

*Total iron as FeO.
mg = 100 × Mg/(Mg + Fe^{2+}).
Analyses 1 and 6 to 8: W.d. analyses, Institute of Mineralogy, Copenhagen.
Analysis 2: W.d. analysis, Grant Institute of Geology, Edinburgh.
Analyses 3 to 5: E.d. analyses, Institue of Mineralogy, Copenhagen.

1. Core of skeletal orthopyroxene microphenocryst in tuff.
2. Core of orthopyroxene phenocryst in lava.
3. Margin of orthopyroxene microphenocryst in lava.
4. Subcalcic augite in groundmass in lava.
5. Pigeonite in groundmass in lava.
6. Outermost margin of orthopyroxene microphenocryst in lava.
7. Subcalcic augite in groundmass in lava.
8. Augite in groundmass in lava.

other sample (113362) from the Qordlortorssuaq Member, microphenocrystic augite (*mg* = 80 to 75) occurs and the groundmass pyroxenes are strongly zoned (*mg* = 78 to 50). Comparison of normative pyroxene compositions (fig. 28) from Kûgánguaq Member rocks and from the uncontaminated olivine-poor tholeiitic basalts from the Vaigat Formation demonstrates that the pyroxene crystallization (figs 26 to 27) is in accordance with the normative mineralogy.

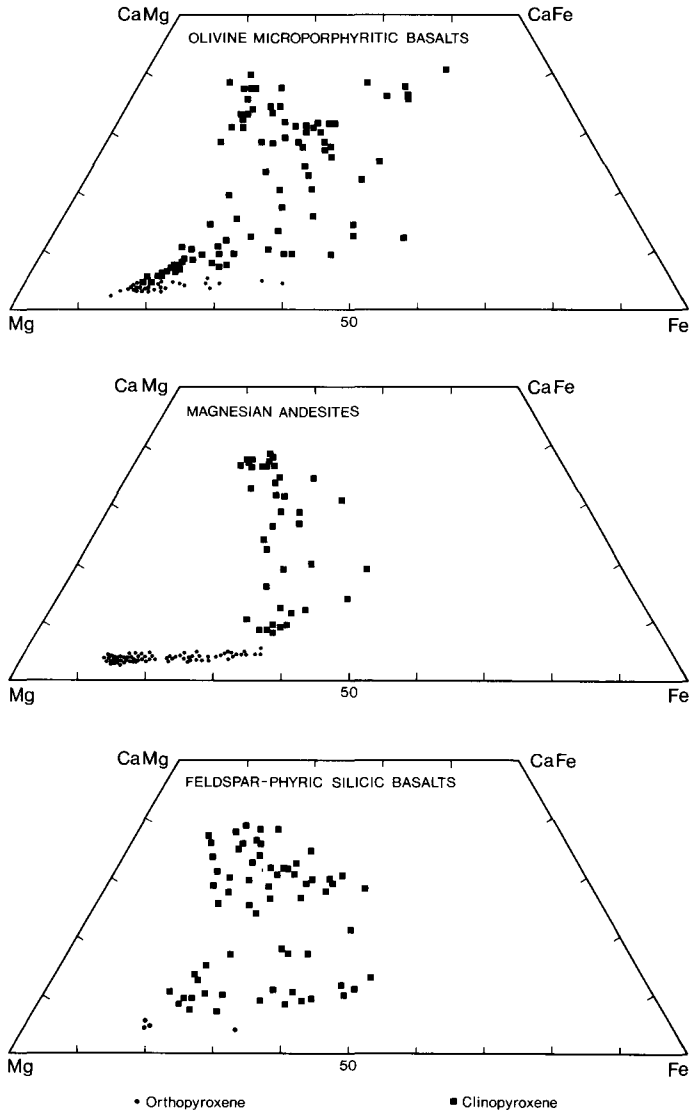

Fig. 27. Ca–Mg–Fe atomic ratio diagram showing all analysed pyroxenes from the Kûgánguaq Member.

Minor elements in pyroxene

Cr decreases rapidly with decreasing *mg* (fig. 29) and is clearly higher in clinothan in orthopyroxene at similar *mg* levels. The highest Cr_2O_3 values (about 1.1 wt.%) occur in the core zones of orthopyroxene phenocrysts in the magnesian andesites. Up to 760 ppm V_2O_3 has been found in a few orthopyroxene phenocrysts in the andesites, but the variations have not been investigated further.

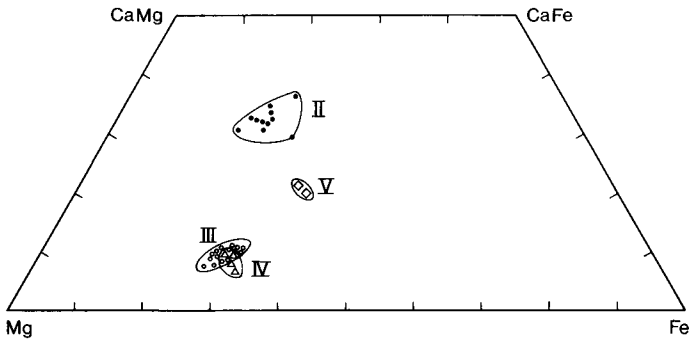

Fig. 28. Cation-normative mineralogy of the following rock types. II: Olivine-poor tholeiitic basalts from the Vaigat Formation. III–V: Rocks from the Kûgánguaq Member, III: Olivine microporphyritic basalts, IV: Magnesian andesites, V: Feldspar-phyric silicic basalts.

Ti is generally low in both clino- and orthopyroxenes and tends to increase with decreasing *mg*, exemplified in fig. 30 by the feldspar-phyric contaminated basalt (135972). Ti is distinctly higher in clino- than in orthopyroxenes and reaches the highest values (> 3.0% TiO_2) in late stage ferroaugite associated with the immiscible mafic blebs in the basaltic feeder dyke.

Tables 9 and 10 show that Al is predominantly found as Al^{IV} in both ortho- and clinopyroxene, whereas Al^{VI} is below 0.04 cations per 6 oxygens. The early orthopyroxene phenocrysts typically (e.g. Table 10, no. 2) contain around 6 mol.% of Tschermacks molecule ($M^{2+}(Al,Cr)^{VI}Al^{IV}Si$) and only around 0.5% Ti-Tschermacks molecule ($CaTi^{4+}(Al)_2^{IV}$) while the amount of jadeite-cosmochlore ($Na(Al,Cr)^{VI}Si_2$) is very small. Al_2O_3 content has strongly declined in the late orthopyroxenes, particularly in late orthopyroxene in vugs in the basaltic hornfels tuff (Table 9, no. 10). In the clinopyroxenes 3.5% Tschermacks molecule has been found, together with only 1% Ti-Tschermacks molecule, in the early augite phenocryst phase in the feldspar-phyric silicic basalts. With decreasing *mg*, Ti tends to increase, $(Al,Cr)^{VI}$ decreases and almost all the Al seems to be present in the Ti-Tschermacks molecule which may constitute between 5 and 9% of the pyroxene. This is seen as a strong clustering around the line $Ti/Al^{total} = 0.5$ (fig. 31).

With further decreasing *mg* Ti tends to exceed Al/2 as in the late ferroaugite in the feeder-dyke (fig. 31a, Table 9, no. 3 and 4). This is unusual for pyroxenes from terrestrial basalts and indicates that another type of Ti-substitution may be involved. Unfortunately, Na (and hence the stoichiometry and Fe^{3+}/Fe^{2+} ratios), is poorly determined by energy dispersive analysis in these late tiny pyroxene crystals, and the Ca–Na–Ti–Fe–Si substitutions involved have therefore not been unequivocally determined.

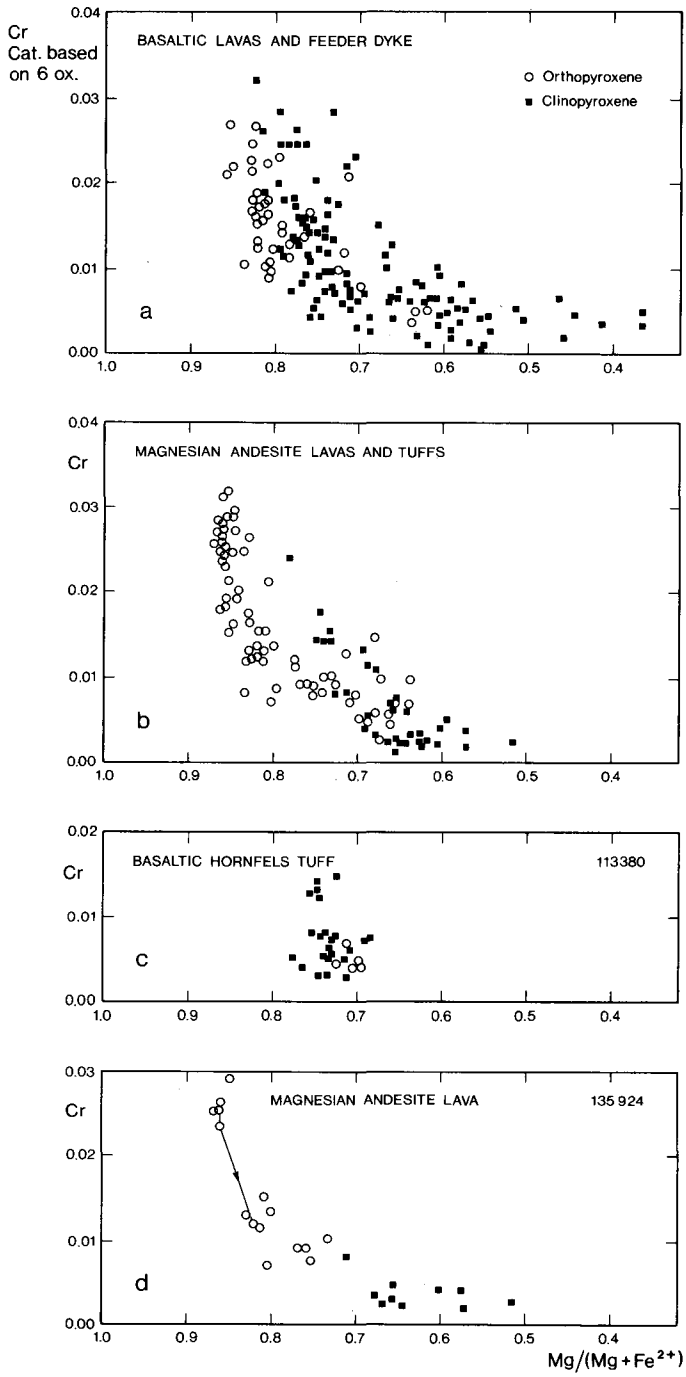

Fig. 29. Cr *v.* Mg/(Mg+Fe^{2+}) diagram (cations based on 6 oxygens) for pyroxenes in samples from the Kûgánguaq Member.

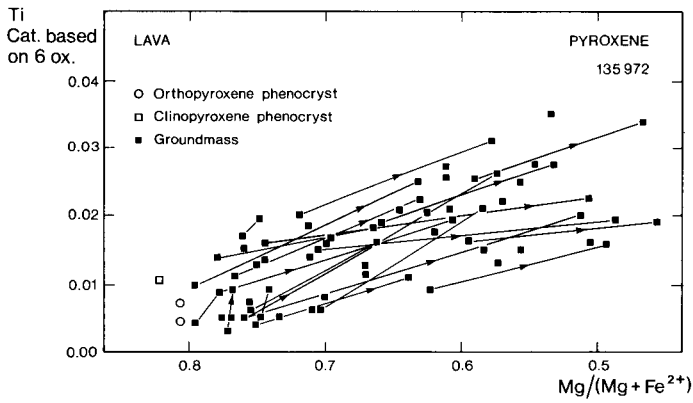

Fig. 30. Ti *v.* Mg/(Mg+Fe^{2+}) diagram (cations based on 6 oxygens) for pyroxenes from the feldspar-phyric silicic basalt lava, sample GGU 135972.

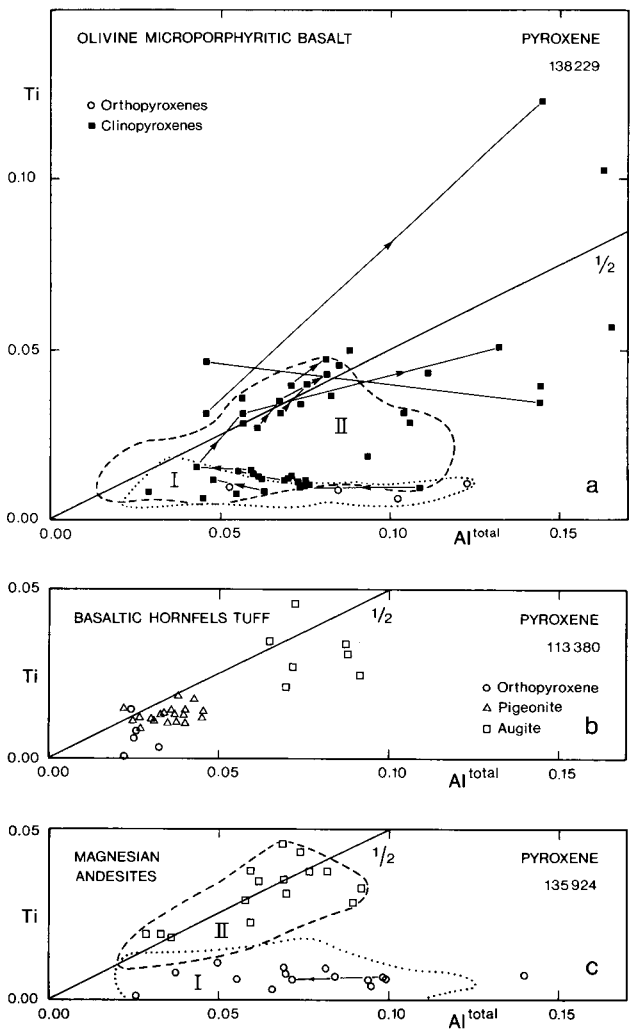

Fig. 31. Ti *v.* Al^{total} diagram (cations based on 6 oxygens) for pyroxenes from the Kûgánguaq Member. Arrows connect points in zoned grains. a: Olivine microporphyritic basalts. Feeder dyke (sample GGU 138229). Field I (stippled): Orthopyroxenes, II (dashed): clinopyroxenes from the olivine microporphyritic basalt lavas. b: Basaltic hornfels tuff (GGU 113380) with orthopyroxene, pigeonite and augite. Note the low Al-content in the orthopyroxene which has crystallized under autometamorphic conditions. c: Magnesian andesite lava (GGU 135924). Field I (stippled): Orthopyroxene (except for one anomalous grain), II (dashed): clinopyroxene in magnesian andesite lavas and one tuff.

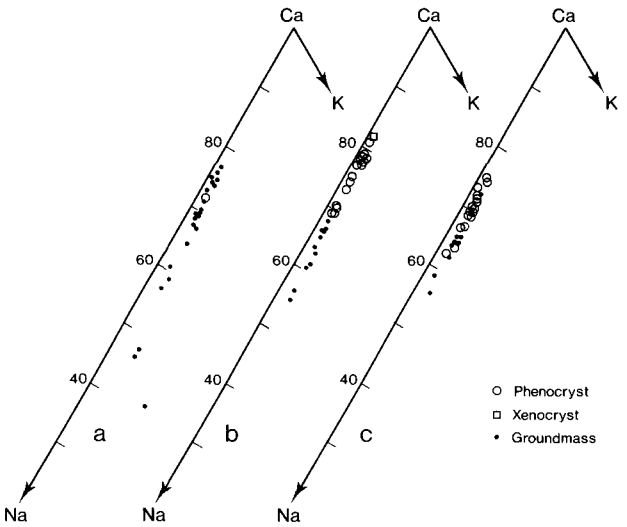

32. Ca–Na–K cation ratio diagrams for plagioclase from the Kûgánguaq Member samples. a: Olivine microporphyritic basalts. b: Feldspar-phyric silicic basalts. c: Magnesian andesites.

Plagioclase

The compositional variation of plagioclase in Kûgánguaq Member rocks is summarized in fig. 32. Plagioclase is absent as a phenocryst phase in the quenched olivine microporphyritic basalts and present as very scarce microphenocrysts in less rapidly cooled rocks. The microphenocrysts grade into the groundmass grains, which all show normal zoning. Plagioclase compositions range from $Ca_{76}Na_{23}K_1$ to $Ca_{45}Na_{51}K_4$ in the most coarsely crystalline rocks whereas the range is less in the more rapidly cooled rocks. In a single sample (135956) more sodic plagioclase ($Ca_{36}Na_{54}K_{10}$) and sanidine ($Ca_7Na_{29}K_{64}$) have been observed as late rims and plates. Such highly evolved compositions may be present in several samples.

In the feldspar-phyric silicic basalt the abundant plagioclase phenocrysts show oscillatory zoning. Compositions range from $Ca_{80}Na_{19}K_1$ to $Ca_{68.5}Na_{30}K_{1.5}$ with total oscillations of about 5% Ca-units. A single investigated grain of a sieve-textured

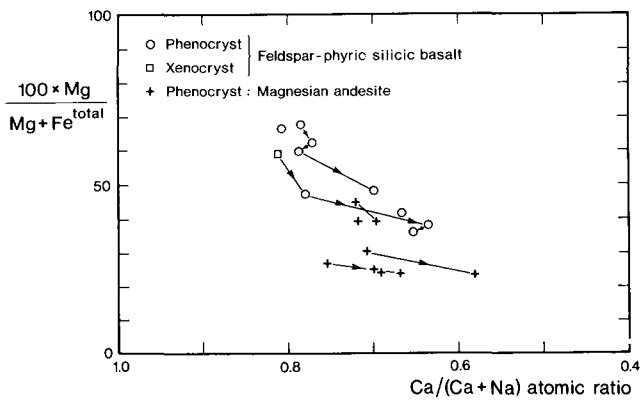

Fig. 33. 100 × Mg/(Mg + Fe^{total}) *v.* Ca/(Ca + Na) diagram (cation ratios) in plagioclase from the Kûgánguaq Member. Arrows point from the cores of grains towards their margins and also show a decline in *mg* when the major elements display oscillatory zoning.

plagioclase xenocryst is calcic in the core ($Ca_{81}Na_{18}K_1$) and more sodic at the margin, while the groundmass plagioclase extends from Ca_{68} to Ca_{54} and shows normal zoning.

In the magnesian andesites plagioclase is invariably present as microphenocrysts which range in composition from $Ca_{74.5}Na_{24.0}K_{1.5}$ to $Ca_{66}Na_{32}K_2$. The groundmass plagioclase grades from this value down to Ca_{54} and probably further, but the latest crystallized plagioclase is too fine-grained to allow quantitative analysis.

In all the investigated plagioclase crystals *mg* falls from core to the margins, also where the major elements show oscillatory zoning (fig. 33). The range found is between *mg* = 68 and 24 (only the wavelength dispersive microprobe analyses have been considered).

Fe-Ti oxides

Scarcity in Fe-Ti oxides is a characteristic feature of the Kûgánguaq Member rocks. The most widespread Fe-Ti oxide is ilmenite, which is present in all rocks except the unwelded tuffs. Titanomagnetite is present as a very minor constituent in the basaltic lavas and in the feeder dyke, and appears to be an important part of the late stage mafic immiscible blebs. Armalcolite has been carefully searched for but not found. Some tiny needles in the rhyolitic glass in andesite sample 135962 are characterized by a high Fe:Ti ratio and may belong to the ferro-ferri pseudobrookite series, but could not be unequivocally identified due to their minute size.

Small oxidized and fractured groundmass oxide grains in the feldspar-phyric silicic basalt (135972) form aggregates which probably contain pseudobrookite. One analysis (Table 11, no. 5) has been calculated on such a basis (3 cations to 5 oxygens) and fits the ferripseudobrookite formula. Rutile has not been identified, but may occur in oxidized aggregates in the same sample.

In contrast to ilmenite from the native iron bearing andesites and dacites, which are very poor in Fe_2O_3, and some of which contain excess TiO_2 (Pedersen, 1981), the Kûgánguaq Member ilmenites (Table 11) all contain Fe^{3+} which, when calculated on the basis of 4 cations and 6 oxygens, amounts to between 1.5 wt.% and 20 wt.% Fe_2O_3. Al_2O_3 is very low in the wavelength dispersive microprobe analyses, whereas Cr_2O_3 varies from 0.1 to 1.6%. MgO varies considerably (*mg* = 1.5 to 20, corresponding to between 0.5 and 5.4% MgO) whereas Mn is invariably low (0.3–1.0% MnO). The major variations are shown in fig. 34. The few ilmenite analyses from basaltic lavas show minimum contents of MgO and Fe_2O_3 and clearly record near-solidus crystallization. The ilmenite from the basaltic hornfels tuff is distinctly MgO and Cr_2O_3-enriched, while Fe_2O_3 is comparatively low.

Ilmenite in the magnesian andesites occurs only in the groundmass and is clearly enriched in *mg*, and in particular in Fe_2O_3. This is seen in both wavelength dispersive and energy dispersive microprobe analyses from three different laboratories and must express the fact that f_{O_2} was definitely not graphite controlled in the groundmass stage (see Pedersen, 1981).

Table 11. Fe-Ti oxides from the Kûgánguaq Member rocks

Analysis	1	2	3	4	5	6	7	8
GGU no.	138229	113380	113380	135972	135972	135947	135962	135945
SiO_2	0.70	0.03	0.30	2.17	2.91	n.a.	0.41	n.a.
TiO_2	26.6	51.4	50.4	30.4	33.5	48.2	47.4	49.1
Al_2O_3	1.89	0.08	0.07	2.20	3.02	0.58	0.16	0.13
Cr_2O_3	0.10	1.64	1.21	0.29	0.08	<0.10	0.69	0.49
FeO*	65.6	40.5	42.8	56.3	48.1	45.7	44.7	45.1
MnO	0.60	0.34	0.53	3.92	0.68	0.54	0.42	0.98
MgO	0.46	5.16	2.97	0.49	0.05	2.80	3.24	2.34
CaO	<0.05	0.11	0.09	0.36	0.87	0.42	0.15	<0.05
	95.95	99.26	98.37	96.13	89.21	98.24	97.17	98.14
Fe_2O_3	11.95	4.36	3.40		50.79†	9.37	8.86	6.79
FeO	54.84	36.58	39.74		2.40	37.27	36.72	38.99
	97.14	99.70	98.71		94.30	99.18	98.05	98.82
mg	1.5	20.1	11.8		3.5	11.8	13.6	9.7
Cations	24 c.	4 c.	4 c.		3 c.†	4 c.	4 c.	4 c.
	32 ox.	6 ox.	6 ox.		5 ox.	6 ox.	6 ox.	6 ox.
Si	0.2125	0.0015	0.0150		0.1187		0.0206	
Ti	6.0722	1.8847	1.8950		1.0278	1.8072	1.7931	1.8579
Al	0.6763	0.0046	0.0041		0.1452	0.0341	0.0095	0.0077
Cr	0.0240	0.0632	0.0478		0.0026		0.0274	0.0195
Fe^{3+}	2.7304	0.1600	0.1281		1.5591	0.3515	0.3356	0.2571
Fe^{2+}	13.9223	1.4914	1.6614		0.0820	1.5539	1.5449	1.6406
Mn	0.1543	0.0140	0.0224		0.0235	0.0228	0.0179	0.0418
Mg	0.2081	0.3749	0.2213		0.0030	0.2080	0.2429	0.1755
Ca		0.0057	0.0048		0.0380	0.0224	0.0081	
	18.4						$\frac{(M^{2+}Fe_2^{3+}O_4)}{M^{2+}Fe_2^{3+}O_4 + M_2^{2+}TiO_4}$	
$\frac{Fe_2^{3+}O_3}{Fe_2^{3+}O_3 + Fe^{2+}TiO_3}$	5.1	3.7				10.2	9.8	7.3

n.a. not analysed.
*Total iron as FeO.
† This calculation only demonstrates that analysis 5 can be calculated on a pseudobrookite basis.

Analyses 2 and 8: W.d. analyses, Institute of Edinburgh.
Analysis 5: W.d. analysis, Institute of Mineralogy, Copenhagen.
Analyses 1, 3, 4, 6 and 7: E.d. analyses at Research School of Earth Sciences, Canberra (nos. 3, 4 and 6) and Institute of Mineralogy, Copenhagen (nos. 1 and 7).

1. Late tiny titanomagnetite from the groundmass in basaltic feeder dyke.
2. Ilmenite rim on titanochromite in basaltic hornfels tuff.
3. Groundmass ilmenite projecting into vug in basaltic hornfels tuff.
4. Small oxidized groundmass Fe-Ti oxide grain in feldspar-phyric silicic basalt.
5. Another grain as 4.
6. Groundmass ilmenite in magnesian andesite lava.
7. Groundmass ilmenite in magnesian andesite lava.
8. Groundmass ilmenite in magnesian andesite lava.

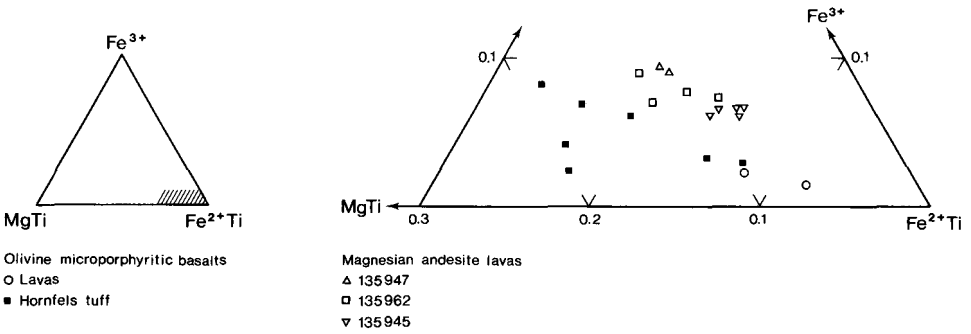

Fig. 34. $MgTi–Fe^{2+}Ti–Fe^{3+}$ cation ratio diagram for ilmenites in some Kûgánguaq Member samples.

Only a single analysis of groundmass titanomagnetite is given in Table 11, no. 1. It represents the late groundmass stage in the basaltic feeder dyke and is probably not very different from the small skeletal oxide crystals found within the immiscible mafic blebs which are too small for analysis. The oxide closely approaches the system $Fe_2TiO_4–FeFe_2O_4$ (*mg* is only 1.5) and is characterized by a very high ulvöspinel component. It differs, however, from the ulvöspinel described from the iron-bearing locality of Uivfaq, south Disko, which appears to be devoid of ferric iron (Bird *et al.*, 1981; Medenbach & ElGoresy, 1982). No titanomagnetite analyses have been obtained from the magnesian andesites.

Zeolites

Zeolites occur in the vesiculated parts of some lavas, and in particular in the matrix of non-welded tuffs. The Kûgánguaq Member rocks are generally much poorer in zeolites than the enclosing picrite lavas. Zeolites from two tuffs (113374 and 135961) and one lava (135972) (Table 12) are characterized by Si/Al ratios above 1.8, and plot close to the line Si+Al = 36 (cations based on 72 O). They also show approximately 2Ca+K+Na = Al (fig. 35) and thereby fulfil the stoichiometric requirements for most zeolites.

In the olivine microporphyritic basalt tuff sample 113374 the zeolite compositions cluster around the ratio $Ca_1Na_1K_1$ (fig. 35a), although some are distinctly less potassic. Among the analysed phases optical examination by O. Jørgensen identified phillipsite (Table 12, no. 4) as radiating aggregates growing around the margins of, and sometimes filling, vesicles, and potassic heulandite as fairly coarse grains which entirely fill vesicles.

In the andesite tuff (sample 135961) the zeolites are found as fairly coarse blades filling vesicles, and show cation ratios of about $Ca_2Na_0K_1$ (Table 12, no. 5).

In the feldspar-phyric silicic basalt lava (sample 135972) colourless, optically isotropic, very fine-grained, zeolite-like aggregates occur as the intermediate zone in vesicles between smectite along the margins and quartz in the core. The aggregates

Table 12. Zeolites from the Vaigat Formation

Analysis	1	2	3	4	5	6
GGU No.	113325	138228	113374	113374	135961	135972
SiO_2	46.7	50.5	53.1	51.7	60.0	83.0
Al_2O_3	26.8	21.9	20.7	23.5	18.1	4.84
FeO*					0.11	
MgO	0.23			0.21	0.15	0.49
CaO	12.3	10.0	7.91	6.45	7.68	2.08
Na_2O	2.01	0.82	2.10	2.22	0.14	0.44
K_2O	0.44	0.71	0.88	5.84	3.47	0.27
	88.48	83.93	84.69	89.92	89.65	91.12
Cations based on 72 oxygens						
Si	21.479	23.970	24.846	23.551	26.519	33.551
Al	14.532	12.255	11.419	12.620	9.431	2.307
Fe^{2+}					0.041	
Mg	0.158			0.143	0.099	0.295
Ca	6.062	5.086	3.966	3.148	3.637	0.901
Na	1.792	0.755	1.905	1.961	0.120	0.345
K	0.258	0.430	0.525	3.394	1.957	0.139
	44.281	42.496	42.661	44.817	41.804	37.538
Al + Si	36.011	36.225	36.265	36.171	35.950	35.858

* total iron as FeO.

Analyses 1 to 4 and 6: E.d. analyses, Research School of Earth Sciences, Canberra.
Analysis 5: E.d. analysis, Institute of Mineralogy, Copenhagen.

1. Calcium-rich zeolite, which fills vesicles in olivine and plagioclase porphyritic basalt.
2. Calcium-rich zeolite from vesicle in picritic pillow margin in hyaloclastite breccia overlying Kûgánguaq Member.
3. Core of bladed zeolite filling vesicle in olivine microporphyritic basalt tuff.
4. Prismatic radiating zeolite (phillipsite) surrounding (3).
5. Calcic-potassic zeolite filling vesicle in magnesian andesite tuff.
6. Fine granulate radiating 'zeolite' mass found intermediate between smectite at margin and silica at the core of a vesicle in feldspar-phyric silicic basalt.

are very high in silica (Table 12, no. 6) and although they fulfil the stoichiometric requirements for zeolites, they may be poorly crystallized masses or consist of several minerals.

Sheet silicates

Only one occurrence of high-temperature sheet silicate has been found in the investigated rocks. It consists of weakly pleochroic, nearly colourless, flakes of mica in the vugs of the basaltic hornfels tuff, occurring together with tridymite, orthopyroxene, plagioclase and ilmenite. The mica closely approaches phlogopite in composition (mg = 88.5) (Table 13, no. 1). It differs, however, from the ideal formula

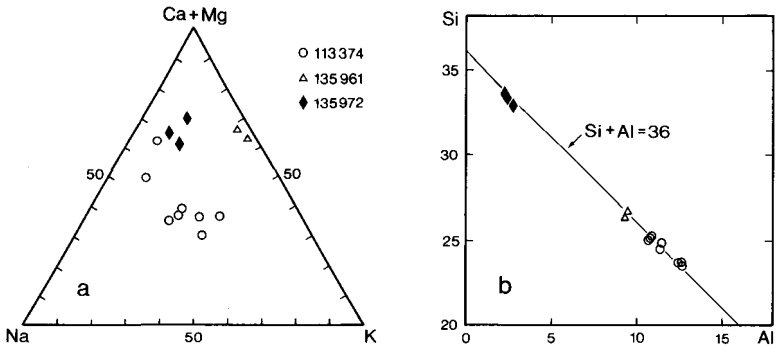

Fig. 35. Composition of zeolites in the Kûgánguaq Member rocks. a: (Ca + Mg)-Na-K cation ratio diagram. b: Si *v.* Al. The compositions fall on the line Si + Al = 36 (cations based on 72 oxygens) and thereby demonstrate their zeolite stoichiometry.

based on 22 oxygens by a lower content of Ca+Na+K (1.60 – 1.80 compared to the ideal 2.00) and by lower Al^{IV} (1.69 – 1.72 compared to the ideal Al^{IV} = 2.00).

All other analysed sheet silicates are yellowish, olive-green, green and brownish minerals which form rosettes of flakes and very fine-grained to cryptocrystalline aggregates. These phases have only been investigated by energy dispersive probe analyses, which allow comparatively non-destructive determination. All the phases in question have compositions similar to smectites; neither chlorites, nor potassic phases like celadonite, have been identified.

The smectites are roughly of two types.

(a) an alumina-poor type (Table 13, nos 3, 6 and 7) which compositionally falls in the range of saponites, such as recently described in detail from deep sea pillows (e.g. Böhlke *et al.*, 1980). This first type replaces olivine, but also occurs as vesicle filling material. When calculated on the basis of 22 oxygens, the analyses mostly show a minor content of Al^{VI} if total iron is assumed to be Fe^{2+}, whereas total iron calculated as Fe^{3+} requires that tetrahedral positions be filled by other cations. The present data do not allow any reliable estimation of the Fe^{3+}/Fe^{2+} ratio, but most published smectite analyses show this ratio to be high (e.g. Weaver & Pollard, 1973). The *mg* ratios for this type vary between 81 and 57.

(b) The other smectite-type is distinctly richer in alumina (Table 13, nos 4 and 5) and has been identified as interstitial masses derived from the decomposition of residuum, and as vesicle fillings in the feldspar-phyric silicic basalt and in magnesian andesite. This type contains Al^{VI} and is characterized by *mg* varying from 55 to 45. K_2O does not exceed 1 wt.% in any of the smectites.

In summary, the Kûgánguaq Member contains an assemblage of relatively silica-rich zeolites and smectite which can be assigned to zeolite facies metamorphism, whereas minerals typical of the lower greenschist facies appear to be entirely ab-

Table 13. Sheet silicates from Kûgánguaq Member rocks

Analysis	1	2	3	4	5	6	7
GGU No.	113380	113380	135956	135972	135961	138229	135962
SiO_2	43.4	44.6	48.2	52.2	48.7	49.2	53.9
TiO_2	2.21	2.70	0.28	0.21	0.47	0.09	
Al_2O_3	10.0	10.4	5.12	12.6	11.3	4.73	1.54
Cr_2O_3	0.22	n.d.	n.d.	n.d.		0.18	
FeO*	5.20	5.21	13.6	8.34	15.7	13.7	13.1
MnO	0.02	n.d.	0.14	n.d.	0.39	0.16	
MgO	22.4	23.3	15.4	4.38	9.85	18.9	20.7
CaO	0.11	0.14	1.27	0.94	3.82	1.57	0.89
Na_2O	0.17	<0.2	<0.2	0.30	0.80	<0.2	0.22
K_2O	8.27	9.07	0.55	0.59	0.22	0.30	0.34
	92.00	95.42	84.56	79.56	91.25	88.83	90.69
mg	88.5	88.8	69.2	51.0	55.4	73.2	75.8
Cations based on 22 oxygens							
Si	6.307	6.263	7.263	7.941	6.875	7.086	7.527
Al^{IV}	1.693	1.722	0.737	0.059	1.125	0.803	0.254
Al^{VI}	0.020		0.172	2.201	0.756		
Ti	0.242	0.285	0.032	0.024	0.050	0.010	
Cr	0.025					0.020	
Fe^{3+}			1.542	0.955	1.668	1.485	1.377
Fe^{2+}	0.632	0.612					
Mn	0.002		0.018		0.047	0.020	
Mg	4.852	4.876	3.458	0.993	2.072	4.057	4.308
Ca	0.017	0.021	0.205	0.153	0.578	0.242	0.133
Na	0.048			0.088	0.219		0.060
K	1.533	1.625	0.106	0.115	0.040	0.055	0.061
	15.371	15.404	13.533	12.529	13.430	13.778	13.720

*Total iron as FeO, $mg = 100 \times Mg/(Mg + Fe^{total\ iron})$; all iron calculated as Fe^{3+} in the smectites.

Analyses 1: W.d. analysis at Grant Institute of Geology, Edinburgh.
Analyses 2, 3 and 5 to 7: E.d. analyses, Institute of Mineralogy, Copenhagen.
Analysis 4: E.d. analysis, Research School of Earth Sciences, Canberra.

1. Late phlogopite from vug in basaltic hornfels tuff.
2. As (1), from another vug.
3. Green smectite filling small vesicle in olivine miroporphyritic basalt lava.
4. Interstitial olive green smectite in feldspar-phyric silicic basalt lava.
5. Vesicle filled with light green smectite in magnesian andesite tuff.
6. Smectite pseudomorphing olivine phenocryst in basaltic feeder dyke.
7. Smectite pseudomorphing olivine phenocryst in magnesian andesite lava.

sent. Comparison with the metamorphic zonation found in drill cores in the presently active high-temperature geothermal fields of Iceland, as reviewed by Pálmason *et al.* (1979), indicates metamorphism in the lower part of the zeolite facies at temperatures well below 120°C. The preservation of magnesian olivines in unwelded tuffs, and of basaltic glass, are additional indications of the low degree of metamorphism and weathering.

Carbonates

No systematic investigation has been carried out on the carbonates, which occur as late vug fillings, but large compositional variations are known to be present. In the basaltic feeder dyke the vug centres are characterized by compositions around $Mg_{70-75}Fe_{25-27}Ca_2Mn_2$ and in the basaltic tuffs from the central crater area the carbonate is calcite $Ca_{96}Mg_3Fe_{0.5}Mn_1$.

Sulphides

Sulphides occur in very minor amounts as (a) immiscible blebs enclosed in silicate phenocrysts in the basaltic glassy tuff and probably in the early orthopyroxene phenocrysts in the andesites and as (b) various groundmass grains of Cu-Ni sulphides and pyrite formed through low temperature equilibration.

No trace of metallic iron has been found in the primary sulphide grains. The sulphide blebs consist predominantly of pyrrhotite with traces of other sulphides. Oxides have not been observed within the blebs.

CHEMISTRY

This section describes the chemistry of rocks, glasses and late-stage 'melts' from the Kûgánguaq Member and compares these with analyses of rocks and some selected glasses which are regarded as potential parents for the Kûgánguaq Member rocks, viz. picrites and olivine-poor tholeiitic basalts from the Vaigat Formation on Disko.

To save space in the description and discussions the following rock types from the Vaigat Formation will be cited with Roman numerals in the text and figures.

Type I_A: Picrites from the Naujánguit Member.
Type I_B: Picrites from the Ordlingassoq Member.
Type II: Olivine-poor tholeiitic basalts from the Naujánguit and the Qordlortorssuaq Members.
Type III: Olivine microporphyritic basalts from the Kûgánguaq Member.
Type IV: Magnesian andesites from the Kûgánguaq Member.
Type V: Feldspar-phyric silicic basalts from the Kûgánguaq Member.

Chemical alteration

As described in the section on mineralogy, the Kûgánguaq Member rocks have been extensively affected by reaction with circulating water to form smectite and zeolites instead of olivine and acid residuum. Most altered are the vesiculated top zones of lava flows which have therefore been avoided in the sampling. On the other hand, the presence of well-preserved glass shows that this reaction was far from penetrative, and many samples appear to be only slightly altered.

The most notable effect of alteration is that the unwelded subaerial tuffs, such as samples 135954 and 138348 (Table 20) have lost Na_2O, and the low totals indicate that they have also taken up 2 to 5% H_2O. Most likely, some samples may have gained or lost other alkalies which may help to explain the somewhat irregular K and Rb distributions within the individual rock types. However, since an irregular K and Rb pattern is also observed within the very fresh sample population, it must partly be a pristine igneous feature. No significant chemical changes appear to accompany the formation of high temperature metamorphosed (welded) basaltic tuffs.However, some of the lower Naujánguit Member picrites have experienced extensive hydrothermal metamorphism and alteration, having taken up 5 to 10% of H_2O and CO_2, partly due to their proximity to the Kûgánguaq hinge zone.

In the following the Kûgánguaq Member rocks are treated as unaltered igneous rocks, but it should be noted that Na_2O loss has affected the norms of several of the analysed glass samples.

Table 14. Chemical analyses of picrites from the Vaigat Formation on Disko

	Naujánguit Member				Ordlingassoq Member		
Analysis	1	2	3	4	5	6	7
GGU No.	156717	113210	156706	264137	156737	136943	138228
SiO_2	44.31	45.14	45.89	45.67	44.67	45.08	44.29
TiO_2	0.76	0.92	1.20	1.15	1.30	1.17	1.23
Al_2O_3	10.06	10.70	12.51	10.56	10.38	11.23	10.72
Cr_2O_3	0.25	0.25	0.16		0.17	0.18	0.18
Fe_2O_3	1.73	3.50	4.23	2.66	3.37	3.63	4.67
FeO	8.64	7.34	7.04	8.98	8.08	7.62	7.27
MnO	0.21	0.19	0.22	0.17	0.22	0.17	0.18
MgO	21.15	20.48	15.20	20.05	18.81	18.48	16.78
CaO	8.60	8.70	10.08	8.67	9.85	9.59	10.40
Na_2O	1.12	1.24	1.47	1.38	1.45	1.30	1.43
K_2O	0.02	0.08	0.05	0.12	0.07	0.18	0.08
P_2O_5	0.06	0.07	0.09	0.12	0.11	0.09	0.11
H_2O^+						1.44	1.18
H_2O^-							1.11
loi	3.36	1.92	1.94	0.84	1.47		
	100.27	100.53	100.08	100.37	99.95	100.16	99.63
FeO*	10.20	10.49	10.85	11.37	11.11	10.89	11.47
mg	80.7	79.8	73.9	78.1	77.4	77.4	74.7

Major elements: XRF analyses, GGU's chemical laboratories, (Sørensen 1975) nos. 1 to 6. G. Hornung, Leeds University, no. 7.
FeO* = total iron as FeO.
mg = 100 × Mg/(Mg + Fe^{2+}), for Fe_2O_3/FeO = 0.15.
loi: loss on ignition (total volatiles).

1. Picritic pillow. In gully just west of Naujánguit at altitude 420 m (70°15′28″N, 53°50′00″W).
2. Picritic lava. 1 m above the base of 20 m thick flow. In the west side of the valley at Manîtdlat kugssinerssuat at altitude 420 m (70°13′13″N, 53°33′06″W).
3. Picritic lava. 15. cm above the base of 4 m thick picritic lava rich in vesicular veins. Gully in the west side of Kûgánguaq 2.5 km south of the entrance at altitude 565 m (70°16′05″N, 54°00′24″W).
4. Picritic pillow margin. In the east side of Kûgánguaq west of point 1310 m at altitude 795 m (70°04′28″N, 53°31′12″W).
5. Picritic pillow. In steep wall 1 km north of Kitdlarpât kûgssua at altitude 900 m (70°05′42″N, 53°06′13″W).
6. Picritic pillow. 1 km NW of point 860 below Ordlingassoq at altitude 820 m (70°11′45″N, 53°24′12″W).
7. Pillow fragment in pillow breccia just overlying Kûgánguaq Member at Kugssinikavsak at altitude 790 m (70°13′59″N, 53°41′09″W).

Table 15. Chemical analyses of olivine-poor tholeiitic basalts from the Vaigat Formation

	Lavas from Naujánguit Member		Lavas from Qordlortorssuaq Member				
Analysis	1	2	3	4	5	6	7
GGU No.	113236	113325	113327	113328	113245	113330	113362
SiO_2	46.80	47.74	47.40	47.23	47.60	47.50	48.24
TiO_2	1.54	1.56	1.48	1.47	1.98	2.29	2.28
Al_2O_3	14.20	14.05	14.50	14.48	14.40	13.90	13.87
Fe_2O_3	5.50	3.34	4.00	4.71	5.30	4.50	6.05
FeO	5.80	7.95	7.10	6.50	5.60	8.30	6.84
MnO	0.18	0.21	0.18	0.19	0.21	0.20	0.22
MgO	10.20	9.89	9.02	9.17	8.00	7.41	7.42
CaO	12.00	12.02	12.20	12.06	12.40	12.10	11.77
Na_2O	1.77	1.89	1.88	1.85	2.10	2.31	2.19
K_2O	0.09	0.11	0.14	0.07	0.27	0.21	0.10
P_2O_5	0.16	0.16	0.19	0.17	0.25	0.24	0.16
H_2O^+	1.75	1.30	1.68	1.99	1.86	0.55	1.20
CO_2			0.01				
	99.99	100.22	99.78	99.89	99.97	99.51	100.34
FeO*	10.75	10.96	10.70	10.74	10.37	12.35	12.29
mg	65.7	64.6	63.0	63.3	60.9	54.8	55.0
Trace elements, in ppm							
Sc	46	46	47	46	47	44	47
V	361	365	364	347	385	451	448
Cr	611	420	400	370	420	219	252
Co	57	52	51	54	47	50	49
Ni	237	174	147	163	140	92	90
Cu	175	178	167	162	144	220	208
Zn	80	84	84	83	84	97	94
Ga	16		17	16	18	21	18
Rb	0.5	1.5	2	0.5	2	1.5	1
Sr	158	175	135	165	235	243	210
Y	26	27	28	28	29	33	33
Zr	80	75	72	73	111	125	114
Nb	3	2	3	2	10	8	6
Ba	33	31	38	26	113	64	54
Ce		12	12	12			20
Nd		9	10	10			18

Major element chemistry: XRF analyses, GGU's chemical laboratories, (Sørensen 1975) nos. 2, 4, and 7. G. Hornung, Leeds University, nos. 1, 3, 5, and 6.
Trace elements: XRF analyses at Institute of Petrology, Copenhagen University.
FeO*, total iron as FeO.
mg = 100 × Mg/(Mg + Fe^{2+}), for Fe_2O_3/FeO = 0.15 (see compilation by Brooks 1976).

1. Olivine porphyritic basalt from 60 m below the base of the Kûgánguaq Member at the west side of Manîtdlat kugssinerssuat valley at altitude 590 m (70°12′41″N, 53°33′21″W) at the site of section 7, Fig. 5.
2. Olivine and plagioclase porphyritic basalt from 60 m below the base of the Kûgánguaq Member. Sample from 2 m above the base of a 30 m thick lava. Steep gully between points 1440, 1869 and 1730 in the north-east side of the Kûgánguaq valley at altitude 450 m (70°06′42″N, 53°43′15″W) at the site of section 8, Fig. 5.

Major elements and normative mineralogy

Analyses of some selected uncontaminated type I_A and I_B samples are presented in Table 14, type II rocks are given in Table 15 and some uncontaminated basalt glass analyses are presented in Table 16. The type I samples (picrites) are strongly olivine normative and slightly hypersthene normative basalts (Table 21), which chemically cluster along an olivine control line (fig. 37; Clarke, 1970; Clarke & Pedersen, 1976) and which are poor in incompatible minor and trace elements.

The type I_A rocks from the Naujánguit Member show a considerable range in MgO from more than 25% to less than 15 wt.%; but a compositional clustering around MgO = 22 to 23 wt.% (fig. 36, Table 14, no. 1) strongly indicates that such magmas are the dominant picrite type to enter high crustal levels in the early stages of volcanism. The type II rocks from the Naujánguit and Qordlortorssuaq Members, which contain between 11 and 7% MgO, are hypersthene and olivine normative, and their similarity to the glass from picritic pillow margins (see Tables 15 and 16) strongly indicates that they are derived from picrites by olivine fractionation.

The type I_B rocks also cover a wide range of MgO values (fig. 36), but cluster at distinctly lower MgO (between 15 and 20 wt.%) than I_A. The most common I_B rocks are very similar to Clarke's (1970) estimated parental picrite magma from Svartenhuk.

The type III rocks from the Kûgánguaq Member (Tables 17 and 19) show only a limited range in major elements with MgO ranging between 13 and 10 wt.%. They are strongly hypersthene-normative basalts (Table 21) which range from slightly olivine- to distinctly quartz-normative compositions.

The type IV rocks from the Kûgánguaq Member (Tables 18 and 19) are magnesian andesites with MgO values between 9.5 and 7.8 wt.%, and are strongly hypersthene normative (Table 21) and clearly quartz normative.

The type V rocks from the Kûgánguaq Member (Table 18) are distinctly quartz normative (Table 21) and low in MgO (6 to 6.5 wt.%), but in other respects show features intermediate between type II and III rocks.

Table 15 cont.

3. Phenocryst-poor basalt from the lowermost lava in the Qordlortorssuaq Member at altitude 522 m. Same locality as no. 2, Fig. 5 section 8.
4. Phenocryst-poor basalt from the second lava in the Qordlortorssuaq Member at altitude 532 m. Same locality as no. 2, Fig. 5, section 8.
5. Phenocryst-poor basalt from the only lava representing the Qordlortossuaq Member, at altitude 700 m. Same locality as 1.
6. Feldspar-phyric basalt from the uppermost lava in the Qordlortorssuaq Member, just below picritic pillow breccia at altitude 547 m. Same locality as 2, 3, and 4. Fig. 5 section 8.
7. Feldspar-phyric basalt from the only lava from Qordlortorssuaq found on the central tuff shield of the Kûgánguaq Member at altitude 870 m. About 1 km north of Harald Moltke Dal (70°13′43″N, 53°51′29″W), Fig. 5 section 2b.

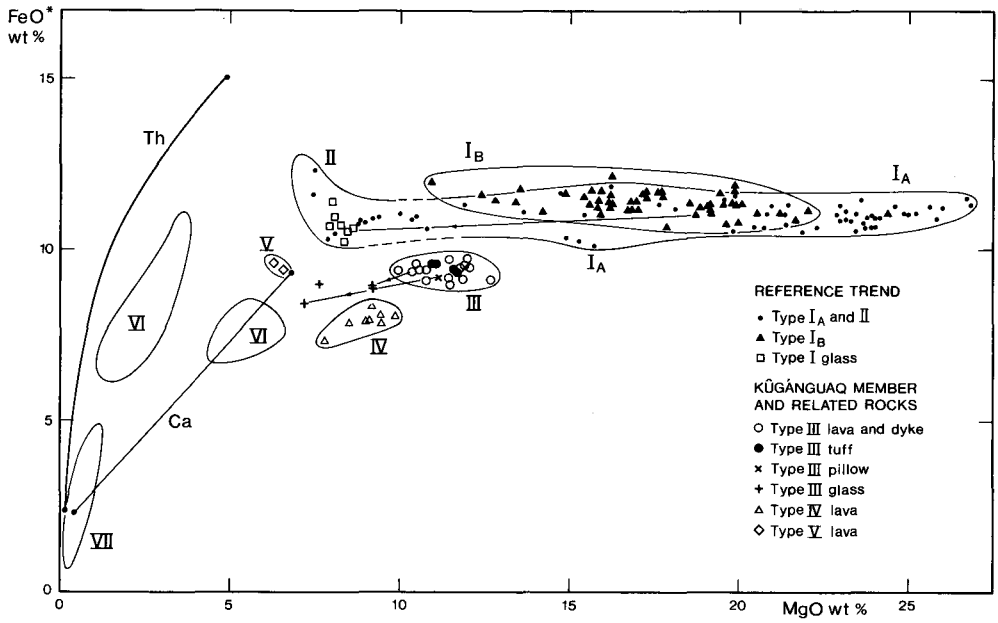

Fig. 36. FeO* (total iron as FeO) *v.* MgO diagram. Line with arrow connects bulk rock and glass from the same sample. The fields marked with Roman numerals are as given in the text. I: Picrites (A from Naujánguit Member and B from Ordlingassoq Member). II: Naujánguit and Qordlortorssuaq Member olivine-poor tholeiitic basalts. III: Kûgánguaq Member olivine microporphyritic basalts. IV: Kûgánguaq Member magnesian andesites. V: Kûgánguaq Member feldspar-phyric silicic basalts. Also shown are fields of Maligât Formation andesites and dacites (VI) and rhyolites(VII), and average tholeiites from Thingmuli (Th) and Cascade calcalkaline rocks (Ca) (Carmichael, 1964) all from Pedersen (1981, fig. 2c).

Cation normative mineralogy

Since there is no evidence of any high-pressure mineralogy in the Kûgánguaq Member rocks, their relations are presented in ol–cpx–opx–plag–qz normative projections. The cation norm projections discussed by Irvine (1970, 1979) to illustrate major layered intrusions with abundant noritic rocks are particularly relevant to the Kûgánguaq Member rocks, which compositionally approach some norite suites. Various recalculated phase relations from the literature are described in detail in the figure texts.

The cation normative olivine (fo + fa), clinopyroxene (di + hd), orthopyroxene (en + fs), plagioclase (an + ab) and quartz (Qz) relations are shown for rocks and glasses from type I to V rocks from the Vaigat Formation in fig. 37 a to d.

Inspection of the diagrams shows that the type I rocks project along a belt which rather crudely defines an olivine control line, leading from well within the olivine volume at low pressures towards an area occupied by type II rocks. The basaltic glasses from picritic pillows project approximately at the end of cluster (I–II) and

Table 16. Basalt glass analyses from picritic pillow margins in the Vaigat Formation

Analysis	1		2		3	
GGU no.	136943	lσ(6)	264137	lσ(6)	156737	lσ(6)
in wt. %						
SiO_2	48.17	0.07	47.95	0.14	48.99	0.28
TiO_2	1.59	0.04	1.59	0.04	1.90	0.04
Al_2O_3	15.01	0.12	14.67	0.08	14.14	0.14
FeO*	10.56	0.14	10.52	0.08	10.61	0.24
MnO	0.13	0.03	0.13	0.02	0.13	0.02
MgO	8.42	0.06	8.52	0.07	7.84	0.24
CaO	13.06	0.11	12.79	0.11	12.78	0.12
Na_2O	2.01	0.07	2.07	0.04	2.05	0.07
K_2O	0.17	0.01	0.17	0.02	0.19	0.02
P_2O_5*	0.128	0.0035(5)	0.164	0.0031(6)	0.165(2)	
	99.25		98.57		98.80	
mg	61.7		62.1		59.9	
CIPW weight norm						
or	1.0		1.0		1.1	
ab	17.1		17.7		17.5	
an	31.6		30.6		29.1	
di	26.7		26.6		27.7	
hy	8.7		8.8		15.7	
ol	9.4		9.8		2.7	
mt	2.0		2.0		2.0	
il	3.0		3.1		3.7	
ap	0.30		0.38		0.39	
Cation normative ratios						
an in Plag	63.5		61.9		61.0	
$100 \times Mg/(Mg + Fe^2 + Mn)$ in silicates	67.0		67.4		66.2	
in ppm						
Cr_2O_3	410		400		350	
NiO	170		200		150	

W.d. analyses at Institute of Mineralogy, Copenhagen.
*Separate trace element analyses for P, Cr and Ni.
$Fe_2O_3/FeO = 0.15$ in norm calculations.

Numbers in parentheses indicate number of analyses.
1. Bulk rock in Table 14 no. 6.
2. Bulk rock in Table 14 no. 4.
3. Bulk rock in Table 14 no. 5.

Table 17. Chemical analyses of olivine microporphyritic basalts from the Kûgánguaq Member

	Feeder dyke		Lavas								Welded tuffs			
Analysis	1	2	3	4	5	6	7	8	9	10	11	12	13	14
GGU No.	138229	138214	138215	138216	138222	113238	113239	113240	113315	113317	113321	135975	113380	135974
wt%														
SiO_2	51.35	50.61	51.43	51.12	49.70	50.30	50.97	50.88	50.64	50.76	51.60	50.45	51.67	51.81
TiO_2	1.16	1.10	1.21	1.02	1.08	1.09	1.09	1.20	1.17	0.89	1.16	1.19	1.15	1.14
Al_2O_3	14.12	14.19	14.38	14.48	13.87	14.90	15.16	14.40	14.31	14.41	14.18	14.51	14.16	14.04
Cr_2O_3	0.18	0.18	0.19	0.19	0.17	0.20	0.18	0.18	0.19	0.24	0.20	0.19	0.19	0.19
Fe_2O_3	0.71	3.00	1.80	1.58	2.88	1.60	2.11	1.39	2.48	1.75	1.19	1.71	2.04	1.00
FeO	8.53	6.34	7.49	7.50	6.72	7.50	7.00	7.45	7.20	7.34	8.38	7.82	7.50	8.44
MnO	0.16	0.16	0.21	0.18	0.17	0.18	0.25	0.26	0.18	0.20	0.18	0.19	0.19	0.18
MgO	10.28	10.38	9.65	11.14	11.01	11.70	10.56	11.21	11.70	12.50	10.80	10.79	11.65	11.55
CaO	8.56	8.29	8.62	8.35	8.46	9.00	8.79	8.75	8.23	8.39	8.70	8.98	8.44	8.54
Na_2O	1.90	1.61	1.67	1.56	1.49	1.57	1.59	1.54	1.69	1.45	1.55	1.73	1.67	1.58
K_2O	0.37	0.28	0.39	0.36	0.16	0.22	0.17	0.22	0.72	0.46	0.53	0.32	0.68	0.66
P_2O_5	0.13	0.13	0.13	0.13	0.11	0.15	0.17	0.19	0.14	0.10	0.14	0.13	0.13	0.12
H_2O^+	1.83	1.15	2.22	1.52	2.48	1.39	1.50	1.37	1.38	1.00	1.20	1.19	1.06	0.96
H_2O^-	0.20	0.30	0.50	0.40	1.45									
CO_2		2.50												
S	0.06				0.01						0.05	0.01	0.01	0.01
Less O	–0.03										–0.02			
Excess loi								0.25						
	99.51	100.22	99.89	99.53	99.76	99.80	99.54	99.29	100.03	99.49	99.84	99.21	100.54	100.21
FeO*	9.17	9.04	9.11	8.92	9.31	8.94	8.90	8.70	9.43	8.92	9.45	9.36	9.34	9.34
mg	66.6	67.2	65.4	69.0	67.8	70.0	67.9	69.7	68.9	71.4	67.1	67.3	69.0	68.8

Table 17. cont.

	Feeder dyke		Lavas								Welded tuffs			
Analysis	1	2	3	4	5	6	7	8	9	10	11	12	13	14
GGU No.	138229	138214	138215	138216	138222	113238	113239	113240	113315	113317	113321	135975	113380	135974
Trace elements in ppm														
Sc	35	35	35	36	35	37	36	35	34	33	38	38	37	36
V	255	241	257	237	243	239	234	253	250	236	262	265	260	255
Cr	1223	1266	1284	1324	1195	1360	1226	1235	1292	1630	1261	1313	1300	1306
Co	42	41	39	41	42	41	39	41	43	47	42	46	44	49
Ni	13	23	11	40	34	43	28	21	23	45	39	41	40	39
Cu	18	14	15	16	17	17	17	14	14	17	18	19	18	19
Zn	82	79	80	81	80	79	80	81	83	82	84	88	82	79
Ga	18	17	18	17	17	17	17	17	19	17	17	18	18	18
Rb	13	7	21	14	4	6	4	8	18	11	12	3	23	23
Sr	169	168	170	148	160	149	154	159	159	161	161	160	159	157
Y	22	22	23	20	22	23	23	23	23	19	23	24	23	22
Zr	115	111	117	103	104	109	114	100	116	85	111	111	109	106
Nb	<2	5	5	<2	5	4	5	5	5	4	5	5	5	6
Ba	180	169	149	147	118	109	101	108	184	135	146	152	160	165
La	12	12	14	16	11	15	15	14	16	11	13	14	13	10
Ce	26	28									27		24	
Nd	13	16									15		16	

Major element chemistry: XRF-analyses by GGU's chemical laboratories, Sørensen (1975) nos. 7–10 and 12–14. G. Hornung, Leeds University nos. 1–6. Classical chemical analyses by M. Mouritzen, Geological Museum, Copenhagen Univ. no. 11.
FeO* = total iron as FeO.
$mg = 100 \times Mg/(Mg + Fe^{2+})$. For Kûgánguaq Member rocks FeO = FeO* in calculations.
S and trace elements: XRF analyses at Institute of Petrology, Copenhagen University.

1. 30 cm from the margin of 4 m thick feeder dyke about 300 m below the palaeosurface. Kugssinikavsak at altitude 465 m. (70°14′10″ N, 53°41′55″ W).
2. Near chill zone of 1 to 4 m thick feederdyke about 70 m below the palaeosurface. Kugssinikavsak at altitude 700 m. (70°13′59″ N, 53°41′09″ W).
3. Lava no. 1. in Kûgánguaq Member at the east side of Kugssinikavsak gully at altitude 710 m. (70°13′59″ N, 53°41′09″ W), Fig. 5, section 6.
4. Lava no. 2 in Kûgánguaq Member at altitude 715 m, same locality as no. 3.
5. Lava no. 10 in Kûgánguaq Member at altitude 770 m, same locality as no. 3.
6. Lava no. 1 in Kûgánguaq Member at the west side of Manîtdlat kugssinerssuat valley at 650 m. (70°12′41″ N, 53°33′21″ W), Fig. 5, section 7.
7. Lava no. 2 in Kûgánguaq Member at altitude 660 m, same locality as no. 6.
8. Lava no. 4 in Kûgánguaq Member at altitude 680 m, same locality as no. 6.
9. Lava no. 4. in Kûgánguaq Member at the east side of Kûgánguaq valley about 1.2 km north of Harald Moltke Dal at altitude 804 m. Below the central tuff shield. (70°13′53″ N, 53°52′11″ W), Fig. 5, section 2a.
10. Lava no. 6 in Kûgánguaq Member, just below the lower welded tuff unit, same locality as no. 9.
11. Welded glass tuff from the middle of the 3 m thick lower glassy welded tuff in the lower tuff unit. Same locality as no. 9.
12. Welded tuff from same level as no. 11, but recrystallized to basaltic hornfels tuff.
13. Welded tuff, recrystallized to basaltic hornfels. At the base of the upper welded tuff unit in the central tuff shield. Close to no. 9 (70°13′57″ N, 53°52′00″ W).
14. Welded tuff recrystallized to basaltic hornfels. Same unit and locality as no. 13.

Table 18. Chemical analyses of magnesian andesites and feldspar-phyric silicic basalts from the Kûgánguaq Member

	Magnesian andesite lavas					Feldspar-phyric silicic basalt lavas	
Analysis	1	2	3	4	5	6	7
GGU No.	113363	135927	135945	135924	135947	135971	135972
SiO_2	56.30	57.01	59.15	56.24	56.15	50.76	51.84
TiO_2	0.95	0.99	0.94	1.00	1.00	1.55	1.48
Al_2O_3	13.20	13.15	13.47	13.30	13.28	15.42	15.25
Cr_2O_3	0.12	0.12	0.11	0.12	0.13	0.08	0.08
Fe_2O_3	2.12	2.32	1.93	3.50	1.40	2.88	2.10
FeO	5.82	5.60	5.55	4.68	6.92	6.58	7.52
MnO	0.13	0.19	0.11	0.25	0.15	0.19	0.21
MgO	9.28	8.33	7.72	8.95	9.04	6.35	6.11
CaO	6.37	6.47	5.78	6.95	6.99	10.65	10.38
Na_2O	1.97	1.92	2.04	2.30	2.30	2.12	2.03
K_2O	1.69	1.67	2.03	0.72	0.81	0.37	0.21
P_2O_5	0.19	0.17	0.19	0.17	0.17	0.19	0.19
H_2O^+	0.95	0.93	0.92	1.33	1.26	1.43	1.31
H_2O^-						0.87	0.66
S		0.04	0.01				
Less O		–0.02					
excess loi		0.63					
	99.09	99.52	99.95	99.51	99.60	99.44	99.37
FeO*	7.73	7.69	7.29	7.83	8.18	9.17	9.41
mg	68.1	65.9	65.4	67.1	66.3	55.2	53.6
Trace elements, in ppm							
Sc	26	28	25	27	28	41	
V	188	190	169	191	194	287	
Cr	850	831	749	852	858	556	518
Co	42	44	36	45	45	33	32
Ni	203	395	160	208	219	10	9
Cu	69	60	39	55	52	22	22
Zn	82	82	81	81	82	86	83
Ga	17	18	19	18	18	20	20
Rb	54	60	68	68	46	5	4
Sr	189	199	190	210	215	276	273
Y	21	21	21	21	21	28	26
Zr	129	135	149	133	134	137	132
Nb	9	9	10	8	9	14	13
Ba	383	404	463	371	390	186	167
La	29	28	33	28	32	29	23
Ce	47	48	50	42	43		47
Nd	25	24	26	24	22		26

Major element chemistry: XRF analyses, GGU's chemical laboratories, (Sørensen 1975) nos. 2–5, G. Hornung, Leeds University, nos. 1 and 6–7. S and trace elements: XRF analyses at Institute of Petrology, Copenhagen University.
FeO*, total iron as FeO.
mg = 100 × Mg/(Mg + Fe^{2+}), FeO = FeO* in Kûgánguaq Member.

Table 18 cont.

1. Magnesian andesite, from lava covering the central tuff shield about 1 km N of Harald Moltke Dal at altitude 860 m.
   (70°13'43''N, 53°51'59''W) Fig. 5, section 2b.
2. Magnesian andesite, from lava no. 12 in Kûgánguaq Member at altitude 840 m in the north side, about 3 km E of the entrance to Harald Moltke Dal.
   (70°13'07''N, 53°48'30''W) Fig. 5, section 5.
3. Magnesian andesite, from lava no. 11 in Kûgánguaq Member at altitude 840 m in the north side of Harald Moltke Dal, about 1.5 km to the east of the entrance to the valley. (70°13'38''N, 53°50'00''W) Fig. 5, section 4.
4. Magnesian andesite, from lava no. 11 in Kûgánguaq Member, same locality as no. 2.
5. Magnesian andesite, from the uppermost lava in Kûgánguaq Member (lava no. 12), same locality as no. 3.
6. Feldspar-phyric silicic basalt lava. Lava no. 2 from the top of Kûgánguaq Member at same loc. as no. 1 (Fig. 5, section 2a).
7. Feldspar-phyric silicic basalt lava. The uppermost flow in Kúgánguaq Member at the same loc. as no. 1 and 6 (Fig. 5, section 2a).

Table 19. Chemical analyses of olivine microporphyritic basalts and magnesian andesites. Supplementary data

	Olivine microporphyritic basalts					Magnesian andesite	Basaltic Pillow
Analysis	1	2	3	4	5	6	7
GGU No.	135955	135956	135957	135958	135959	135962	264110
SiO_2	52.14	51.05	52.03	51.34	51.41	56.51	51.71
TiO_2	1.10	1.03	1.14	1.14	1.09	0.94	1.27
Al_2O_3	14.07	13.54	14.53	13.73	13.90	13.23	13.90
Fe_2O_3	2.90	3.86	2.34	2.76	2.25	1.16	1.58
FeO	6.61	6.02	7.24	6.82	7.36	6.90	7.65
MnO	0.15	0.15	0.16	0.16	0.19	0.13	0.15
MgO	10.21	11.73	10.29	11.62	11.88	9.76	10.97
CaO	8.46	8.42	8.61	8.62	8.52	6.74	8.81
Na_2O	1.72	1.53	1.82	1.58	1.62	2.48	1.71
K_2O	0.67	0.28	0.34	0.38	0.59	0.75	0.62
P_2O_5	0.13	0.11	0.13	0.14	0.13	0.18	0.14
H_2O^+	1.24	1.36	1.02	0.95	0.77	1.33	1.30†
CO_2	0.15	0.10	0.10	0.10	0.10	0.10	
excess loi		0.44					
	99.55	99.62	99.75	99.34	99.81	100.21	99.81
FeO*	9.22	9.49	9.34	9.30	9.38	7.94	9.07
mg	66.4	68.8	66.3	69.0	69.3	68.7	68.3

XRF analyses at GGU's chemical laboratories (Sørensen, 1975).
FeO* Total iron as FeO.
mg = $100 \times Mg/(Mg + Fe^{2+})$, $Fe_2O_3 = 0$ in norm calculations of Kûgánguaq Member rocks.
loi loss on ignition.
† loss on ignition analysis.

1 to 5. Olivine microporphyritic basalt lavas from Kûgánguaq Member north of the tuff shield, 4.6 km south of the entrance to Kûgánguaq on the east side (70°14'47''N, 53°51'03''W), locality 3 (fig. 4a and 5). Accurate positions within the lavas in the sections are shown on fig. 5 section 3.
6. Magnesian andesite lava from Kûgánguaq Member, same locality as 1 to 5.
7. Olivine microporphyritic basalt pillow with fresh glass from Ordlingassoq Member. Eastern part of Kûgánguaq (fig. 4a) at altitude 960 (70°05'27''N, 53°34'41'W).

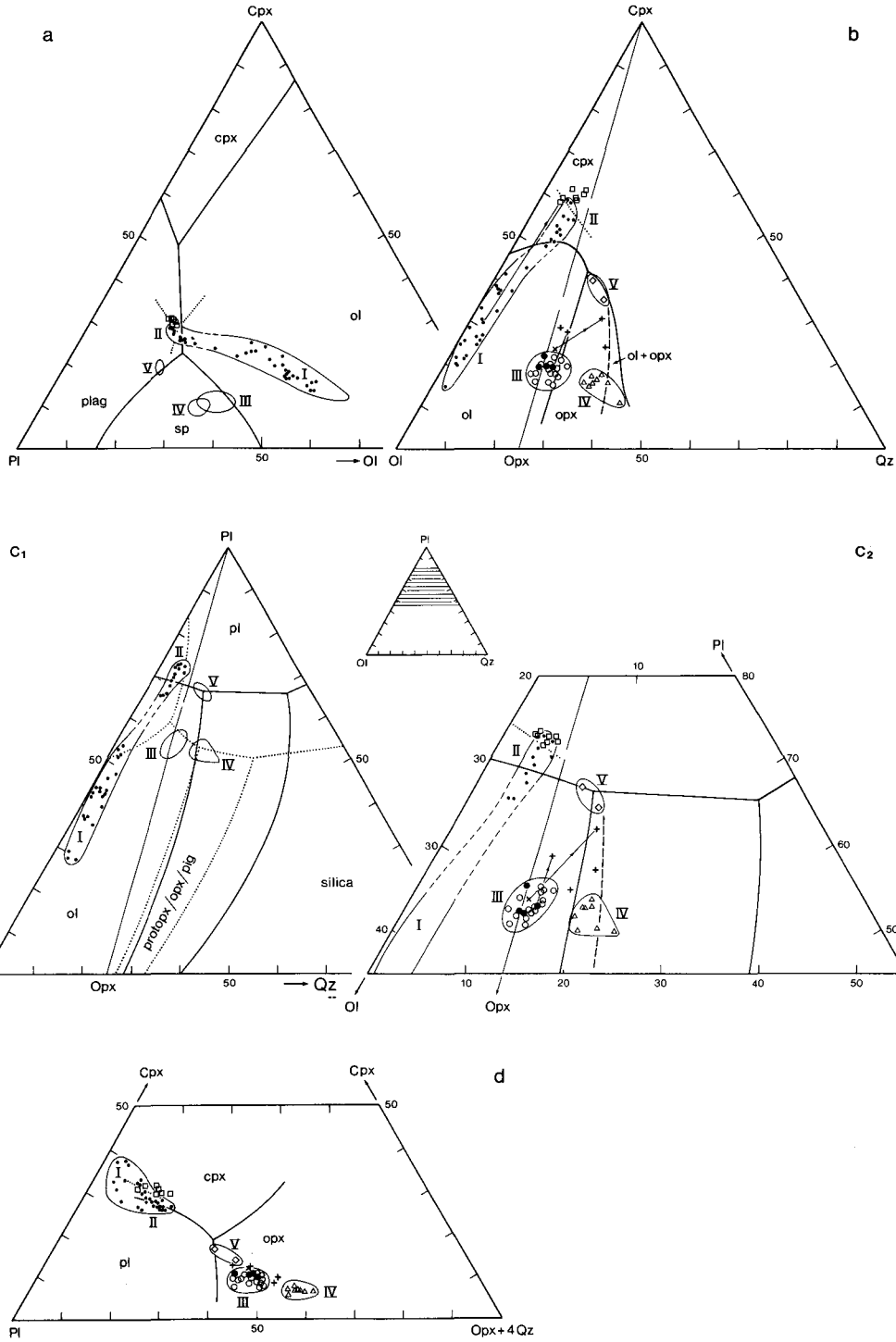
a
Cpx
cpx
ol
plag
sp
Pl
Ol
50
I
II
III
IV
V
b
Cpx
cpx
ol
opx
ol + opx
Ol
Opx
Qz
C1
Pl
pl
ol
silica
protopx / opx / plg
Ol
Opx
Qz
C2
Pl
Ol
Qz
Ol
Opx
Qz
d
Cpx
Cpx
cpx
opx
pl
Pl
Opx + 4 Qz

are still within the olivine volume of the tetrahedron. The end of cluster (II) and the glasses are close to a projected ol+cpx+plag+melt cotectic (fig. 37a) for MORB, as sketched by Irvine (1979, figs 9–12) and to experimental glasses of MORB compositions coexisting with ol+cpx+plag, as given by Walker *et al.* (1979, Table 1), which indicate that rocks of type II represent olivine fractionated picrites. This could also indicate that the picrite glasses which only carry phenocrystic olivine + chromite + minor plagioclase would be close to saturation with calcic clinopyroxene.

The type III rocks occupy a volume which extends across the silica saturation plane opx–cpx–plag with a predominance of quartz-normative rocks, and with plag+opx accounting for between 80 and 86% in the calculated norms (Table 21). The type III rocks are distinctly separated from type I and II by their more saturated nature and by their low normative cpx (figs 28, 37 a to c and Table 21). In accordance with this, phenocrystic calcic clinopyroxene is completely absent in type III rocks, which carry olivine and chromite as the early phases. The absence or scarcity of phenocrystic orthopyroxene shows that the olivine phase volume extends well into the quartz normative part of the tetrahedron for these rocks, indicative of low-pressure equilibration (e.g. Boyd *et al.*, 1964). The glasses from type III rocks (Table 20) extend further into the quartz normative volume away from olivine, in accordance with their mineralogy (figs 37 b and c_2).

←

Fig. 37 a to d. Cation normative projections in the tetrahedron olivine–clinopyroxene–plagioclase–quartz (Ol–Cpx–Pl–Qz). Signatures as in fig. 36 (except that subfields IA and IB are not shown separately). a: The plane Ol–Cpx–Pl projected from Qz. Phase fields recalculated from wt.% diagrams of the system An–Fo–Di by Andersen (1915) and Irvine (1975a). Stippled lines: phase boundaries constructed from experimental MORB glasses from Walker *et al.* (1979). Note the olivine control line defined by fields I and II. The projection shows that the fields III to V are widely separated from I + II and from the picrite glasses, but otherwise the phase relations for Kûgánguaq Member rocks cannot be interpreted in this projection. b: The plane Ol–Cpx–Qz projected from plagioclase. Dotted line: 1 atm. experimental MORB glasses coexisting with ol + cpx + pl from Walker *et al.* (1979). Full lines: Phase boundaries in Kilauean basalts (Irvine, 1979, fig. 9-7A). Note that the type III glasses are well separated from the Magnesian andesites (IV). The type III glasses do not carry phenocrystic orthopyroxene, and the primary phase boundary opx olivine for Kûgánguaq Member rocks is probably located as indicated by the dashed line in this projection. c: The plane Ol–Pl–Qz projected from Cpx. c_1: Unbroken lines: Phase boundaries as given by Morse (1980, fig. 13.12). Stippled lines: Phase boundaries as recalculated from the system Fo–An–Qz by Andersen (1915) and Irvine (1975). Field I to V as in a and b. c_2: Enlarged part of c_1. Dotted line: Phase boundaries constructed from 1 atm. experimental MORB glasses coexisting with ol + cpx + pl (Walker *et al.*, 1979). Dashed line: Possible position of the primary phase boundary ol + opx + melt in the Kûgánguaq Member rocks. Note the wide separation of the type I + II rocks and picrite glasses from the Kûgánguaq Member rocks. The type V rocks project close to the ol + opx + cpx + pl + melt reaction point as estimated by Morse (1980, fig. 13.12). d: The plane Opx–Cpx–Pl projected from Ol (Irvine, 1970). Dotted line as in (a) to (c). Unbroken line: phase boundaries estimated for Kilauean basalts by Irvine (1979, fig. 9-7B).

Table 20. Glass analyses from contaminated basalts

Rock type	Olivine microporphyritic basalt tuffs					
Analysis	1		2		3	
GGU no.	135954	$1\sigma^{(6)}$	113321	$1\sigma^{(6)}$	135975	$1\sigma^{(6)}$
in wt.%						
SiO_2	52.54	0.19	52.76	0.40	51.83	0.97
TiO_2	1.21	0.02	1.22	0.02	1.14	0.44
Al_2O_3	15.18	0.08	15.24	0.12	16.03	1.13
FeO*	8.77	0.13	8.91	0.16	8.09	0.13
MnO	0.11	0.01	0.15	0.04	0.12	0.02
MgO	9.05	0.07	9.19	0.06	9.66	1.29
CaO	9.15	0.19	9.64	0.35	9.87	0.45
Na_2O	1.31‡	0.15	1.85	0.09	1.93	0.24
K_2O	0.73	0.04	0.74	0.07	0.45	0.13
P_2O_5	0.135†	0.0034(5)	0.134†	0.0060(5)	0.13	0.07
	98.19		99.83		99.25	
mg	64.8		64.8		68.0	
CIPW weight norm						
Q	5.4		2.0		0.8	
or	4.4		4.4		2.7	
ab	11.3		15.7		16.5	
an	34.0		31.1		34.0	
di	9.2		12.9		11.8	
hy	33.0		31.3		31.8	
il	2.3		2.3		2.2	
ap	0.32		0.31		0.30	
Cations normative ratios						
an in Plag.	74.0		65.2		66.1	
$100 \times Mg/(Mg+Fe^{2+} + Mn)$ in silicates	67.4		67.3		70.6	
in ppm						
Cr_2O_3†	1240		1220		1170	
NiO†	< 20		30		< 20	

W.d. analyses at Institute of Mineralogy, Copenhagen.
†Separate trace element analyses for P, Cr and Ni.
‡Glass has suffered sodium loss due to leaching.
mg = $100 \times Mg/(Mg + Fe^{2+})$.
FeO*: Total iron as FeO. $Fe_2O_3 = 0$ in norm calculations.
Numbers in parentheses indicate number of analyses.
1 to 4: Kûgánguaq Member. 5–6 other related glasses.
1. Olivine microporphyritic basalt glass in air fall tuff, distal part of lower tuff unit in central tuff shield.

Table 20. cont.

Basalt tuff		Pillow glass rim		Basalt glass with iron in tuff	
4		5		6	
138348	1σ[6]	264110	1σ[6]	5646,Tuff	1σ[5]
51.74	0.35	53.70	0.15	53.16	0.21
1.24	0.02	1.37	0.05	1.12	0.06
14.97	0.15	15.46	0.09	14.76	0.21
8.63	0.18	8.34	0.11	11.73	0.33
0.11	0.02	0.11	0.03	0.10	0.02
7.31	0.05	7.11	0.08	6.36	0.36
9.52	0.15	9.78	0.12	8.78	0.26
1.30‡	0.12	1.93	0.02	1.97	0.11
0.62	0.03	0.77	0.05	0.69	0.03
0.144†	0.0079[4]	0.142	0.0024[5]	0.116	0.008
95.58		98.71		98.79	
60.2		60.3		49.1	
7.7		5.9		5.0	
3.8		4.6		4.1	
11.5		16.5		16.9	
34.7		31.6		29.8	
11.3		13.6		11.3	
28.2		24.7		30.5	
2.5		2.6		2.2	
0.35		0.33		0.27	
74.0		64.3		62.4	
63.1		63.7		51.1	
970		550		1510	
20		20		970	

2. Olivine microporphyritic basalt glass, glassy welded lower tuff in central tuff shield. Bulk rock Table 17 no. 11.
3. Same unit as (2) where the glass has recrystallized to hornfels tuff. Bulk rock in Table 17 no. 12.
4. Basaltic air fall tuff carrying chromite. Qordlortorssuaq.
5. Olivine microporphyritic basalt glass from margin. Bulk rock in Table 19 no. 7.
6. Basalt glass with chromite and native iron from Tuff 1, from Agatkløft, Nûgssuaq, Pedersen (1978a, p. 121) new analysis.

Table 21. Normative mineralogy of selected rocks from the Vaigat Formation

	Picrites			Olivine poor tholeiitic basalts				Olivine micropor-phyritic basalts			Magnesian andesites			Feldspar-phyric silicic basalt
				Naujánguit M.		QordlortorssuaqM.		Kûgánguaq M.			Kûgánguaq M.			
Analysis	1	2	3	4	5	6	7	8	9	10	11	12	13	14
GGUno.	156717	136943	138228	113236	113325	113327	113362	138229	113317	113321	135924	135927	135945	135972
Q								1.4		1.7	8.8	9.9	12.1	5.6
or	0.1	1.1	0.5	0.5	0.6	0.8	0.6	2.3	2.8	3.2	4.3	10.1	12.2	1.3
ab	9.8	11.2	12.5	15.3	16.2	16.3	18.8	16.6	12.5	13.3	19.9	16.6	17.5	17.6
an	23.1	24.7	23.3	31.2	29.9	31.4	28.1	29.7	32.1	30.7	24.4	22.9	21.9	32.9
di	16.4	18.4	23.5	23.2	24.0	23.8	24.7	10.6	7.9	10.0	8.0	7.2	4.8	15.6
hy	9.2	6.6	2.5	11.7	13.1	13.0	17.3	36.8	41.1	38.6	32.3	30.9	29.3	23.5
ol	37.5	33.3	32.8	12.6	10.7	9.3	3.4		1.8					
mt	2.0	2.1	2.3	2.1	2.1	2.1	2.4							
il	1.6	2.3	2.4	3.0	3.0	2.9	4.4	2.3	1.7	2.2	1.9	1.9	1.8	2.9
ap	0.1	0.2	0.3	0.4	0.4	0.4	0.4	0.3	0.2	0.3	0.4	0.4	0.4	0.5

CIPW weight norms on H_2O, CO_2 and S-free basis, recalculated to 100%.
Cr_2O_3 is not included in the norms.
In analyses 1 to 7, $Fe_2O_3/FeO = 0.15$ (see compilation by Brooks 1976).
In analyses 8 to 14, $Fe_2O_3 = 0$ in calculations.
Chemical analyses from the following tables:
1 to 3. Table 14.
4 to 7. Table 15.
8 to 10. Table 17.
11 to 14. Table 18.

The type IV rocks plot well away from these glasses and from their parents (III), being distinctly enriched in normative quartz (8 to 12%). They are unusually rich in normative orthopyroxene for andesites (29 to 34%, Table 21), and have a high hy/(hy+di) ratio (0.80 to 0.86). They carry scarce phenocrystic olivine (always resorbed and rimmed by pyroxene), traces of chromite, abundant phenocrystic orthopyroxene and scarce microphenocrystic plagioclase. The olivine-orthopyroxene phase boundary must lie near the type IV composition (fig. 37 b and c).

Finally, the type V rocks occupy a field of their own. They show similarities to evolved type II rocks, but are distinctly quartz normative and with a hy/(hy+di) ratio (0.60) between the type II (*c.* 0.25) and type III (*c.* 0.80) rocks. These basalts carry phenocrysts of olivine (pseudomorphosed), calcic clinopyroxene, orthopyroxene and plagioclase (+ traces of chromite), and could hence define a pseudoinvariant reaction point in the tetrahedron (fig. 37 b, c and d) where olivine finally reacts out (e.g. Chinner & Schairer, 1962).

Other major and minor element relations

FeO* (total iron calculated as FeO) *v.* MgO variations are shown in fig. 36. The type I_A+I_B+II rocks clearly demonstrate the olivine control line as a band parallel to the MgO-axis, with separate compositional clusters for type I_A and I_B. The type III rocks are distinctly depleted in iron relative to uncontaminated type I and II rocks with the same MgO level. Types III and IV have very similar iron-magnesium ratios, a feature also seen in the pyroxene mineralogy, whereas the type III glasses

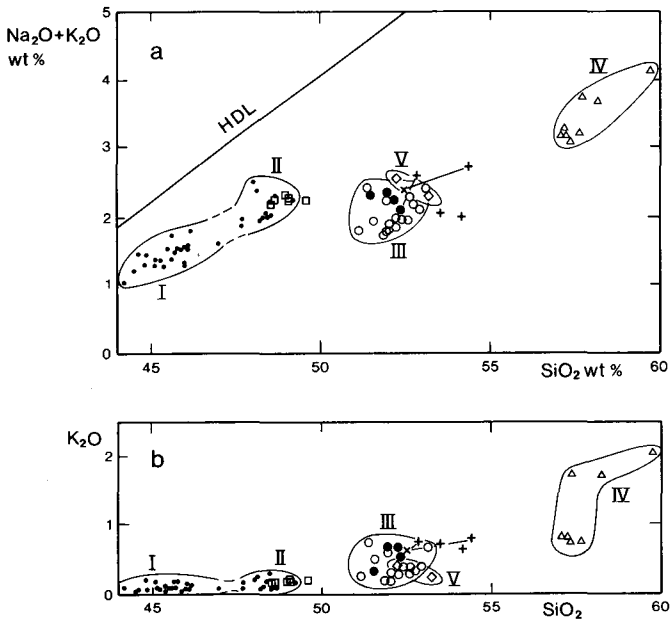

Fig. 38. a: (Na_2O + K_2O) *v.* SiO_2 diagram. Signatures as in fig. 36. HDL: Hawaiian division line (Macdonald & Katsura, 1964). All the plotted rocks are subalkaline. Two glasses (GGU 135954 and GGU 138348) have lost Na_2O through alteration. b: K_2O *v.* SiO_2 diagram, which shows the irregular K_2O enrichment found in the Kûgánguaq Member compared to type I and II samples. Two K_2O-levels are found in the magnesian andesites of which the enriched type represents the most potassic igneous rocks known from the Vaigat Formation.

are iron-enriched relative to the host rocks. The evolved nature of the type V rocks compared with types I to IV is apparent from this plot.

Alkalies. The Na_2O+K_2O *v.* SiO_2 plot (fig. 38a) shows that all the rocks plot well below the Hawaiian division line of MacDonald & Katsura (1964) and that the Kûgánguaq Member rocks are strongly subalkaline. Further, the K_2O *v.* SiO_2 diagram (fig. 38b) demonstrates that Kûgánguaq Member rocks are clearly enriched in K_2O compared to types I and II and that this enrichment is irregular. Within type III rocks, K_2O contents vary by more than a factor 3, while type IV rocks show different K_2O contents for rocks with otherwise almost identical major element chemistry.

Titanium and phosphorus. TiO_2 *v.* SiO_2 and TiO_2 *v.* MgO diagrams (fig. 39a, b) show that TiO_2 is definitely lower in Kûgánguaq Member samples than in type I to II samples at similar MgO levels, and that type III, IV and V samples fall in separate clusters. Within type III samples TiO_2 is increasing with decreasing MgO. In type IV samples TiO_2 is about constant or slightly decreasing with increasing SiO_2 and decreasing MgO, despite the absence of observed TiO_2-rich phenocryst phases. This substantiates the important conclusion that type IV rocks cannot be derived from type III magma exclusively through olivine and/or orthopyroxene fractionation.

A TiO_2 *v.* P_2O_5 diagram for rocks and glasses, for which high quality P_2O_5 analyses are available, is shown in fig. 40. The correlation between TiO_2 and P_2O_5 pro-

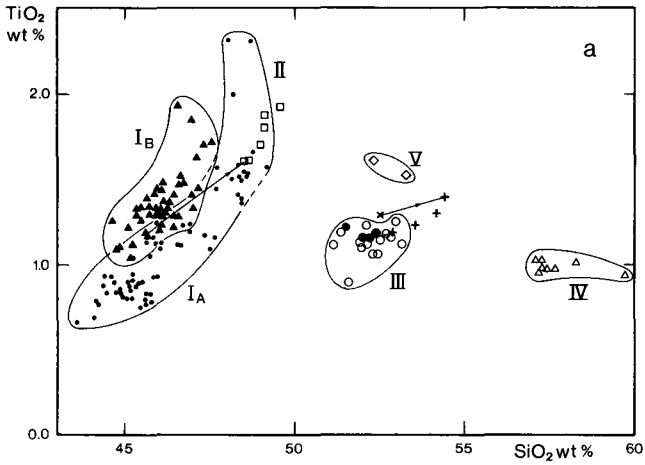

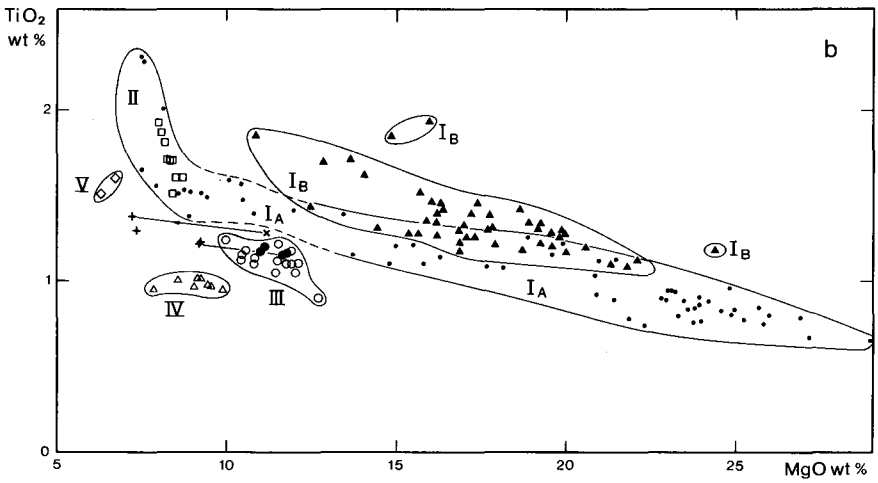

Fig. 39. TiO_2 *v.* SiO_2 (a) and MgO (b) diagrams. Note the wide separation of the Kûgánguaq Member rocks from type I_A, I_B and II and picrite glasses. The considerable TiO_2 scatter at constant SiO_2 and MgO levels must be a magmatic feature.

vides a further test as to which rock samples are related through simple crystal fractionation since both elements are moderately imcompatible in these magmas as long as no unobserved phases have participated in the process (TiO_2 enters pyroxenes and chromites while P_2O_5 enters olivine).

Type I_A, and most of the I_B rocks plot together in a narrow belt. The type I_B rocks are enriched in both TiO_2 and P_2O_5 compared to type I_A rocks at the same MgO-level. Some type I_B samples, and two of the analysed picrite glasses, plot along a separate trend towards relative P_2O_5-enrichment. Unpublished analyses of alkaline rocks from the Manîtdlat Member suggest that the type I_B rocks have probably been slightly mixed with alkaline melts.

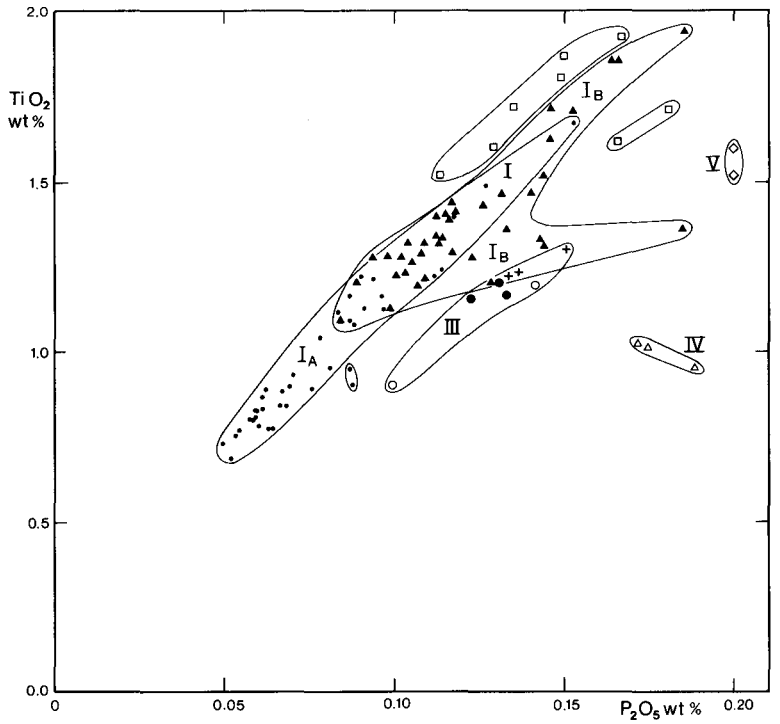

Fig. 40. TiO_2 *v.* P_2O_5 diagrams. Type I_A rocks show a close correlation and approximate the lines given by $y = 0.219 + 9.794\,x$ ($r^2 = 0.90$). Type III rocks and their glasses define a field ($r^2 = 0.89$), approximately parallel to type I_A but at slightly higher P_2O_5, whereas type IV rocks are distinctly enriched in P_2O_5 and show negative correlation with TiO_2.

The picrite glasses also define a narrow belt parallel to the picrites, but at slightly higher TiO_2-values in accordance with the higher P_2O_5/TiO_2 ratio in olivines compared to bulk rocks and melts.

Trace elements

Transition metals

As already demonstrated through trace and minor element analyses of minerals and glasses, some transition elements display highly anomalous behaviour in Kûgánguaq Member rocks, and the same is true for the rock analyses discussed in detail below.

Sc and V show essentially the same type of variation in plots *v.* SiO_2 and *v.* MgO (fig. 41a to d). The geochemistry of Sc within the type I rocks is poorly known, but the concentrations definitely increase from type I to type II rocks. The type III rocks have similar, or slightly higher Sc levels than type I, whereas the type IV

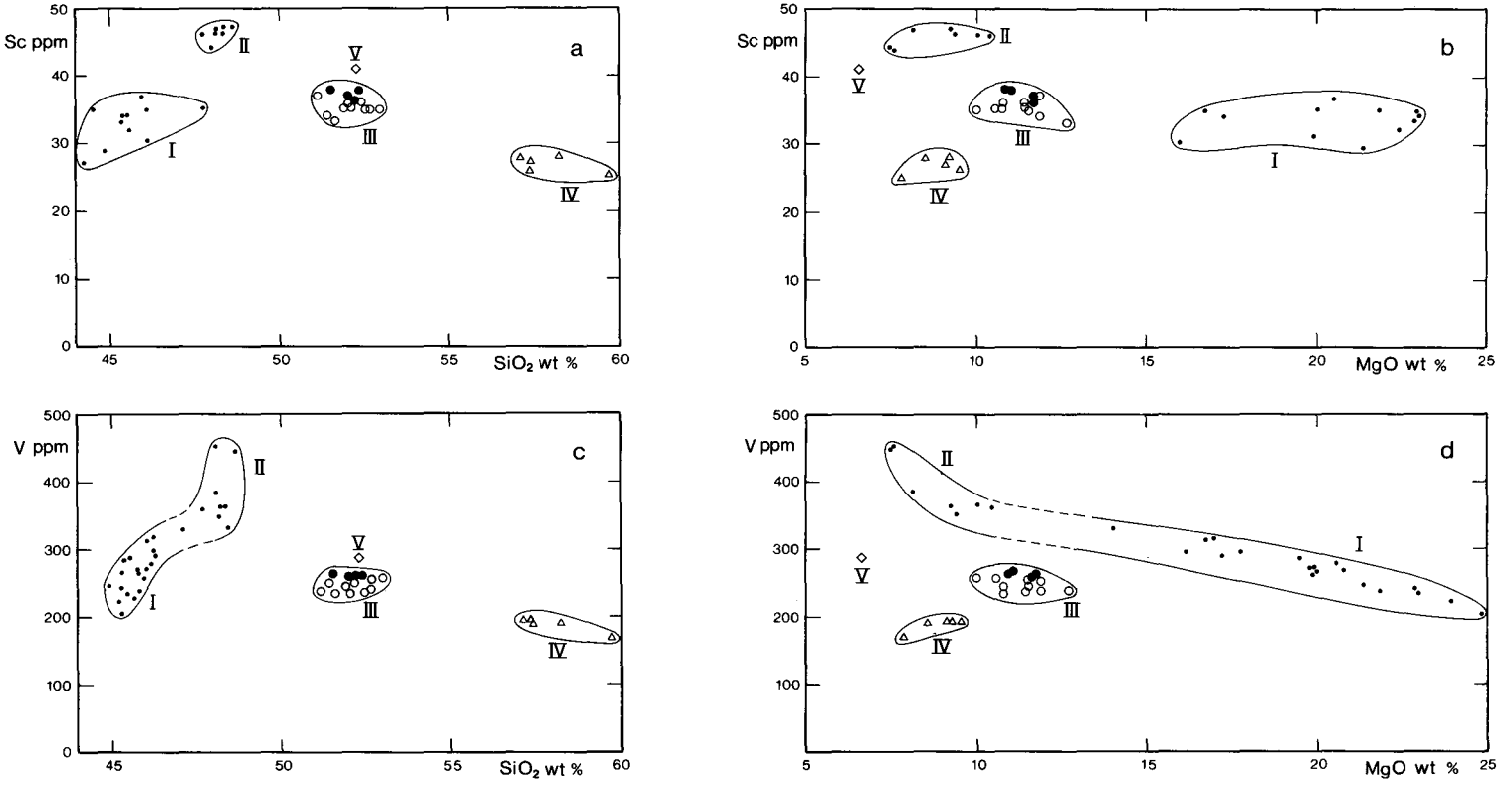

Fig. 41. a to d. Sc and V *v.* SiO_2 and MgO diagrams. Note the increasing V with decreasing MgO which shows that the combined olivine plus chromite fractionation in type I_A to II rocks did not prevent concentration of V.

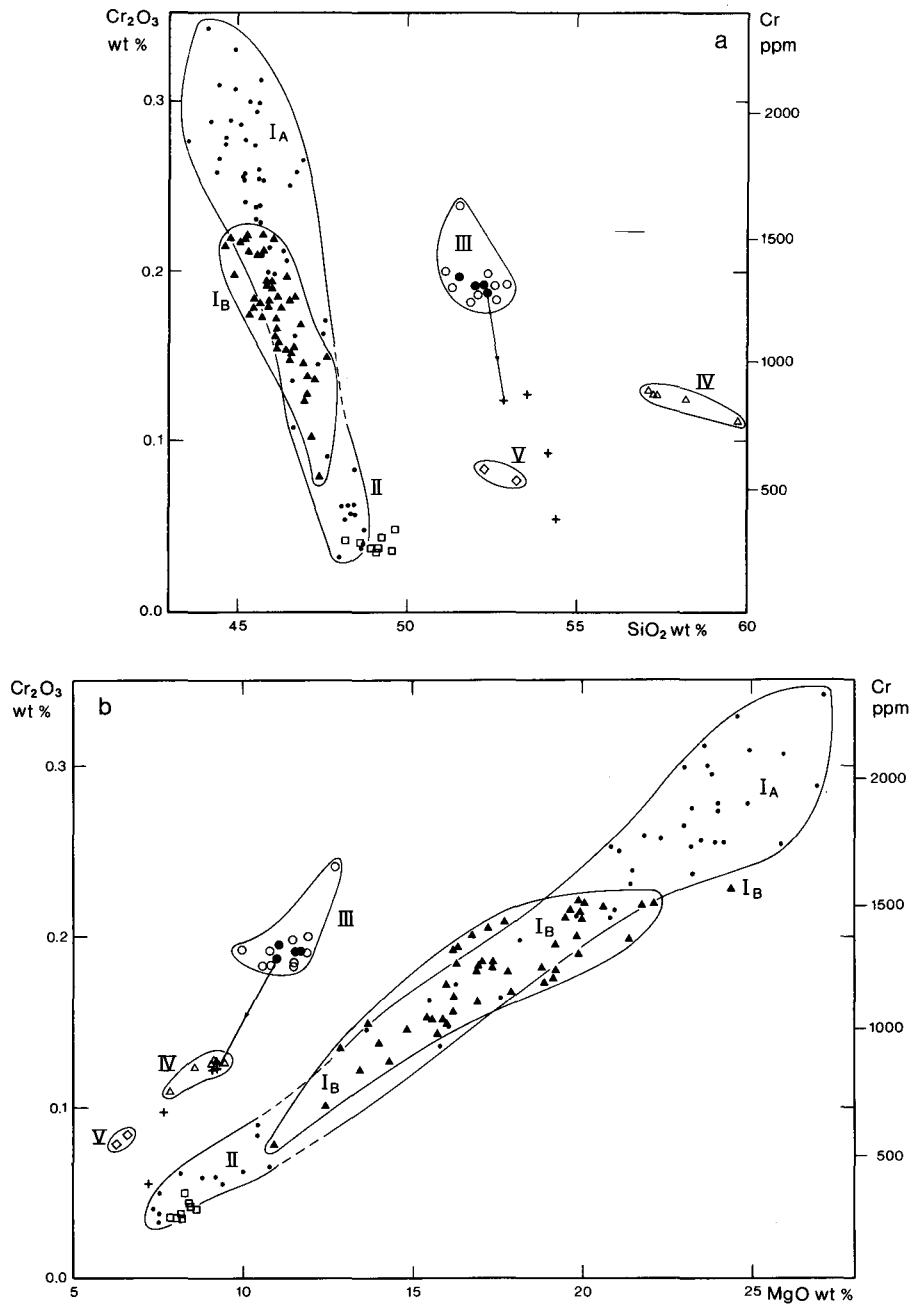

Fig. 42. a: Cr *v.* SiO_2 and b: Cr *v.* MgO diagrams. Note that Cr in the type I and II rocks and their glasses rapidly decrease with increasing SiO_2 and decreasing MgO. The Kûgánguaq Member rocks contain much higher Cr at the same MgO compared to types I and II. The very high Cr at high SiO_2 in the Kûgánguaq Member distinguishes these rocks from most other silicic basalts and andesites.

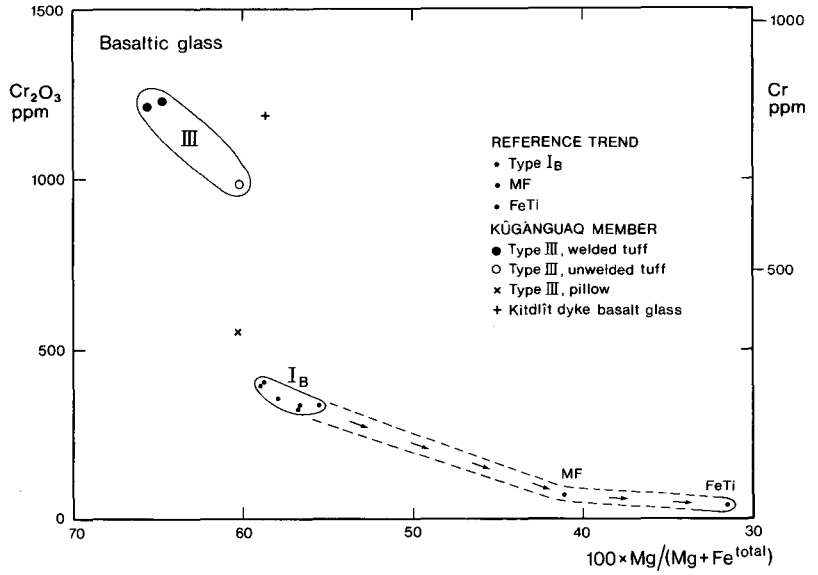

Fig. 43. Cr_2O_3 *v.* 100 × Mg/(Mg + Fe^{total}) diagram for basaltic glasses. IB: picrite glass, MF: glass in sample 176765 from the Maligât Formation, FeTi: glass chill in late FeTi basalt dyke 176554. Note that the glasses representing the regional picritic to basaltic volcanism plot in a narrow band characterized by low Cr. The pillow glass from the Ordlingassoq Member (×) with type III bulk chemistry is higher in Cr than the picrites but very distinctly lower than the other type III glasses. This is interpreted as reflecting a higher f_{O_2} in glass no. GGU 264110 at the time of quenching.

rocks have less Sc. The single determination from a type V rock is intermediate between type II and III. Sc is particularly concentrated in pyroxenes (see review by Irvine, 1978) and could provide a test for their fractionation; such a fractionation is, however, more tightly constrained by the variation of Ti and Cr.

V gradually increases from type I to type II rocks. It is moderately enriched in chromite in type I samples, but not to such an extent that chromite precipitation could counteract the effect of olivine fractionation. Compared to type I and II rocks the Kûgánguaq Member samples are all distinctly poorer in V at the same MgO levels. Type IV samples show a slight decrease in V with increasing SiO_2, as was the case for TiO_2. V has been found to be strongly concentrated in Kûgánguaq Member chromites and much less so in the orthopyroxenes, but no fractionation effects are apparent.

Cr variations have been investigated in considerable detail (fig. 42a and b).

The type I_A and I_B samples show prominent olivine control lines with overlapping trends in the Cr_2O_3 *v.* SiO_2 and MgO diagrams and with compositional clusters for I_A at MgO = 23%, Cr_2O_3 = 0.26% and for I_B at MgO = 19 to 16% and Cr_2O_3 = 0.22 to 0.16%.

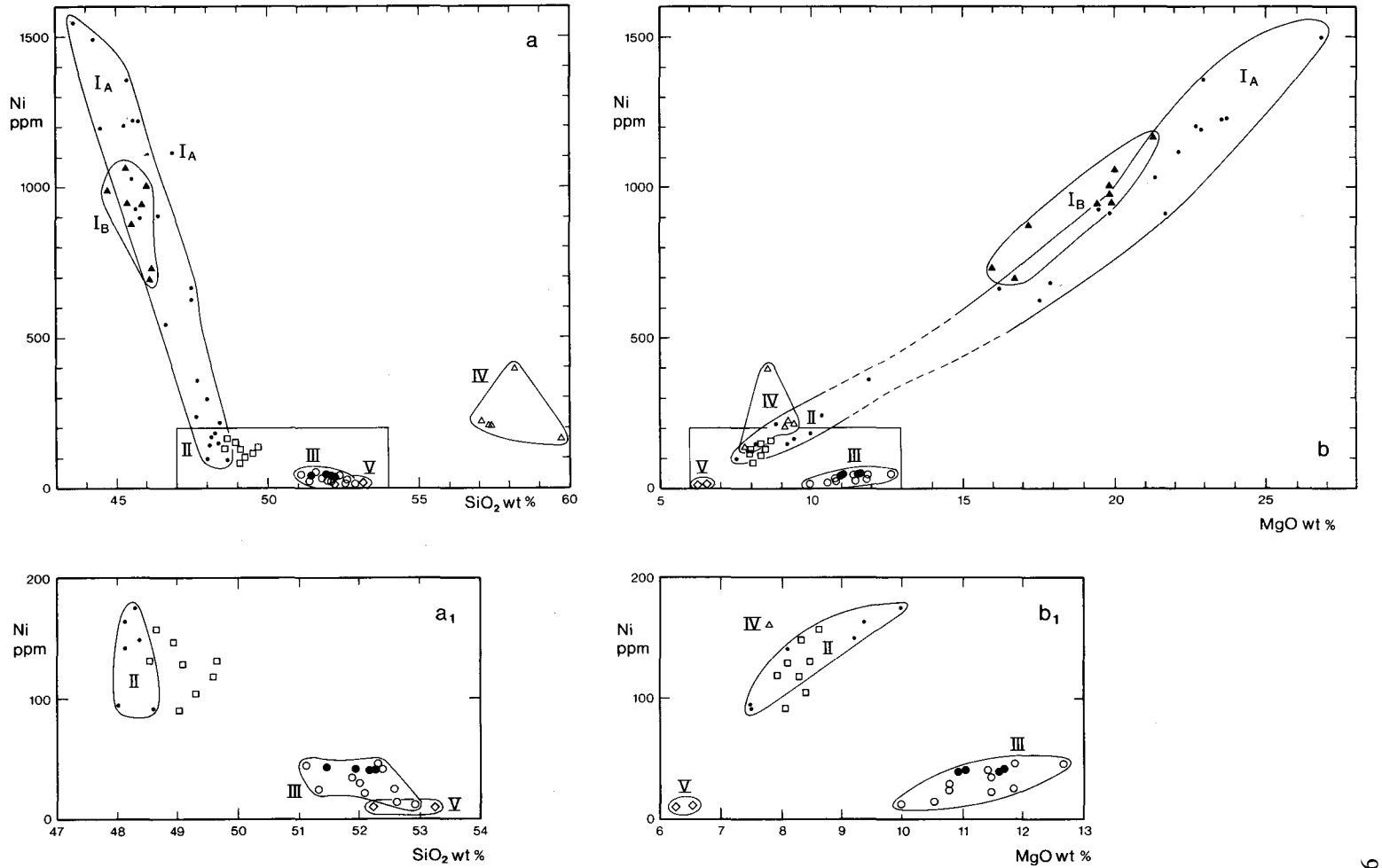

Fig. 44. a and enlargement a_1: Ni *v.* SiO_2 diagram. Type I and II rocks define the olivine control line with picrite glasses plotting close to type II. The extremely low but variable Ni in type III is attributed to sulphide fractionation. The high Ni in the magnesian andesites (IV) is extremely unusual for such silicic rocks and indicates that type IV is not a direct daughter of type III rocks. b and enlargement b_1: Ni *v.* MgO diagram. Note how markedly type III rocks deviate from the olivine control line. The type V basalts, on the other hand, plot at the lower extension of the line.

Type II samples and the glasses from picrites overlap at the lower end of the olivine control line with typical concentrations around MgO = 8% and Cr_2O_3 = 0.035%. The Kûgánguaq Member rocks show distinctly higher Cr values at comparable MgO levels than the uncontaminated type I and II rocks. Of particular petrogenetic interest is the high Cr_2O_3 (0.18 to 0.24%) in the type III samples. Since neither chromite nor olivine fractionation can lead to notable increase of Cr in the magma, and since no high-Cr source is likely among the contaminants, it can be estimated directly from fig. 42b that the main part of type III basalts was derived from a picrite magma with at least 18% MgO. Type III sample 113317 (with Cr_2O_3 = 0.24%) must have been derived from a picrite with between 21 and 23% MgO, which corresponds to the most common type I_A magma. The same line of evidence implies a minimum of 13 to 15% MgO for the parental magma of the type IV rocks. A parental magma with at least 11 to 13% MgO can be deduced for the evolved type V rocks with about 6% MgO. The very high Cr contents found in some of the type III glasses as compared to picrite glass (fig. 43) are noteworthy, the Cr_2O_3 *v.* SiO_2 diagram (fig. 42a) illustrating unusually high Cr levels for such silicic basalts and andesites.

Ni shows a rapid decrease with falling MgO (fig. 44b) and with increasing SiO_2 (fig. 44a) along the olivine control line in type I and II rocks, and the picrite glasses plot together with type II samples at the low-MgO end of the line. The Kûgánguaq Member rocks display most unusual features. The main type III rocks are extremely low in Ni for basalts when compared to type I and II samples at similar MgO levels. The same feature has been described from the iron-bearing basaltic glasses at Luciefjeld, south Disko (Pedersen, 1979b) where it was ascribed to the effects of metal and sulphide fractionation. The type V samples are even lower in Ni, and much lower than the picrite glasses. On the other hand, the type IV samples are much higher in Ni than type III samples and show considerable variation within the group. They overlap with the most magnesian type II samples, and one of the type IV samples (135927) has a high Ni (395 ppm) as picrites with about 13 wt.% MgO. This contrasting behaviour between type III and IV samples was also displayed by the Ni variations in olivine from these rocks (fig. 20b and c).

The type II basalts are characterized by 150 to 220 ppm Cu, and unpublished emission spectrographic analyses by H. Bollingberg indicate type I sample values of around 70 to 150 ppm. Cu, like Ni, is very much lower (14 to 25 ppm) in the Kûgánguaq Member types III and V samples, whereas Cu is definitely higher (39 to 69 ppm) in type IV samples (fig. 45a and b).

The similar type of variation shown by Ni and Cu implies that the basaltic rocks from the Kûgánguaq Member, represented by the type III and V samples, were affected by sulphide fractionation. On the other hand, the more silicic rocks (type IV) show much less marked depletion in these elements (fig. 45a, b), presumably because sulphide fractionation became ineffective in the more viscous andesite magma (Pedersen, 1975).

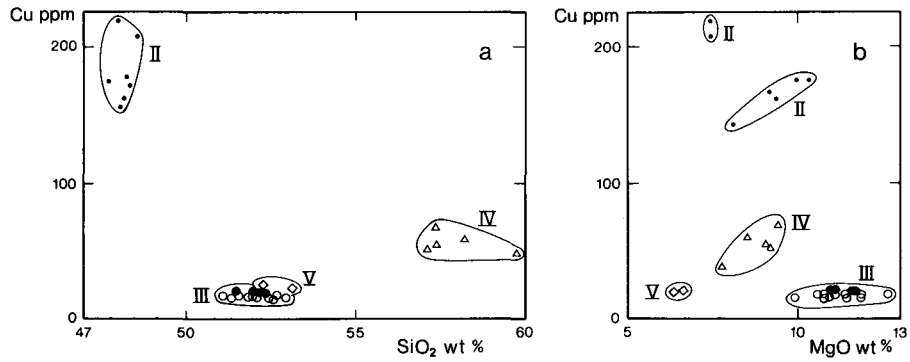

Fig. 45. a and b: Cu *v.* SiO_2 and MgO diagrams. Cu is high in type II basalts, but extremely low in type III and V rocks, presumably because of sulphide fractionation. In the andesites (IV) Cu is distinctly higher, probably because higher viscosity prevented effective sulphide fractionation.

Co shows the same type of variation as Ni and Cu, but the relative variation is smaller.

Zn only varies from 79 to 86 ppm in the analysed Kûgánguaq Member samples and thus appears to have been insensitive to both redox variations and to extraction by a hypothetical sulphide melt. This constant value around 80 ppm is not markedly different from the values found in the uncontaminated type I (62 to 101 ppm) and type II samples (80–97 ppm).

Other siderophile elements (Ga, Ge)

Ga shows only minor variation within Kûgánguaq Member rocks from 17 to 19 ppm in type III and IV samples, and *c.* 20 ppm in type V samples. No data are available from the type I picrites, but the type II basalts vary from 16 ppm for the magnesian ones to 21 for the most iron-rich ones. Hence, if iron metal fractionation affected the Kûgánguaq Member rocks, it did not produce a Ga anomaly.

A few long-time XRF countings by J. C. Bailey indicate Ge concentrations between 1.5 and 2 ppm, without indication of a Ge anomaly at the 1 ppm scale.

Rare earth elements

REE patterns of four uncontaminated basaltic samples from Disko (one type I_B rock, one type II rock, an evolved Maligât Formation basalt and a late Fe-Ti basalt dyke) are shown together with one type III and one type IV sample in fig. 46a (see also Table 22).

The four uncontaminated samples, together with REE data of Baffin Island and Svartenhuk picrites and feldspar-phyric basalts presented and discussed by O'Nions & Clarke (1972) allow the REE patterns of the Kûgánguaq Member rocks to be evaluated.

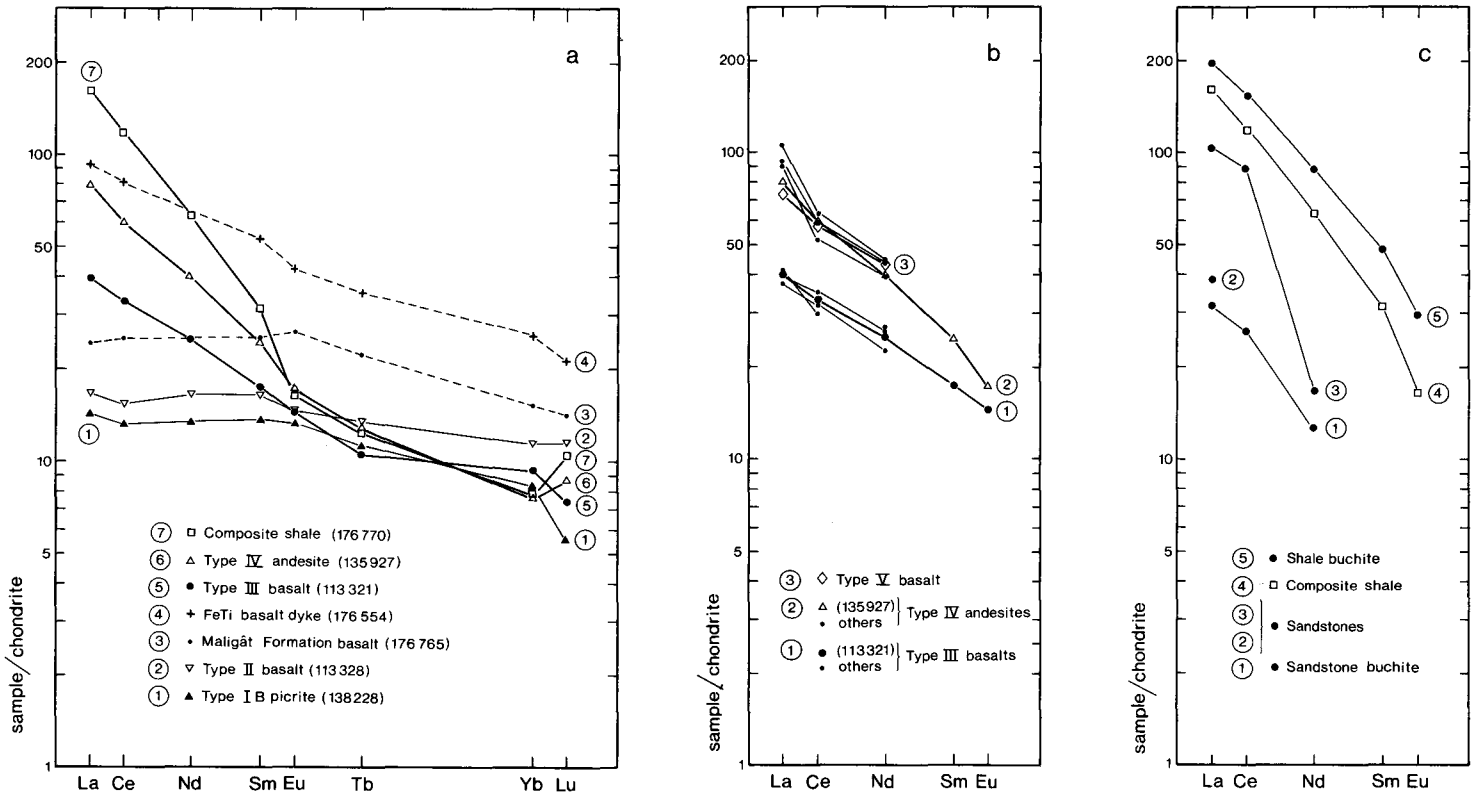

Fig. 46. a: REE analyses from Disko normalized to chondrite (Hickey & Frey, 1982; Evensen *et al.*, 1978, values × 1.27). b and c: Supplementary REE data on La, Ce and Nd (XRF analyses). b: Kûgánguaq Member rocks all show LREE enrichment and imply that the fully analysed type III (GGU 113321) and IV (GGU 135927) samples are representative for these two rock types. c: Analyses of Cretaceous to Tertiary sandstones, shales and their equivalent buchites all show LREE-enrichment patterns.

Table 22. Instrumental neutron activation analyses of rocks from West Greenland

Analysis	1	2	3	4	5	6	7
GGU no.	138228	113328	176765	176554	113321	135927	176770
in ppm							
Sb	0.01	0.06	0.02	0.07	0.05	0.17	0.35
Cs	0.06	0.03	0.13	0.46	0.45	1.38	2.64
La	4.4	5.2	7.5	28.6	12.4	24.8	50.3
Ce	10.6†	12.3†	20.4†	65.1	27†	48†	95
Nd	8.1†	10†			15†	24†	38
Sm	2.67	3.20	4.99	10.5	3.41	4.76	6.14
Eu	0.98	1.10	1.95	3.16	1.07	1.26	1.20
Tb	0.53	0.64	1.07	1.69	0.51	0.61	0.60
Yb	1.72	2.38	3.22	5.46	2.01	1.60	1.64
Lu	0.18	0.37	0.46	0.69	0.24	0.28	0.34
Hf	1.87	2.37	4.42	7.97	2.87	2.50	5.51
Ta	0.31	0.18	0.46	2.66	0.39	0.61	1.08
Th	0.17	0.21	0.46	2.45	2.65	3.90	11.1
U	0.13	0.10	0.35	1.20	0.78	1.56	3.00

Analyses at the Neutron Activation Laboratory at the Geological Museum in Oslo after the procedure by Brunfelt & Steinnes (1969) and Gordon *et al.* (1968).

† XRF analyses at Institute of Petrology, Copenhagen.

1. Picritic pillow from the Vaigat Formation (type I_B).
2. Olivine-poor tholeiitic basalt lava from Qordlortorssuaq Member (type II).
3. Olivine, augite and plagioclase-porphyritic basaltic pillow from the Maligât Formation (Pedersen, 1977a, Table 7, no. 2).
4. Late Fe-Ti basalt dyke from Disko (Pedersen, 1977b, Table 9, no. 3).
5. Olivine microporphyritic basalt from welded tuff in Kûgánguaq Member (type III).
6. Magnesian andesite lava from Kûgánguaq Member (type IV).
7. Composite of 11 unmetamorphosed Mesozoic to early Tertiary shale samples from Nûgssuaq (Pedersen, 1979a, Table 1, no. 1).

Among the uncontaminated rocks from Disko the type I_B and II samples show essentially flat REE patterns ($La/Yb_{E.F.}$ = 1.5 to 1.7 (E.F. = enrichment factor when normalized to chondrite)) and with LREE around 15 times chondrite. The evolved Maligât Formation sample shows a pattern parallel to these ($La/Yb_{E.F.}$ = 1.6) but with distinctly higher total REE abundance, the Fe-Ti basalt dyke showing still more increased total REE levels and relative LREE enrichment ($La/Yb_{E.F.}$ = 3.5).

Of the Kûgánguaq Member rocks the type III sample 113321 shows a distinct LREE enrichment ($La/Yb_{E.F.}$ = 4.2), and this feature is even more pronounced ($La/Yb_{E.F.}$ = 10.5) for the type IV sample 135927. Supplementary La, Ce and Nd analyses for many other Kûgánguaq Member samples (fig. 46b) indicate that the INA-analysed samples are representative for types III and IV. These two rocks show a rather flat HREE pattern of about 8 to 10 times chondrite, which is the same level as found in type I_B rocks, but distinctly lower than the HREE in the type II rocks.

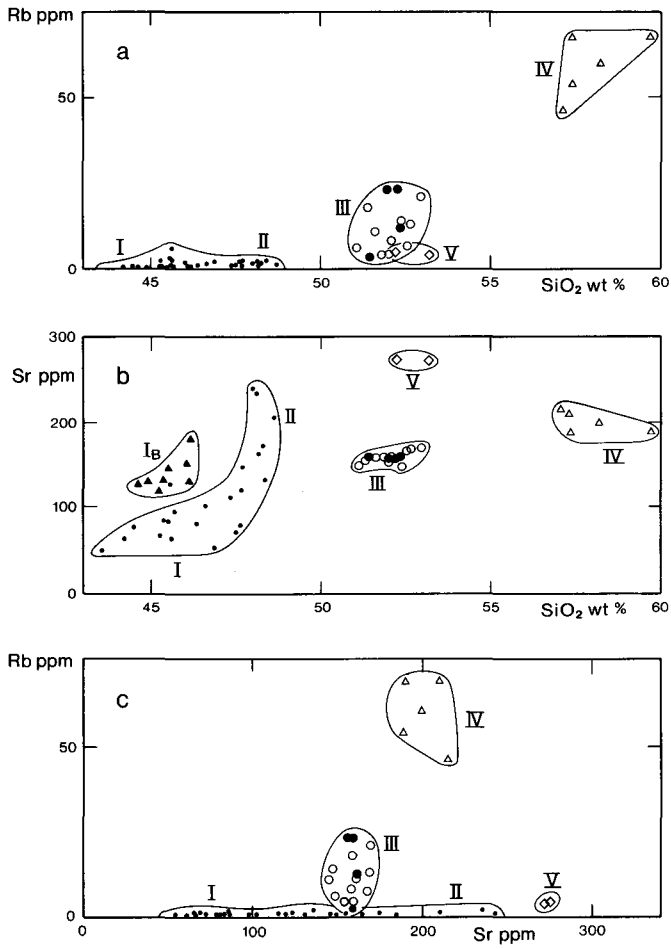

Fig. 47. a: Rb *v.* SiO_2 diagram. b: Sr *v.* SiO_2 diagram. c: Rb *v.* Sr diagram. Note the very variable Rb/Sr ratio within Kûgánguaq Member rocks, ranging from about 0.015 in type V, 0.02 to 0.12 in type III and 0.21 to 0.32 in the type IV andesites, despite the absence of notable amounts of Rb or Sr fractionating phases in type III and IV.

A composite unheated Mesozoic to Tertiary shale sample from Nûgssuaq (Pedersen, 1979a) (fig. 46a) and some other shales, sand and siltstone sediments from the Disko region (fig. 46c) show strongly LREE-enriched patterns ($La/Yb_{E.F.}$ = 11.8) with HREE compositions essentially similar to the picrite (I) and the Kûgánguaq Member samples.

Based on the REE data it can be concluded that an evolved basalt cannot be parental to the Kûgánguaq Member rocks of type III and IV, whereas addition of LREE-enriched and HREE-poor sedimentary components to picritic materials would explain the observed patterns.

Y possesses properties similar to the HREE (e.g. Goldschmidt, 1954), and this is confirmed by the present data (Tables 15, 17, and 18). Y is well correlated with TiO_2 (fig. 49a).

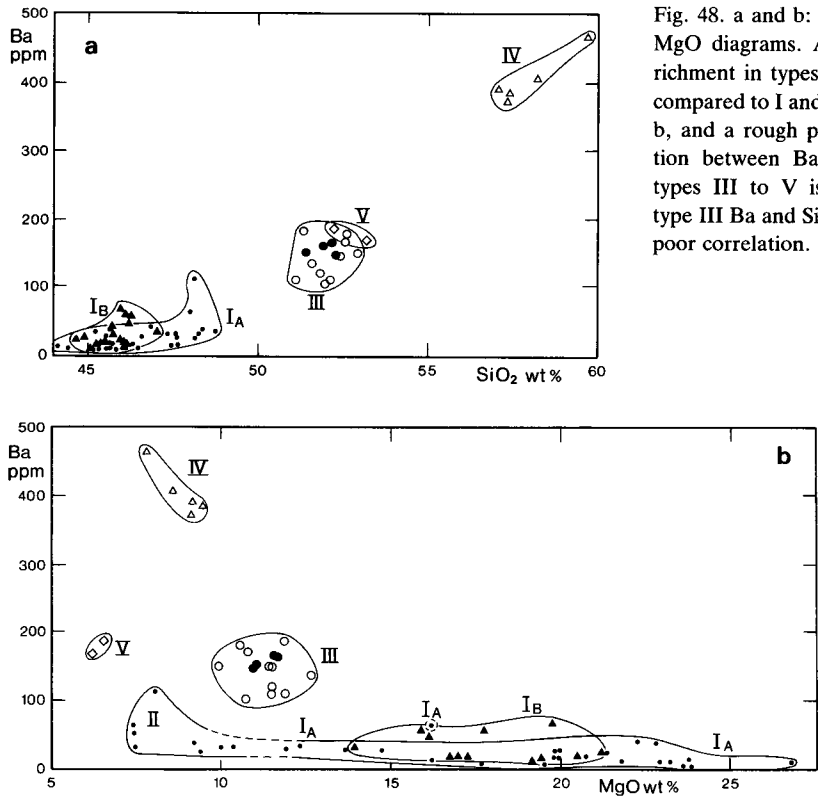

Fig. 48. a and b: Ba *v.* SiO_2 and MgO diagrams. A clear Ba enrichment in types III, IV and V compared to I and II is evident in b, and a rough positive correlation between Ba and SiO_2 for types III to V is seen. Within type III Ba and SiO_2 show a very poor correlation.

Incompatible elements

Among the incompatible elements Rb, Ba, Zr, Hf, Nb, Th, U and Sr will be briefly described below.

Rb varies much like K in the analysed rock samples. The concentrations in type I and II samples are generally a few parts per million or less. Within the type III basalts Rb shows a considerable scatter (fig. 47) with no simple correlation with MgO or SiO_2. Some type III samples are nearly as low in Rb as type I rocks (< 5 ppm) whereas others reach 23 ppm. The type IV samples are strongly enriched in Rb (50–70 ppm), whereas the type V samples are nearly as low in Rb (4–5 ppm) as the uncontaminated type I and II rocks.

Ba generally varies like K and Rb. Ba concentrations are very low in type I and increase to 65 ppm through type II which, however, includes one anomalously enriched sample (113245). The Kûgánguaq Member type III and V rocks are relatively enriched in Ba (100 to 200 ppm) whereas the type IV rocks are strongly enriched (400 ppm). Ba shows a rough positive correlation with SiO_2 in the contaminated rocks (type III to V) (fig. 48a).

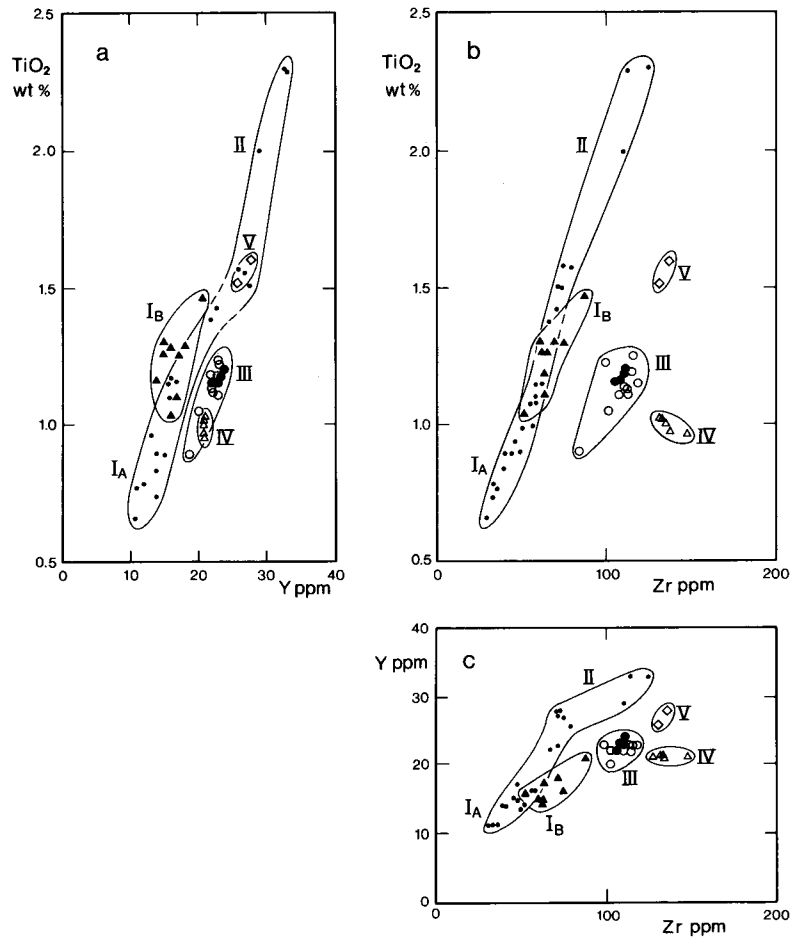

Fig. 49. a: TiO_2 *v.* Y diagram. A clear positive correlation is seen for most rock types, and the Kûgánguaq Member rocks show only a minor deviation from the type I to II trend. Type V basalts overlap with the least evolved type II basalts. b: TiO_2 *v.* Zr diagram. The type I to II basalts show a clear positive correlation. The Kûgánguaq Member rocks are relatively enriched in Zr with type III and V roughly forming a trend parallel to I and II, whereas the andesites deviate by having slightly increasing Zr with decreasing TiO_2. c: Y *v.* Zr diagram. The type I_B rocks show relative enrichment in Zr compared to types I_A to II. Types III and V are characterized by nearly the same Y/Zr ratios as I_B, while type IV is distinctly enriched in Zr.

Zr shows a narrow covariation with TiO_2 (fig. 49b) within the type I to II rocks. At the same MgO and TiO_2 levels the Kûgánguaq Member rocks are all enriched in Zr compared to the uncontaminated type I to II rocks. The Zr–TiO_2 diagram implies distinct addition of Zr from the contaminants.

Only a few INA values have been obtained for Hf. This element (Table 22) varies essentially like Zr.

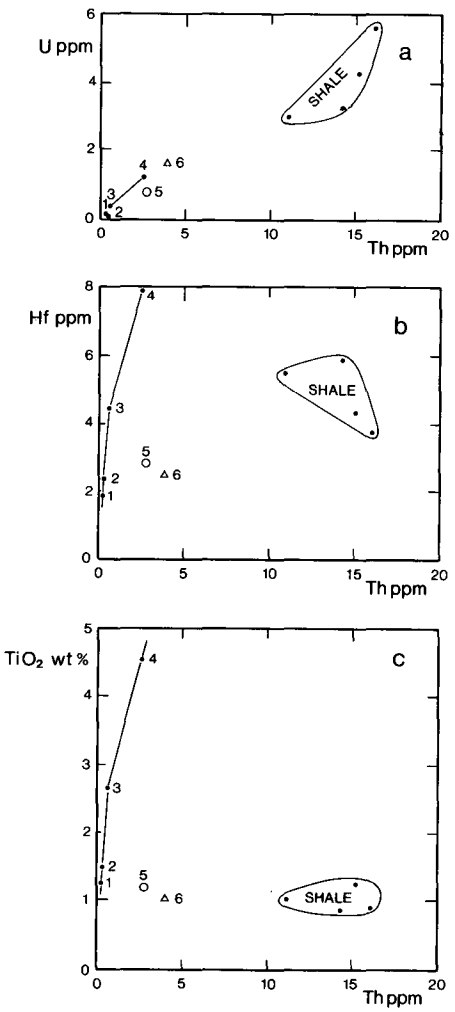

Fig. 50. U, Hf, and TiO_2 *v.* Th diagrams. Numbers 1 to 6 refer to Table 22 and fig. 46a. (1: I_B, 2: II, 3: MF, 4: FeTi, 5: III, 6: IV, 7: composite shale). a: U *v.* Th diagram. Potential parental magmas (type I and II) are very low in these elements. Kûgánguaq Member rocks are distinctly enriched compared to I and II and could have received most of their U and Th from a shale source (Shale). b: Hf *v.* Th diagram. Type I to FeTi basalt magmas define a trend of high Hf/Th ratios. Kûgánguaq Member rocks deviate markedly by being Th enriched and could have been contaminated by materials with Hf/Th ratios typical of shales from the region. c: TiO_2 *v.* Th diagram. Same as b, but the effects are even more marked because of the larger differences in TiO_2/Th ratios.

Nb is very low in the type I rocks (< 2–3 ppm) and in the most magnesian type II rocks (2–3 ppm), increasing to 6 to 10 ppm in the Fe- and Ti-enriched type II rocks. Nb is low in type III rocks (< 2 to 6 ppm) and increases to 8 to 10 ppm in type IV. The highest levels are found in the type V rocks (13–14 ppm). It is concluded that the Kûgánguaq Member rocks have been slightly Nb-enriched by the contaminants.

Only a few values are available for Th and U (Table 22, fig. 50). The analysed type I_B and II rocks are very poor in Th and U, whereas the type III and IV samples are enriched by more than a factor of 10 for Th and 6 for U relative to the uncontaminated rocks. The REE data (fig. 46) indicated that sediments with the chemistry of shales could be possible contaminants. This is strengthened by the U and Th analyses (Table 22) and by the Hf or Ti *v.* Th diagrams (fig. 50b and c) which indi-

Table 23. Sr-isotope analyses of some Kûgánguaq Member rocks

Sample	Type	Rb/Sr	$^{87}Rb/^{86}Sr$	$^{87}Sr/^{86}Sr$	$^{87}Sr/^{86}Sr_0$ (55 m.y.)
138229	III	0.0769	0.223	0.7101	0.7099
113380	III	0.145	0.420	0.7104	0.7101
135924	IV	0.324	0.938	0.7115	0.7108
135927	IV	0.302	0.874	0.7116	0.7109
135972	V	0.0147	0.043	0.7077	0.7077
176770	C. shale	0.425	1.233	0.7279	0.7269

All samples $^{87}Sr/^{86}Sr$; ± 0.0003 (2σ). Eimer & Amend standard = 0.7080. Analyst: S. Pedersen.

cate that the addition of material with shale chemistry to type I and II magma could produce type III and type IV rocks.

Sr behaves as an incompatible element in the picrites in West Greenland prior to the onset of plagioclase crystallization (Clarke, 1970). Data on sedimentary xenoliths from Disko (Pedersen, 1979a) indicate that sediment – magma interaction can lead to extraction of Sr from the magma into xenolith materials. Sr increases from type I_A rocks (unpublished data) to type II rocks with decreasing MgO, reaching about 240 ppm in the least magnesian type II samples. Sr shows very little variation within type III (148–170 ppm) and type IV rocks (190–215 ppm) (fig. 47). The highest Sr contents (about 275 ppm) are found in type V samples, which points to an evolved basalt as parent for type V.

Sr-isotopes

O'Nions & Clarke (1972) have published Sr-isotope data on picrites and more evolved basalts from Baffin Island and Svartenhuk, and these data are assumed to be representative of mantle-derived melts from the region. Pedersen (1981) has presented Sr-isotope data for four andesitic to dacitic iron-bearing samples from the Maligât Formation of north-west Disko and showed these to be extensively contaminated by radiogenic Sr ($^{87}Sr/^{86}Sr$ = 0.7141 to 0.7145) from crustal rocks. Five new Sr-isotope analyses of type III, IV and V samples from the Kûgánguaq Member are presented in Table 23 together with one analysis of a composite shale from Nûgssuaq. All the Kûgánguaq Member samples are strongly enriched in ^{87}Sr compared to the regional picrites, which points to extensive contamination by continental crustal rocks. The Kûgánguaq Member rocks show generally increasing $^{87}Sr/^{86}Sr$ ratios with increasing Rb and Rb/Sr ratios. Most enriched in radiogenic Sr are the type IV rocks (*c.* 0.712) which therefore define the minimum $^{87}Sr/^{86}Sr$-ratio in the contaminant, while the Rb-poor (4 ppm) type V rock is the least radiogenic (*c.* 0.708). Taken together, the Kûgánguaq Member samples define a very crude pseudoisochron with $(^{87}Sr/^{86}Sr)_0 \sim 0.707$ to 0.708 on a $^{87}Sr/^{86}Sr$ *v.* $^{87}Rb/^{86}Sr$ diagram. The Sr in all the analysed samples is distinctly less radiogenic than that in the composite shale from Nûgssuaq ($^{87}Sr/^{86}Sr \sim 0.728$).

Chemistry of immiscible late stage melts

Pairs of mafic and felsic late stage melt phases described from the type III feeder dyke (138229) and from the type IV andesite (135924) have been analysed by energy dispersive microprobe technique (Table 24). The first occurrence of such phases on Disko was noted by Roedder & Weiblen (1971) who briefly stated their presence "in rocks from Disko Island" and found up to 14% TiO_2 and 10.8% P_2O_5 in high-iron glass associated with metal-bearing basalt. Immiscible melt phases have subsequently been found to be very widespread in metal-bearing dyke intrusions on Disko. Philpotts (1982) has compiled abundant data on immiscible melts from tholeiitic and alkaline lava and dyke rocks, and many immiscible melt pairs from lunar basalts are described by Roedder & Weiblen (1972). Comparison of the present data with published values shows that the felsic melt phases from the Kûgánguaq Member rocks are closely similar to the average rhyolitic melt phase from tholeiitic rocks as given by Philpotts (1982, p. 213) (see Table 24, no. 12). The mafic melt phases from Kûgánguaq Member are, on the other hand, unusually high in TiO_2 compared with mafic melts outside Disko, and silica is low, but otherwise the compositions are close to the average mafic immiscible melts in tholeiites (Philpotts, 1982 and Table 24, no. 11). Fig. 51, a pseudoternary Greig diagram from Roedder (1978), demonstrates that in the Kûgánguaq Member rocks conjugate melt pairs plot outside the experimentally determined low-temperature immiscibility field in the system leucite–fayalite–SiO_2. The tie-lines bridge the immiscibility field and nearly overlap with that of the average tholeiitic melt pair, but the Disko pairs indicate a larger immiscibility gap than characteristic of most other rocks. According to Philpotts (1982), early oxidation of a liquid will prevent the iron enrichment necessary to form immiscible low temperature melts, and the prominent development of such melts in the analysed Kûgánguaq Member rocks could be due to their reduced nature.

Summary of results from major and trace element chemistry

Major and trace element relations impose various constraints on possible genetic relations among the described rocks. To simplify the discussion and interpretations below the following conclusions are summarized.

Picrites and olivine-poor tholeiitic basalts (types I_A and II) from the Naujánguit and Qordlortorssuaq Members

The dominant rock type (type I_A) is picrite with about 21 to 23% MgO, characterized by very low levels of imcompatible elements. While resembling the Baffin Island picrites of Clarke (1970) it is distinctly more magnesian than the preferred parental magma which has 18 to 19% MgO.

Table 24. Late stage mafic and acid immiscible 'melt' phases in Kûgánguaq Member rocks

	Olivine microporphyritic basaltic feeder dyke			Magnesian andesite lavas												Average tholeiite	
Analysis	1	2		3	4	5	6		7		8	9		10		11	12
GGU no.	138229	138229		138229	138229	135924	135924		135924		135962	135962		135962			
	Bulk rock	Mafic	1σ (10)	Felsic	Felsic	Bulk rock	Mafic	1σ (10)	Felsic	1σ (5)	Bulk rock	Rhyolite	1σ (4)	Rhyolite	1σ (4)	Mafic	Felsic
SiO_2	51.35	33.4	2.0	72.9	72.2	56.2	31.4	2.3	74.7	1.5	56.51	73.76	0.39	74.81	0.29	41.5	73.3
TiO_2	1.16	11.1	2.0	0.85	1.2	1.00	13.6	2.0	1.1	0.1	0.94	1.08	0.07	0.17	0.08	5.8	0.8
Al_2O_3	14.12	3.1	0.5	11.5	12.3	13.30	2.5	0.8	11.3	0.5	13.23	12.15	0.14	11.81	0.26	3.7	12.1
FeO*	9.17	33.3	2.5	1.3	1.6	7.83	37.2	2.7	1.5	0.5	7.94	0.69	0.07	0.68	0.10	31.0	3.2
MnO	0.16	0.55	0.05	<0.2	<0.2	0.25	0.40	0.15	<0.2		0.13	<0.02		<0.02		0.5	0
MgO	10.28	2.1	0.5	<0.2	0.3	8.95	2.4	0.5	<0.2		9.76	0.07	0.02	0.03	0.01	0.9	0
CaO	8.56	9.3	1.9	1.0	2.0	6.95	7.6	1.3	0.7	0.15	6.74	0.31	0.05	0.18	0.03	9.4	1.8
Na_2O	1.90	0.65	0.45	3.2	3.0	2.30	0.60	0.50	3.0	0.15[4]	2.48	4.14	0.05	4.03	0.13	0.8	3.1
K_2O	0.37	0.45	0.20	2.9	2.3	0.72	0.30	0.20	3.0	0.10[4]	0.75	2.84	0.08	2.88	0.05	0.7	3.3
P_2O_5	0.13	3.6	1.3	0.30	0.10	0.17	3.5	0.70	0.15	0.10	0.18	0.30	0.03[3]	0.16	0.02[3]	3.5	0.07
S	0.06	0.85	0.35[6]	<0.1	<0.1		0.35	0.10	<0.1	0.10		n.a.		n.a.			
less O	–0.03	–0.42					–0.17										
	97.23	97.98		93.95	95.00	97.71	99.68		95.45		98.66	95.34		95.75		97.8	97.67
mg	66.6	10.1		0	0	67.1	10.3		0		68.7	15.3		7.3		4.9	0
CIPW weight norm																	
Q	1.4	7.5		44.1	40.9	8.8	5.8		46.4		6.8	40.6		42.1		4.9	37.8
c				2.1	1.7				2.3			2.4		2.1			0.3
or	2.3	3.1		18.2	14.6	4.3	1.8		18.6		4.5	17.6		17.8		4.2	20.0
ab	16.6	6.8		28.8	29.0	19.9	5.1		26.6		21.3	36.8		35.6		6.9	26.9
an	29.7	4.9		3.2	10.0	24.4	3.2		2.6		23.1					4.5	8.7
di	10.6	17.1				8.0	10.0				7.8					17.5	
hy	36.8	23.9		1.0	1.8	32.3	30.2		1.0		34.3	0.2		0.1		42.4	4.7
ol																	
mt		6.8‡					9.1‡										
il	2.3	17.9		1.7	1.8	1.9	25.8		2.2		1.8	1.5		1.5		11.3	1.6
ru												0.3		0.4		8.3	0.2
ap	0.3	8.7		0.7	0.2	0.4	8.1		0.4		0.4	0.6		0.3			
tro	tr	3.4					1.0										
Cation normative ratios																	
an in Plag.	67.1	41.9		9.5	25.6	53.6	37.6		8.5		50.6	0		0		38.2	23.3
$100 \times Mg/(Mg + Fe^{2+} + Mn)$ in silicates	67.6	20.7		0	50.6	69.0	14.8		0		70.7	100		100		5.7	0

Bulk rocks: XRF analyses, see tables 17, 18 and 19. Analyses of immiscible blebs by E. d. analyses at Institute of Mineralogy, Copenhagen.
Analyses of rhyolitic residiuum in GGU 135962 by W.d. microprobe analyses at Institute of Mineralogy, Copenhagen.
Mafic: Mafic immiscible globules. Felsic: Rhyolitic residuum enclosing mafic globules.
Rhyolite: Clear rhyolite glass without an immiscible mafic melt.
Numbers in parentheses indicate number of analyses. Superscripts to standard deviation is number of analyses.
‡Fe_2O_3/FeO ratio in norm calculation = 0.20 estimated from the composition of late stage titanomagnetites in GGU 138229. $mg = 100 \times Mg/(Mg + Fe^{2+})$.

1. Bulk rock composition. Table 17 no. 1. $Fe_2O_3 = 0$ in norm calculation.
2. Mafic immiscible blebs as shown in Fig. 13 no. b to d.
3. Felsic residuum. Only 1 analysis.
4. Felsic residuum. Only 1 analysis.
5. Bulk rock composition. Table 18 no. 4. $Fe_2O_3 = 0$ in norm calculation.
6. Mafic immiscible blebs, as shown in Fig. 17, b & d.
7. Felsic residuum enclosing mafic blebs.
8. Bulk rock composition. $Fe_2O_3 = 0$ in norm calculation.
9. Interstitial rhyolite glass.
10. Rhyolite glass around quartz xenocryst.
11. Average mafic immiscible blebs in tholeiites as compiled by Philpotts (1982, Table 3, p. 213).
12. Average felsic residual immiscible melt in tholeiites as compiled by Philpotts (1982, Table 3, p. 213).

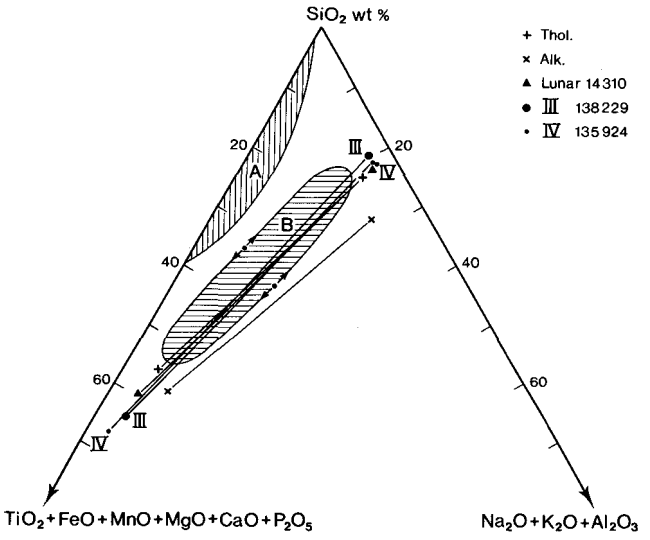

Fig. 51. Pseudoternary SiO_2–(Na_2O + K_2O + Al_2O_3)–(TiO_2 + FeO + MnO + MgO + CaO + P_2O_5) diagram showing pairs of immiscible late stage melts in Kûgánguaq Member rocks. Experimentally determined low temperature immiscibility fields from Roedder (1978). In addition to the type III basalt (GGU 138229) and the type IV andesite (GGU 135924) pairs from Lunar rock 14310 (Roedder & Weiblen, 1972) and from average tholeiitic (Thol.) and alkaline lavas and dykes (Alk.) (Philpotts, 1982) are shown.

The type I_A rocks define an olivine control line, which at the evolved end is terminated by type II rocks controlled by olivine + plagioclase + melt and olivine + augite + plagioclase + melt equilibria. Plots of some incompatible elements against each other show linear trends with positive slopes which substantiate, but do not prove, the comagmatic nature of these rocks.

Picrites from the Ordlingassoq Member (type I_B)

The dominant rock type is a picrite with between 16 and 19% MgO. Compared with type I_A the I_B picrites are slightly enriched in incompatible elements at the same MgO levels and are very similar to Clarke's (1970) Svartenhuk picrites, and the dominant I_B rock being very similar to the estimated Svartenhuk parental magma.

Olivine microporphyritic basalts (type III) from the Kûgánguaq Member

If it is assumed that type III rocks do not represent an independent primary magma derived from an exotic mantle, the following constraints emerge.

1. The high $^{87}Sr/^{86}Sr$ ratios demonstrate that mantle-derived parental magma has reacted with crustal rocks.
2. The basic parent was so Mg and Cr rich that it must have been picritic. One non-cumulative type III sample was derived from a parent with at least 21% MgO, and all the others from parents with at least 18% MgO.

3. The low levels of elements like Nb and P clearly indicate a non-alkaline parental magma.
4. Comparison of REE patterns in contaminated and uncontaminated samples shows that the low HREE level in the analysed type III sample constrains the parent to contain well above 10% MgO.
5. The chemical variation within type III rocks indicates minor olivine fractionation in the type III magmas.

In conclusion of points 1 to 5, the chemistry points to a magnesian (> 18% MgO) type I rock as parent for type III rocks. Geologically and chemically the dominant type I_A magma with 21 to 23% MgO, is the most likely candidate.

The crustal reactant cannot be unequivocally identified, since only one vesiculated, partially melted, and strongly carbonated, xenolith resembling sandstone has been found, from which no representative chemical analysis could be obtained.

However, the following observations constrain its composition.

6. Marked depletion of the chalcophile elements Ni and Cu (and to a minor extent Fe) is attributed to sulphur addition from the contaminant and subsequent fractionation of a sulphide (+ minor Fe metal?) from the type III magma. This occurred prior to the crystallization of the phases now present in the type III rocks.
7. Type III rocks show distinct LREE enrichment, increasing from Nd to La, which must be derived from the crustal reactant. Addition of LREE-enriched components from Cretaceous to Tertiary sediments to type I_A rocks would explain the observed patterns. The addition of other, unobserved, crustal components could of course equally well explain the patterns.
8. Distinct enrichment in some incompatible elements such as Zr, Hf, P, Nb, U and Th is noted and must be attributed to the crustal component.
9. A distinct, but irregular enrichment noted for elements like K and Rb is not only caused by post-eruptional hydrothermal metamorphism, but must reflect inhomogeneities in the crustal component, or possibly volatile transport at the roof of the magma chamber.
10. Major element modifications include addition of SiO_2, marked decrease in CaO/Al_2O_3 ratios, and decrease in FeO^{total}. In addition to the precipitation of olivine, some process other than simple mixing must have occurred. Previous xenolith studies from Disko (Melson & Switzer, 1965; Pedersen, 1979a) suggest that diffusion of some elements from the magma into contaminant rocks has occurred.

Magnesian andesites (type IV) from the Kûgánguaq Member

These rocks have been affected by interaction with the same crustal components that affected the type III rocks, but to a more extreme degree. Because of this, the

basic parental magma is more strongly modified and hence less easy to identify. The following constraints apply.

1. A minimum of 13 to 15% MgO in the parent is implied from the Cr-data.
2. Sulphide extraction of Ni and Cu has been ineffective, probably due to higher magma viscosity than that for the type III basalts.
3. The REE data are compatible with the same parent as for type III rocks, but the additions of LREE from the crustal component have been larger.
4. The Ti–SiO_2 data show TiO_2 dilution effects with increasing SiO_2, which identifies the crustal component as being TiO_2-poor (1.00%).
5. There is no clear evidence of crystal fractionation. Even minor orthopyroxene fractionation would increase TiO_2 and markedly decrease Cr, V and Sc, but the observed variation implies only passive dilution by the crustal component.
6. Major and trace elements exclude the possibility that type IV is derived from III by crystal fractionation of the observed phases.
7. The widespread occurrence of resorbed quartz xenocrysts in the andesites, and the pronounced silica enrichment, point to sandstone as the crustal component. Gneissic to granitic rocks cannot be excluded, but positive evidence is lacking.

From the evidence presented for type III and IV rocks it is concluded that both types originated from a picritic parent and that type IV is more strongly contaminated than type III. Petrographic evidence points to sandstone as the likely contaminant. However, evidence from REE and other trace elements indicates that the concentration of these elements in the contaminant was similar to values found in Mesozoic to Tertiary shales and siltstones from Disko and Nûgssuaq. As a very simplistic approximation to estimate the extent of contamination (neglecting selective contamination, Watson, 1982) as well as complex equilibration reactions at contacts) simple mixing calculations have been made below (Table 25). Mixing of a type I rock (represented by sample 138228 and a composite shale (sample 176770, Pedersen, 1979a)) to give a type III (113321) and a type IV (135927) rock was performed for incompatible elements since these showed distinctive concentration differences between parent and contaminant.

For the elements La, Nd, Sm, U and Th the contribution from contaminants can be estimated to amount to between 17 and 23% by weight for the type III sample (113321), and to between 34 and 60% for the type IV sample (135927). The actual volumes of contaminants transferred to the magmas were probably much smaller, since it is likely that the incompatible elements became strongly concentrated in partial melts in the sediments.

It is, however, interesting to note that if the same calculations are performed for SiO_2 and the value SiO_2 = 75 wt.% is assigned to the contaminant (a likely value for some sandstone and siltstones as well as for rhyolitic melt in partially molten

Table 25. Estimation of the extent of contamination of a type III and a type IV rock based on some incompatible elements

Element	Percent contaminant added to parent in: Type III (113321)	Type IV (135927)
Rb	16	84
Ba	32	98
Zr	44	66
Hf	28	17*
Nb	27	64
La	17	44
Nd	23	53
Sm	21	60
Th	23	34
U	23	50

Parent: Type I picrite 138228 (Tables 15 and 24, and unpublished data).
Contaminant: Composite shales from Nûgssuaq (Table 24 and Pedersen, 1979a, table 1).
Simple mixing: $a_1x + a_2y = a_3$.

a_1 concentration of element in parent.
a_2 concentration of element in contaminant.
a_3 concentration of element in Kûgánguaq Member rock.
x weight fraction parent.
y weight fraction of contaminant.
$x + y = 1$.
* Indicates dubious Hf value for 135927.

sandstone or siltstone) then the values obtained (23% for type III and 41% for type IV) are similar to those indicated for the incompatible elements cited above.

Feldspar-phyric silicic basalts (type V) from the Kûgánguaq Member

These rocks represent basaltic melt coexisting with olivine (pseudomorphosed) + orthopyroxene + augite + plagioclase and could hence represent compositions erupted at a low pressure pseudo-invariant reaction point (e.g. Chinner & Schairer, 1962; Stolper, 1980). The following constraints can be applied.

1. The high $^{87}Sr/^{86}Sr$ ratio determined for type V samples demonstrates that mantle derived parental magma has reacted with crustal rocks.
2. High Cr in the magma indicates that the parental magma contained at least 11 to 13% MgO.
3. Both the major element chemistry, and the concentrations of the elements Ti, P, Sc, V, Nb and Y, indicate that the type V parent rock had become an evolved

basalt with some major and trace element characteristics similar to evolved type II basalts.

4. Low levels of elements such as Ni and Cu are taken as definite evidence for sulphide fractionation.
5. Low levels of K and Rb indicate that there was only limited reaction with crustal material.

In conclusion, the type V rocks have been derived from an already evolved type I_A to II rock (11 to 13% MgO). After reaction with crustal contaminants, which involved sulphide fractionation, the magma evolved to a pseudo-invariant reaction point. Cr remained unusually high for an evolved basalt, probably because reducing components from the contaminants delayed the crystallization of chromite.

DISCUSSION AND INTERPRETATION

This section first attempts to apply mineral thermometry to the Kûgánguaq Member rocks and to their supposed parents; the transition element chemistry of olivine, chromite and glass is then discussed in relation to f_{O_2} and f_{S_2}, and finally the Kûgánguaq Member volcanism is reassessed.

Estimation of temperature from olivine-melt thermometry

Iron and magnesium partitioning between olivine and melt,

expressed as $K_D = (X^{ol}_{FeO}/X^{ol}_{MgO})/(X^{liq}_{FeO}/X^{liq}_{MgO})$

has been shown to be close to a value of *c.* 0.30 for a wide range of compositions, temperatures and pressures by Roeder & Emslie (1970) and Roeder (1974). Recent iterative calibration of a large number of experimental olivine–glass data by Ford *et al.* (1983) has, however, demonstrated that K_D is clearly composition and pressure dependent, and their reformulated olivine thermometer is applied here.

The Kûgánguaq Member rocks and their proposed parent magmas of type I and II were all olivine saturated at their liquidus. From the K_D relation (Ford *et al.*, 1983) and analyses of olivines, glasses and bulk samples, and an estimated pressure, it is possible (1) to estimate liquidus olivine compositions and liquidus temperatures from bulk analyses, and (2) to estimate the MgO in the magma in equilibrium with actually analysed olivine phenocryst compositions.

Table 26 summarizes estimated liquidus and quench temperatures and the corresponding olivine compositions.

Type I. The type IB glass sample 136943 carries olivine with a compositional range from *mg* = 92.3 to 85.8. Its 1 bar liquidus temperature is 1424°C (olivine, *mg* = 92.4) and the 10 kb temperature is 1475°C (olivine, *mg* = 91.7). The glass itself indicates a 1 bar quench temperature of about 1200°C. The more magnesian type I_A samples 156717 would have a 1 bar liquidus temperature as high as 1473°C and more magnesian liquidus olivine (*mg* = 93.7) than has ever been analysed from the Vaigat Formation picrites.

Type II. The investigated type II samples show a wide range in estimated liquidus temperatures from *T*= 1251°C (olivine, *mg* = 86.2) to *T*= 1180°C (olivine, *mg* = 79.4). The estimated olivine compositions contrast markedly with the analysed olivine cores (*mg* = 65) from the magnesian type II sample 113325, indicating that the ferromagnesian silicates experienced extensive equilibration during the cooling of this thick lava flow.

Table 26. Thermometry based on olivine–melt equilibria

Rock	Source	Type	Anal. MgO[†]	Anal. FeO*[‡]	Est. or calc. Fe_2O_3/FeO[$]	Calc *mg* in olivine at T_{sum}°C, 1 bar	T_{sum}°C,[¶] 1 bar	K_D,[††] 1 bar	Calc *mg* in olivine at T_{sum}°C *P* bar	T_{sum}°C	*P* bar	K_D, *P* bar
156717	Table 14 anal. 1	I_A	21.15	10.20	0.20	93.7	1473	0.294	93.1	1524	10 000	0.324
136943	Table 14 anal. 6	I_B	18.48	10.89	0.20	92.4	1424	0.294	91.7	1475	10 000	0.324
136943 glass	Table 16 anal. 1		8.48	10.64	0.20	84.3	1198	0.312				
113236	Table 15 anal. 1	II	10.20	10.75	0.15	86.2	1251	0.307				
113328	Table 15 anal. 4	II	9.17	10.74	0.15	84.7	1225	0.312				
113330	Table 15 anal. 6	II	7.41	12.35	0.15	79.4	1180	0.315				
113317	Table 17 anal. 10	III	12.50	8.92	0	88.6	1314	0.320				
138229	Table 17 anal. 1	III	10.28	9.17	0	86.1	1274	0.323				
113321	Table 17 anal. 11	III	10.80	9.45	0	86.3	1279	0.325				
113321 glass	Table 20 anal. 2		9.21	8.93	0	85.1	1240	0.320				
264110	Table 19 anal. 7	III	10.97	9.07	0	87.1	1286	0.320				
264110 glass	Table 20 anal. 5		7.20	8.45	0	82.3	1188	0.327				
135962	Table 18 anal. 6	IV	9.76	7.94	0	87.0	1290	0.328				
135927	Table 18 anal. 2	IV	8.33	7.69	0	85.4	1265	0.331	85.2	1269	1000	0.335
135972	Table 18 anal. 7	V	6.11	9.41	0	77.6	1151	0.333				

Applied formula: Ford *et al.* (1983, eq 3 p. 259; coefficients from table 2, p. 261).

[†]1 Analysed MgO wt.% in rocks or glasses.
[‡]2 Analysed FeO* in rocks or glasses.
[$] 3 Estimated Fe_2O_3/FeO in rocks and glasses, see section on f_{O_2}.
[¶]4 Olivine saturation temperature T_{sum}°C as defined in Ford *et al.* (1983).
[††]5 $K_D = (X^{ol}_{FeO}/X^{ol}_{MgO})/(X^{liq}_{FeO}/X^{liq}_{MgO})$

Type III. The type III bulk rock liquidus temperatures range from T= 1314°C (olivine, *mg* = 88.6) for the most magnesian sample 113317 to about T= 1275°C for typical type III compositions. The glass phases span a considerable range, from T = 1240°C (olivine, *mg* = 85.1) in the welded tuff 113321 to T = 1188°C (olivine, *mg* = 82.3) in the type III glass from the Ordlingassoq Member (sample 264110). In general, the compositions of the most magnesian olivines analysed from type III samples are similar to the calculated liquidus olivines.

Type IV. Calculated liquidus temperatures for the type IV samples are very high (about 1290 to 1265°C) for such silicic rocks, and the most magnesian analysed olivines (*mg* = 87 to 86) are very similar to the calculated composition of the liquidus olivine (*mg* = 87.0 to 85.4).

Type V. The type V samples, which only contain traces of olivine pseudomorphs, show a very low calculated liquidus temperature (T = 1151°C) and less magnesian liquidus olivine (*mg* = 77.6) than any other Kûgánguaq Member rocks.

Estimation of temperature from pyroxene thermometry

Lindsley & Andersen (1983) and Lindsley (1983) have recently formulated a graphical two-pyroxene thermometer and a specific scheme to project pyroxenes into the system Wo–En–Fs. This projection has been applied for two pyroxene pairs in the type V sample 135972 (Table 9, nos 6 and 7). One atmosphere temperatures obtained are around 1180–1200°C, which is higher than the olivine saturation temperature (1151°C). Two large crystals of groundmass pyroxene (unpublished wavelength dispersive analyses) from the type IV magnesian andesite sample 135945 (fig. 26c) give temperatures around 1100°C. Finally, a temperature estimate was attempted on pyroxenes crystallized in vugs in the large type III hornfels tuff 113380 (Table 9, nos 9 and 10). The calcic clinopyroxene yields T= *c.* 1130°C while the orthopyroxene gives 1000–1100°C, but it is likely that a true equilibrium assemblage was never established in this rock.

Estimation of pressure

No useful mineral barometers have been found in the Kûgánguaq Member rocks. Some general indication that the Kûgánguaq Member rocks are low pressure equilibrated comes from the fact that the type III basalts crystallized at least 8 vol.% of olivine before the appearance of low Ca pyroxene, and that the distinctly quartz-normative type IV andesites crystallized early olivine. Higher pressures increase the primary phase volume of orthopyroxene (Boyd *et al.*, 1964; Chen & Presnall, 1975) and markedly reduce that of olivine. This would be counteracted by a high P_{H2O} (Kushiro, 1972), but evidence of a high P_{H2O} is notably lacking in these rocks. The phase relations at low dry pressure of Bushveld samples (Cawthorn & Davies, 1983), very close in composition to Kûgánguaq Member type III and IV

samples, strongly suggest that the Disko rocks equilibrated at pressures < 3 kbar, and in the case of type IV the pressure must have been distinctly less.

Estimation of f_{O_2}

Recent experimental work has permitted empirical calibration of oxygen fugacities from ferric–ferrous ratios at known high igneous temperatures for a wide range of silicate melt compositions, including the present rocks (Sack *et al.*, 1980; Kilinc *et al.*, 1983). The calibration now ranges from oxygen fugacities at one order of magnitude below the FMQ buffer to those in atmospheric air. Unfortunately direct f_{O_2} determination from ferric–ferrous ratios in the present chemical rock analyses is rarely possible due to combinations of deuteric oxidation, high temperature metamorphism, and late regional low temperature metamorphism. In the present study the estimates of f_{O_2} variations are therefore only qualitative. They are based on

(1) The composition and modes of Fe-Ti oxide phases, and
(2) Transition metal chemistry in glass, chromite and olivine.

Composition and abundance of Fe-Ti oxides

Coexisting ilmenite and titanomagnetite allow the determination of T and f_{O_2} in rocks (Buddington & Lindsley, 1964; Spencer & Lindsley, 1981). In the Kûgánguaq Member rocks Fe-Ti oxides crystallized late, and no usable oxide pairs which could provide temperatures of magmatic crystallization have been found in the present study. The modal abundance of Fe-Ti oxides in Kûgánguaq Member rocks are generally low (Table 1), and those samples with least late stage deuteric oxidation (138229, 135924 and 135927) are remarkably low in well crystallized Fe-Ti oxides, carrying a large part of their oxide component in mafic immiscible blebs. A plot of modal Fe-Ti oxides *v.* TiO_2 (fig. 52) illustrates this, and shows that uncontaminated type II samples are much richer in Fe-Ti oxides than the Kûgánguaq Member samples with only slightly lower TiO_2 contents. This indicates that the type III and IV rocks are reduced compared to the regional uncontaminated basalts, and the composition of the late titanomagnetite (usp/(usp + mt) = 0.82) in the type III feeder dyke gives the same indication.

Composition of the glass

Of the elements Ti, V, Cr, Ce, Eu, Hf and Zr (disregarding Fe), which occur in more than one valency state under reducing conditions and at igneous temperatures (e.g. Schreiber, 1977; Schreiber *et al.*, 1982), only Cr and Ti have been analysed in the glasses. While Ti shows no apparent redox-controlled anomalies, the unusually high Cr in type III glasses must be ascribed to low prevailing f_{O_2}.

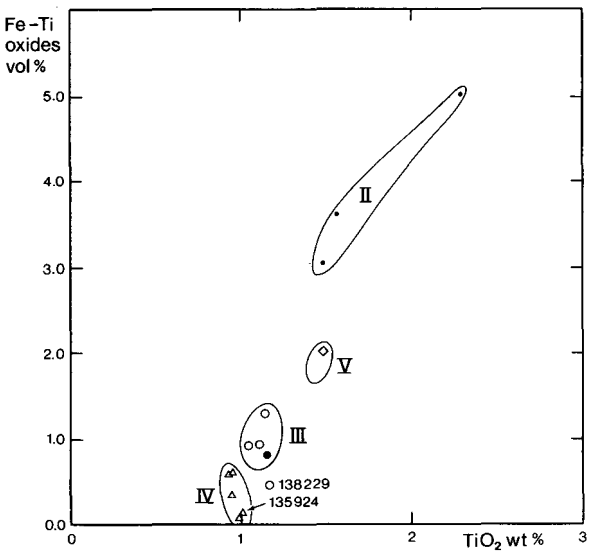

Fig. 52. Modal Fe-Ti oxides in vol.% (outside late stage immiscible blebs) *v.* TiO_2 (wt.%). Note the low abundance of Fe-Ti oxides in some Kûgánguaq Member type III and IV rocks compared to well crystallized type II basalts. The type V sample is a vesiculated and subsolidus oxidized lava.

The solubility of Cr in basic magmas is known to be strongly dependent on T and f_{O_2} (e.g. Hill & Roeder, 1974; Maurel & Maurel, 1982a), Cr solubility increasing with T and decreasing f_{O_2}. In addition, the solubility is dependent on the melt composition (e.g. Irvine, 1975b; Schreiber & Haskin, 1976), but the effects are not quantitatively calibrated.

Fig. 43 shows Cr_2O_3 *v. mg* in glasses from type I samples and other more evolved uncontaminated basalts from Disko compared to type III glasses. The estimated quench temperatures for type I glasses fall within the range for type III glasses. Given the same T and f_{O_2}, the more silicic type III glasses should dissolve less Cr than the type I glasses according to Irvine (1975b). Therefore, the fact that Cr is a factor of 3 higher in type III than I glass indicates that much more reducing conditions prevailed in the type III magma. The experimental work by Hill & Roeder (1974) and Maurel & Maurel (1982a) would suggest a difference in f_{O_2} of about 3 orders of magnitude.

Another example of f_{O_2}-dependent Cr solubility is shown by the two, nearly identical, chromite-saturated type III glasses (Table 20): the tuff (138348) from the Kûgánguaq Member and the pillow glass (264110) from the Ordlingassoq Member, which is the only type III material from outside the Kûgánguaq Member included in this study. Sample 138348 contains about twice as much Cr as 264110 and must have been distinctly more reduced than the latter.

Composition of the chromite and evidence from chromite-glass equilibration

The following redox-sensitive elements will be discussed: Cr, Fe and V. Chromium almost exclusively enters spinel phases as Cr^{3+}, even when crystallizing in magmas with $Cr^{3+} \ll Cr^{2+}$ (Schreiber & Haskin, 1976), and even under extremely

reducing conditions no evidence for Cr^{2+}-substitution has been found in Disko spinels (Pedersen, 1978b). All Cr is therefore assumed to be present as Cr^{3+} in the chromites studied here.

This study has shown the presence of substantial Fe^{3+} substitution in all the chromites in type I_B glass samples (fig. 22). Of particular interest is the fact that even chromite in glass inclusions in the core of clear, very magnesian ($mg = 92.3$) olivine phenocrysts also shows the same distinctive ferric iron enrichment as the free chromite microphenocrysts in the glass. This demonstrates that the redox conditions, which characterize the type I_B glasses, originated early in their evolution at high temperatures before they reached the Earth's surface.

Several experimental investigations have been made on the relation between ferric–ferrous ratios in chromites and coexisting basaltic glass (melt) at 1 atm. (Maurel & Maurel, 1982b; Roeder, 1982). The experimental range ($f_{O_2} = 10^{-6}$ to 10^{-9}) covers the studied type I glass samples and permits an estimate of the Fe_2O_3/FeO ratio in the glasses. From the estimated ferric–ferrous ratios and the bulk composition of the glass phase, and with the temperature obtained from olivine-glass thermometry, f_{O_2} is calculated from the work of Sack *et al.* (1980). Table 28 summarizes data for some of the investigated type I_B samples. The f_{O_2} values obtained are close to the NNO buffer and distinctly above FMQ. Some oxidized olivines contain magnesioferrite and would indicate even higher f_{O_2} locally.

In chromite from type III to V samples calculated ferric iron varies substantially (figs 22, 23 and 25), but values from chromite in quenched samples are invariably much lower than values in quenched type I rocks.

Attempts to estimate the Fe_2O_3/FeO ratio from the chromite in quenched type III and IV samples, and subsequent calculation of f_{O_2}, show that these rocks are more reduced than the compositions covered by the experimental equilibration range ($f_{O_2} < 10^{-9}$ at $T = 1180$ to 1399°C). For this reason a more crude estimation of f_{O_2} has to be made. From experimental results (in the range $T = 1080$ to 1300°C and $f_{O_2} = 10^{-3}$ to 10^{-9}) Maurel & Maurel (1982b) made a correlation equation between ferric–ferrous ratios in chromite and glass, but noted that the dependence on melt compositions was not well constrained. As a more general relation, they found that $Fe^{3+}/Fe^{2+}_{chromite} > Fe^{3+}/Fe^{2+}_{melt}$, and this relation has been extrapolated to lower f_{O_2} in order to estimate maximum ferric–ferrous ratios in quenched type III and IV samples (Table 27). The values are clearly lower than (a) ratios calculated for the same rocks at the FMQ-buffer (Sack *et al.*, 1980) and (b) the analytically determined oxidation ratios in the rocks, indicating that the rocks have been subsequently oxidized.

In conclusion, the ferric–ferrous ratios calculated for chromite in the quenched type III and IV samples show that these magmas, just prior to eruption, were all characterized by f_{O_2} distinctly, below 10^{-9} (the experimental calibration range) and well below the WM buffer – that is more than one, and more likely two to three orders of magnitude below that characterizing the type I magmas.

Even the type V chromite in lava sample 135972, which is likely to have been oxi-

Table 27. Calculation of f_{O_2} from chromite–glass data

Sample	Type	Chromite	Fe^{3+}/Fe^{2+} in chromite	Fe^{3+}/Fe^{2+} in glass, from eq 1	T°C from olivine-glass thermometry see Table 27	log f_{O_2} after Sack *et al.* (1980)
136943	I_B	Table 5 no 4	0.638	0.198	1198	– 7.65
264104	I_B	Table 5 no 8	0.615	0.188	1195	– 7.95
264104	I_B	Table 5 no 9	0.857	0.291	1195	– 7.00
264137	I_B	Unpubl.	0.692	0.220	1204	– 7.35
264110	III	Table 7 no 7	0.131	0.025	1188	–11.75†
264110 glass	III		0.407	0.110	1188	– 9.00‡
113321 glass	III		0.295	0.072	1240	– 9.00‡

General conclusion: All quenched type III rocks equilibrated at $f_{O_2} \ll 10^{-9}$.
Equation 1; from Maurel & Maurel, 1982b, p. 211 for 1180C $\leqq$ T°C $\leqq$ 1300 and $10^{-9} \leqq fO_2 \leqq 10^{-3}$.
For $f_{O_2} < 10^{-9}$ maximum Fe^{3+}/Fe^{2+} in melt is given by $(Fe^{3+}/Fe^{2+})_{sp} > (Fe^{3+}/Fe^{2+})_{liq}$, where sp = spinel phase and liq = melt.
†Extrapolation far outside the calibration range.
‡Calculated limiting compositions at the lower f_{O_2}-calibration range.

dized to some extent during the cooling of the lava, still records a f_{O_2} value well below the calibration range of 10^{-9}.

Several samples of Kûgánguaq Member lavas and of the metamorphosed tuffs contain chromite which was clearly equilibrated at near solidus to subsolidus temperatures. Chromite in different samples shows different Fe^{3+} enrichment trends (fig. 22, 24) from which a sequence of increasing f_{O_2} can be noted (138229 < 135975 < 113380); however, the extent of the oxidation processes has not been quantified.

Vanadium is present predominantly as V^{5+} at igneous temperatures at f_{O_2} close to or higher than FMQ (see discussion in Schreiber, 1977 and Shervais, 1982). As f_{O_2} decreases, species such as V^{4+} and V^{3+} become increasingly important. With decreasing f_{O_2} the spinel-phase/melt partition coefficient for V (D_V) has been found to increase very markedly (Lindstrom, 1976, cited in Irving, 1978). In Table 28 approximate partition coefficients (D_V) for type I_B and the Kûgánguaq Member rocks are given. The very small abundances of chromite in type III to V samples (Table 1) and in type I_B glass samples (0.3 vol.%) show that less than 10% of the total V in the rocks is partitioned into chromite. Since V has not been analysed in the glasses or matrices with the microprobe, partition coefficients are here $V_{Chromite}/V_{Bulk\ rock}$. For the picrites this gives higher values than would be obtained for chromite/glass pairs, whereas the effect is very minor for the other rocks.

The partition coefficients (D_V) in type I samples are around 4, whereas type III values are about 35 to 40. In the type IV samples the chromite shows both varying V and Fe^{3+} (fig. 23). The quenched andesite tuff 135961 and lava sample 135927

Table 28. Mineral–glass partition coefficients

Sample	Type	D_{Ti}-olivine/glass	D_V-olivine/glass	D_V-chromite/glass
136943	I_B	0.006–0.008	< 0.08	< 6
Maligât Formation basalt 176765*		0.006–0.009	< 0.08	no chromite
Fe-Ti basalt dyke 176554†		0.013–0.017	< 0.07	no chromite
113374‡	III		*c.* 0.20	*c.* 22
113321	III	0.012	0.12–0.21	20–34
113380§	III		*c.* 0.07	
138229¶	III	0.008	*c.* 0.24	31–35
264110	III	0.008–0.016	0.2–0.3	35–40
135961**	IV	0.015	*c.* 0.40	*c.* 30–35
135962¶	IV	0.010	*c.* 0.15	*c.* 11
135972¶	V			*c.* 40
Basaltic glass rock with metallic iron 176669††	similar to type III	0.016	1.0	no chromite

* Major elements in Pedersen (1977a, Table 7, no. 2).
† Major elements in Pedersen (1977b, Table 9, no. 3).
‡ The sample is a tuff with altered matrix. Glass values estimated as typical type III compositions.
§ Metamorphosed tuff, the low D_V-olivine/glass is interpreted as due to metamorphic equilibration.
¶ Only the composition of the bulk rock is known.
**Tuff sample with altered glassy matrix. Glass values estimated as typical type IV compositions.
†† Described by Pedersen (1979b, Table 2).

show coefficients from 35 to 23, whereas other samples range down to 11. In the type V sample the coefficient is around 40.

The compositional effect on V solubility in the different silicate magmas at constant T and f_{O_2} cannot be assessed at present, but the analysed or estimated V concentrations vary only by a factor of 2 in the bulk rocks and glasses, but by up to a factor 10 to 15 in the chromites. The marked increase in D_V chromite/glass from type I to type III, IV and V was presumably caused by a shift from more oxidized V^{5+} in type I magma to more reduced V^{4+} and V^{3+} in the type III to V magmas, where the reduced V would enter the spinel structure more easily. In the Lindstrom experiments (Irving, 1978) a comparable shift in D_V was attained by a decline in f_{O_2} by 3.5 orders of magnitude, but the chemical system was different and the temperature lower (1110 to 1135°C), so quantification of the Disko results is not justified.

Another important point emerges from the chromite data from type III samples: high V concentrations in chromite established during early chromite precipitation

at low f_{O_2} were retained or only slightly decreased when the chromites were subsequently oxidized at near solidus or subsolidus temperatures (figs 22 to 25).

In conclusion, D_V chromite/glass is highly f_{O_2} sensitive and an important parameter which can be used to estimate the relative f_{O_2} in quenched magnesian basalts and andesites in the f_{O_2} range from the NNO and perhaps to the IW buffer.

Composition of the olivines

The following redox-sensitive elements will be discussed: Ti, V and Cr. Ti is almost exclusively present as Ti^{4+} in normal terrestrial magmas, and even in a haplobasaltic model system at 1250°C at the IW buffer only about 2% of the Ti is present as the reduced species Ti^{3+} (Schreiber *et al.*, 1982). In the present work no distinctive Ti anomalies have been found (fig. 20e). Calculated partition coefficients for olivine/glass pairs in glass samples which range from type I to Fe-Ti basalt vary only between 0.006 and 0.017, while partition coefficients estimated for type III and IV samples vary between 0.008 and 0.016 (Table 28). The glass samples from Luciefjeld which are estimated to have quenched close to the IW buffer (Pedersen, 1979b) show $D_{Ti} = 0.017$. It must be concluded that no evidence for Ti^{3+} anomalies has been found in the rocks studied here.

Vanadium does not easily enter olivine under normal terrestrial conditions, and experimental determination of D_V olivine/glass pairs show low values at FMQ (0.04, Lindstrom, 1976 cited in Irving, 1978). Ringwood (1970) has reported a much higher D_V (1.3) in an olivine/glass pair synthesized in an Apollo 11 composition at low f_{O_2}, and Pedersen (1979b) reported a $D_V = 1.0$ in an olivine/glass pair from iron-bearing glass at Luciefjeld. Fig. 20f shows how the olivine from this rock deviates very markedly from the olivines investigated in this study.

The picritic to FeTi basaltic olivines are poor in V and all show D_V below 0.1, and in some rocks D_V can be constrained to below 0.06 (Table 28) which is in accordance with Lindstrom's experiments. In quenched type III rocks D_V ranges between 0.18 and 0.3. Only in the strongly metamorphosed tuff sample 113380 has V been lost from olivine, resulting in D_V 0.07. In quenched andesite tuff sample 135961 D_V is estimated at around 0.40, whereas the re-equilibrated olivines from andesite lava sample 135962 give D_V about 0.15.

In conclusion, V partitioning between olivine and 'melt' in the investigated samples varies from 0.06 to 0.4, and appears to be distinctly f_{O_2}-sensitive. At f_{O_2}-levels characteristic of the regional volcanic rocks D_V is below 0.1. In the quenched type III and IV magmas D_V reaches about 0.2 to 0.4, but when such rocks have been re-equilibrated during cooling a substantial amount of V has been expelled from the olivine. The data on V partitioning seem to indicate that the Kûgánguaq Member magmas were characterized at quenching by f_{O_2} values intermediate between the IW buffer (Luciefjeld glass $D_V = 1.0$) and the NNO buffer (picrite glass, $D_V = 0.08$).

Chromium partitioning between olivine and glass has been investigated in model silicate melts by Schreiber (1979) and Schreiber & Haskin (1976), see also summary by Irving (1978). At low f_{O_2}, D_{Cr} olivine/glass is dominated by $D_{Cr^{2+}}$, and only slightly dependent on temperature and melt composition. At higher f_{O_2} the $D_{Cr^{3+}}$ contribution dominates on D_{Cr} total, and a considerable dependence on T, as well as on melt composition, is noted. Values for D_{Cr} total for olivine/glass pairs are crudely estimated in Table 28. Minimum values are obtained when the most magnesian olivine cores are paired with bulk rocks, because Cr was rapidly lost from the melt through the precipitation of chromite.

In some samples high-temperature metamorphic equilibration has depleted the olivine in Cr. In the picritic to FeTi basaltic glass samples estimated D_{Cr} values are around 1.2 to 1.5, these values being probably maximum estimates.

In type III samples D_{Cr} is estimated at 0.9 to 1.1 (which is also the level found in the iron-bearing Luciefjeld glass), and in the quenched type IV sample the value is 1.4. In conclusion, the partition coefficients D_{Cr} in the quenched type III samples are probably slightly lower than in the picritic to FeTi basaltic glasses, but do not in themselves provide a reliable estimate of f_{O_2}.

Estimation of f_{S_2}

Only very tiny blebs of immiscible sulphides have been found in the Kûgánguaq Member rocks, and none of these have been quantitatively analysed. Significantly, no trace of metallic iron is observed within these sulphides, such as described from tuffs from Nûgssuaq (Pedersen, 1978a) and the basalt glass from Luciefjeld (Pedersen, 1979b). In accordance with the evidence of f_{O_2} above the IW buffer, f_{S_2} must have been higher than the low level defined by an Fe–FeS type buffer (*c.* 10^{-5} at 1200°C, see Pedersen, 1979b). Evidence from strong Ni and Cu anomalies in type III and V samples shows that these magmas fractionated sulphides and were thus sulphide saturated. In the present samples the highest sulphur concentration is 0.06 wt.% found in the type III feeder dyke, while the analysed lava samples range between 0.04 and 0.01% S. Even these low levels are probably not a measure of the amount of primary sulphur retained in the rocks, since considerable parts of the observed sulphides are vug or vein filling low-temperature sulphide precipitates. The sulphur and oxygen fugacity seems therefore to have been high enough to allow extensive degassing of sulphide compounds such as is generally observed for terrestrial lavas (e.g. Moore & Fabbi, 1971), which contrasts with the high primary sulphide content preserved in metallic iron-bearing lavas and some of their xenoliths on Disko (0.15–0.78% S, Pedersen, 1979b, 1981). The highest primary sulphide concentrations found are in the mafic immiscible silicate blebs in type III and IV samples (0.35–0.85% S, Table 24) in accordance with the experimental evidence that sulphide solubility increases strongly with increasing Fe^{2+} in the silicate melt

(Haughton *et al.*, 1974). In conclusion f_{S_2} was high enough in the lavas to allow extensive degassing, and higher than the level determined by equilibrium with metallic iron, but no more precise estimates can be obtained from the present data.

Estimation of magma density

To estimate density contrasts between various uncontaminated and contaminated magmas in high-level crustal reservoirs the low pressure (1 atm.) densities have been calculated for rock and glass compositions after the method of Bottinga *et al.* (1982). A major uncertainty is the volatile content in the magma which is known to have a substantial effect on the densities. Magma densities increase markedly with increasing total dry pressure (e.g. Stolper *et al.*, 1981), but this effect has been neglected for the present purpose.

In accordance with the calculations given by Sparks *et al.* (1980) and Stolper & Walker (1980) on densities of basaltic melts, the picritic to olivine-poor tholeiitic basalts from Disko (Type I and II) gradually decrease in liquidus melt density with decreasing *mg* ratio, to a minimum represented by samples 113236 and 113328 with d = 2.68. With increasing iron and titanium the density gradually increases to 2.70–2.71 (sample 113330 and picrite glass 136943).

The Kûgánguaq Member melts are all markedly less dense than type I and II magmas and would float on top of the latter. The type III samples have melt densities in the range 2.63–2.64, and the melts representing their glass phases show similar values. Much lighter than these are the type IV rocks, which show liquidus melt densities ranging from 2.56 to 2.53, and which would definitely float on type III melts. The feldspar-phyric silicic basalts have similar densities to type III basalts (2.63).

From the calculated densities it can be concluded that once contaminated type III basalts formed from type I, they would accumulate in the roof zone of the chamber. Further, if magnesian andesites formed, they would definitely float on all other magmas observed. However, there is as yet no positive evidence for the existence of layered Kûgánguaq Member magma chambers.

Evidence from volcanic eruption forms

The Kûgánguaq Member volcanism deviates in eruption forms and lava morphology from the Naujánguit Member picrites, which were almost exclusively emplaced as pahoehoe lavas (except where erupted into shallow water) and which must have had a very low gas content. The type III basalt feeder dyke and its crater structure shows evidence of low ($\ll$ 100 bar) primary volatile pressure in the erupting magma which is considered typical for the majority of the type III rocks. The occurrence of tuff units in the central crater area forms an exception to this rule. Grain morphology shows that these tuffs were not erupted through phreatic

activity. The presence of well-defined achneliths is typical of Hawaiian to Strombolian type eruptions (Walker & Croasdale, 1972; Heiken, 1974), and the tuffs may therefore have been formed from lava fountains. However, the tuff morphology, and in particular the formation of a 3 m thick glass layer at the base, shows that they are neither normal agglutinates nor secondary lavas, but unusual minor ash flows. The small volumes involved and the small areal dispersal of the tuffs indicate that only a minor part of the type III basalt magma body became gas enriched. The mineral chemistry further shows that the gas enrichment did not change the f_{O_2} already established in the magma, or the change did not last long enough to re-equilibrate the minerals. It is likely that the gas enrichment took place in the contact zone to the contaminants from which the gasses were probably derived. Sandstones and siltstones from Disko commonly contain between 5 and 15% CO_2 (unpublished data), and low pressure reaction between such sediments and a basaltic magma would generate a carbon oxide rich gas phase, provided the sediments were poor in organic carbon. The triggering of an eruption from the top zone of such a magma/sediment contact could give rise to localized explosive activity. Most pyroclastic flows are thought to be generated from a collapsing Plinian eruption column (e.g. Sparks & Wilson, 1976; Sheridan, 1979), but no evidence of Plinian activity has been found.

The low horizontal mobility of the ash flow compared to other ash flows (e.g. Sheridan, 1979) could be due to combinations of (1) the small erupting volume, (2) the lower solubility of gas in basalts relative to more evolved magmas and (3) the much higher solidification temperatures for basalt compared to more acid magmas.

The type IV andesites show evidence of a low magmatic volatile pressure. The crater structures have not been localized but must be somewhere within the central crater area, and the scarcity of andesitic pyroclastic material here, together with lava morphology and petrography, show that the magmas must have been volatile poor. In conclusion, the reactions between magma and the crust only locally led to sufficient gas enrichment to allow explosive eruption, and less than 2 vol.% of the Kûgánguaq Member rocks erupted as pyroclastics.

COMPARISON AND FINAL CONCLUSIONS

In the preceding chapters the genesis of the Kûgánguaq Member type III and IV magmas has been narrowly constrained to a reaction between primitive picrite magmas and a quartz-rich crustal contaminant, for which a Mesozoic sandstone with some sulphur and minor organic carbon appears to be the most likely candidate. Published work on shale xenoliths from Disko (e.g. Melson & Switzer, 1966; Pedersen, 1979a) has shown that the magma-shale sediment reactions cannot be described as simple mixing of components, but involve extensive equilibration reactions at the magma–xenolith contacts. More detailed modelling of the process leading to the formation of the Kûgánguaq Member rocks, which almost certainly involved selective contamination (Watson, 1982), is not justified until detailed data on sandstone and siltstone xenoliths from Disko have been obtained, and until a parallel study of the related predominantly shale-contaminated, volcanic rocks from the Asuk Member has been carried out.

The Kûgánguaq Member type III and IV rocks are unlike any modern igneous rocks produced at constructive plate margins (e.g. Melson *et al.*, 1976; Sigurdsson, 1981; Clague *et al.*, 1981). However, they show considerable similarities to rocks from two associations: (a) the boninite suite and high Mg andesites, (b) the high-Mg continental dolerites.

(a) The magnesian basaltic to dacitic rocks collectively termed the boninite suite have been reviewed by Cameron & Nisbet (1982) and Hickey & Frey (1982). The very different tectonic environment, distinctly different trace element composition (Hickey & Frey, 1982) and the more hydrous nature of the boninites (Walker & Cameron, 1983) make it unlikely that the Kûgánguaq Member rocks are genetically related to the boninites.

(b) High-Mg continental dolerites are found associated with the Bushveld complex (Davies *et al.*, 1980; Cawthorn *et al.*, 1981; Sharpe, 1981) and are believed to represent one of the two parental melts which formed that gigantic complex (Cawthorn & Davies, 1983). Comparable in a general sense to Kûgánguaq Member type III rocks are also such continental dolerites as the Antarctic diabases described by Hamilton (1965) and the Tasmanian dolerites studied by McDougall (1962) and Compton *et al.* (1968). These continental dolerites are considered to have been contaminated by material from the continental crust (e.g. Philpotts & Schnetzler, 1968; Faure *et al.*, 1974). The Kûgánguaq Member type III and IV rocks are of considerable interest in this context because they provide an indisputable example of the production of high-Mg silicic basalts and magnesian andesites from picritic parents through reaction with continental crust, and the example is strengthened by

their field occurrence as a minor sequence of contaminated lavas enclosed in a major series of picritic parental type lavas.

Finally, this study has demonstrated that the partition of the redox-sensitive lithophile transition metals Cr and V between glass, olivine and chromite can distinguish redox-levels in quenched Vaigat Formation rocks. This will make possible future estimates of indigenous reducing properties in crustal contaminants in many of the contaminated lava series in West Greenland, and thus allow the recognition of whether granite/gneiss, sandstone/siltstone or shale contaminations were dominant in the crustal reservoirs.

Acknowledgements

I am grateful to H. Bollingberg, M. Mouritzen and I. Sørensen for the chemical analyses, to S. Pedersen for Sr-isotope determinations, to J. C. Bailey for help with the trace element analyses and to P. G. Hill and N. G. Ware for help with the microprobe work. Thanks are due to the Research School of Earth Sciences, Canberra, to the Geological Museum, Oslo and to the Danish Natural Science Research Council for providing laboratory facilities. I am particularly grateful to J. G. Rønsbo for valuable help and discussions on microprobe analyses of major and trace elements and to A. Noe-Nygaard, F. Kalsbeek, L. M. Larsen, F. Ulff-Møller, and J. R. Wilson for constructive criticism of the manuscript. R. Larsen drafted the figures and A. K. Brantsen typed the manuscript. The project was carried out in close cooperation with the Geological Survey of Greenland.

REFERENCES

Andersen, O. 1915: The system anorthosite–forsterite–silica. *Amer. J. Sci.* **39,** 407–454.

Bird, J. M., Goodrich, C. A. & Weathers, M. S. 1981: Petrogenesis of Uivfaq iron, Disko Island, Greenland. *J. geophys. Res.* **86,** 11787–11805.

Bottinga, Y., Richet, P. & Weill, D. F. 1983: Calculation of the density and thermal expansion coefficient of silicate liquids. *Bull. Minéral.* **106,** 129–138.

Bottinga, Y., Weill, D. & Richet, P. 1982: Density calculations for silicate liquids. I. Revised method for aluminosilicate compositions. *Geochim. cosmochim. Acta* **46,** 909–919.

Boyd, F. R., England, J. L. & Davis, B. T. C. 1964: Effects of pressure on the melting and polymorphism of enstatite, $MgSiO_3$. *J. geophys. Res.* **69,** 2101–2109.

Brooks, C. K. 1976: The Fe_2O_3/FeO ratio of basalt analyses: an appeal for a standardized procedure. *Bull. geol. Soc. Denmark* **25,** 117–120.

Brunfelt, A. O. & Steinnes, E. 1969: Instrumental activation analysis of silicate rocks with epithermal neutrons. *Anal. Chim. Acta* **48,** 13–24.

Buddington, A. F. & Lindsley, D. H. 1964: Iron-titanium oxide minerals and synthetic equivalents. *J. Petrol.* **5,** 310–357.

Buseck, P. R. 1977: Pallasite meteorites – mineralogy, petrology and geochemistry. *Geochim. cosmochim. Acta* **41,** 711–740.

Bøggild, O. B. 1953: The mineralogy of Greenland. *Meddr Grønland* **149**(3), 442 pp.

Böhlke, J. K., Honnores, J. & Honnores-Guerstein, B.-M. 1980: Alteration of basalts from Site 396B, DSDP: Petrographic and mineralogic studies. *Contr. Miner. Petrol.* **73,** 341–364.

Cameron, W. E. & Nisbet, E. G. 1982: Phanerozoic analogues of komatiitic basalts. *In* Arndt, N. T. & Nisbet, E. G. (edit.) *Komatiites,* 29–50. London: George Allen & Unwin.

Carmichael, I. S. E. 1964: The petrology of Thingmuli, a Tertiary volcano in eastern Iceland. *J. Petrol.* **5,** 435–460.

Cawthorn, R. G. & Davies, G. 1983: Experimental data at 3 kbars pressure on parental magma to the Bushveld Complex. *Contr. Miner. Petrol.* **83,** 128–135.

Cawthorn, R. G., Davies, G., Clubley-Armstrong, A. & McCarthy, T. S. 1981: Sills associated with the Bushveld Complex, South Africa: an estimate of the parental magma composition. *Lithos* **14,** 1–16.

Chen, C. H. & Presnall, D. C. 1975: The system Mg_2SiO_4–SiO_2 at pressures up to 25 kilobars. *Amer. Miner.* **60,** 398–406.

Chinner, G. A. & Shairer, J. F. 1962: The join $Ca_3Al_2Si_3O_{12}$ – $Mg_3Al_2Si_3O_{12}$ and its bearing on the system CaO–MgO–Al_2O_3–SiO_2 at atmospheric pressure. *Amer. J. Sci.* **260,** 611–634.

Clague, D. A., Frey, F. A., Thompson, G. & Rindge, S. 1981: Minor and trace element geochemistry of volcanic rocks dredged from the Galapagos Spreading Center: role of crystal fractionation and mantle heterogeneity. *J. geophys. Res.* **86,** 9469–9482.

Clarke, D. B. 1970: Tertiary basalts of Baffin Bay: possible primary magma from the mantle. *Contr. Miner. Petrol.* **25,** 203–224.

Clarke, D. B. & Pedersen, A. K. 1976: Tertiary volcanic province of West Greenland. *In* Escher, A. & Watt, W. S. (edit.) *Geology of Greenland,* 365–385. Copenhagen: Geol. Surv. Greenland.

Clark, D. B. & Upton, B. G. J. 1971: Tertiary basalts of Baffin Bay: field relations and tectonic setting. *Can. J. Earth Sci.* **8,** 248–258.

Compton, W., McDougall, I. & Heier, K. S. 1968: Geochemical comparison of the Mesozoic basaltic rocks of Antarctica, South Africa and Tasmania. *Geochim. cosmochim. Acta* **32,** 129–149.

Davies, G., Cawthorn, R. G., Barton, J. M. & Morton, M. 1980: Parental magma to the Bushveld Complex. *Nature* **287,** 33–35.

Denham, L. R 1974: Offshore geology of northern West Greenland (69°N to 75°N). *Rapp. Grønlands geol. Unders.* **63,** 24 pp.

Elder, J. W. 1975: A seismic and gravity study of the western part of the Cretaceous–Tertiary sediments of central West Greenland. *Rapp. Grønlands. geol. Unders.* **69,** 5–9.

Evensen, N. M., Hamilton, P. J. & O'Nions, R. K. 1978: Rare earth abundances in chondritic meteorites. *Geochim. cosmochim. Acta* **42,** 1199–1212.

Faure, G., Bowman, J. R., Elliot, D. H. & Jones, L. M. 1974: Strontium isotope composition and petrogenesis of the Kirkpatrick Basalt, Queen Alexandra Range, Antarctica. *Contr. Miner. Petrol.* **48,** 153–169.

Ford, C. E., Russell, D. G., Craven, J. A. & Fisk, M. R. 1983: Olivine–liquid equilibria: temperature, pressure and composition dependence of the crystal/liquid cation partition coefficients for Mg, Fe^{2+}, Ca and Mn. *J. Petrol.* **24,** 256–265.

GGU 1976: Geologisk kort over Grønland 1: 100 000, Qutdligssat 70 V. 1 Syd. Copenhagen: Grønlands geologiske Undersøgelse.

Goldschmidt, V. M. 1954: *Geochemistry.* Oxford: Clarendon Press. 730 pp.

Goodrich, C. A. 1983: Phosphoran pyroxene and olivine in silicate inclusions in natural iron-carbon alloy from Uivfaq, Disko Island, Greenland. *EOS* **64,**(45), 903 only.

Goodrich, C. A. 1984: Phosphoran pyroxene and olivine in silicate inclusions in natural iron-carbon alloy, Disko Island, Greenland. *Geochim. cosmochim. Acta* **48,** 1115–1126.

Gordon, G. E., Randle, K., Coles, G. G., Corliss, J. B., Beeson, M. H., Oxley, S. S. 1968: Instrumental activation analysis of standard rocks with high resolution X-ray detectors. *Geochim. cosmochim. Acta* **32,** 369–396.

Hamilton, W. 1965: Diabase sheets of the Taylor Glacier region, Victoria Land, Antarctica. *U.S. Geol. Surv. Prof. Pap.* **465-B,** 1–71.

Haughton, D. R., Roeder, P. L. & Skinner, B. J. 1974: Solubility of sulfur in mafic magmas. *Econ. Geol.* **69,** 451–467.

Heiken, G. 1974: An atlas of volcanic ash. *Smithsonian Contr. Earth Sci.* **12,** 101 pp.

Henderson, G., Rosenkrantz, A. & Schiener, E. J. 1976: Cretaceous – Tertiary sedimentary rocks of West Greenland. *In* Escher, A. & Watt, W. S. (edit.) *Geology of Greenland,* 340–362. Copenhagen: Geol. Surv. Greenland.

Henderson, G., Schiener, E. J., Risum. J. B., Croxton, C. A. & Andersen, B. B. 1981: The West Greenland basin. *Can. Soc. Petrol. Geol. Mem.* **7,** 399–428.

Hickey, R. L. & Frey, F. A. 1982: Geochemical characteristics of boninite series volcanics: implications for their source. *Geochim. cosmochim. Acta* **46,** 2099–2115.

Hill, R. E. T. & Roeder, P. L. 1974: The crystallization of spinel from liquid as a function of oxygen pressure. *J. Geol.* **82,** 709–729.

Irvine, T. N. 1970: Crystallization sequences in the Muskox intrusion and other layered intrusions. I: Olivine-pyroxene-plagioclase relations. *Spec. Publs geol. Soc. S. Africa* **1,** 441–476.

Irvine, T. N. 1975a: Olivine-pyroxene-plagioclase relations in the system Mg_2SiO_2–$CaAl_2Si_2O_8$–$KAlSi_3O_8$–SiO_2 and their bearing on the differentiation of stratiform intrusions. *Yb. Carnegie Instn Wash.* **74,** 492–500.

Irvine, T. N. 1975b: Primary precipitation of concentrated deposits of magmatic ores. *Pap. geol. Surv. Can.* **75-1,** Part B, 73–79.

Irvine, T. N. 1979: Rocks whose competition is determined by crystal accumulation and sorting. *In* Yoder, H. S. (edit.) *The evolution of the igneous rocks. Fiftieth anniversary perspectives.* Princeton University Press. 588 pp.

Irving, A. J. 1978: A review of experimental studies of crystal/liquid trace element partitioning. *Geochim. cosmochim. Acta* **42,** 743–770.

Kilinc, A., Carmichael, I. S. E., Rivers, M. L. & Sack, R. O. 1983: The ferric-ferrous ratio of natural silicate liquids equilibrated in air. *Contr. Miner. Petrol.* **83,** 136–140.

Kushiro, I. 1972: Effects of water on the composition of magmas formed at high pressures. *J. Petrol.* **13,** 311–334.

Lindstrom, D. J. 1976: Experimental study of the partitioning of the transition metals between clinopyroxene and coexisting silicate liquids. Ph.D. Thesis, University of Oregon, 188 pp.

Macdonald, G. C. & Katsura, T. 1964: Chemical composition of Hawaiian lavas. *J. Petrol.* **5,** 82–133.

Maurel, C. & Maurel, P. 1982a: Étude expérimentale de la solubilité de chrome dans les bains silicatés basiques et de sa distribution entre liquide et minéraux coexistants: conditions d'existence du spinelle chromifère. *Bull. Minéral.* **105,** 640–647.

Maurel, C. & Maurel, P. 1982b: Étude expérimentale de l'équilibre Fe^{2+}–Fe^{3+} dans les spinelles chromifères et les liquides silicatés basiques coexistants, à 1 atm. *C.r. hebd. Séanc. Acad. Sci. Paris* **295,** Sér. 2, 209–212.

McDougall, I. 1962: Differentiation of the Tasmanian dolerites: Red Hill dolerite-granophyre association. *Bull. geol. Soc. Amer.* **73,** 279–316.

Medenbach, O. & El Goresy, A. 1982: Ulvöspinel in native iron-bearing assemblages and the origin of these assemblages in basalts from Ovifak, Greenland, and Bühl, Federal Republic of Germany. *Contr. Miner. Petrol.* **80,** 358–366.

Melson, W. G. & Switzer, G. 1966: Plagioclase-spinel-graphite xenoliths in metallic iron-bearing basalt, Disko Island, Greenland. *Amer. Miner.* **51,** 664–676.

Melson, W. G., Vallier, T. L., Wright, T. L., Byerly, G. & Nelen, J. 1976: Chemical diversity of abyssal volcanic glass erupted along Pacific, Atlantic and Indian Ocean sea floor spreading centers. *In* Sutton, G. H., Manghani, M. H. & Moberly, R. (edit.) *Geophysics of the Pacific Ocean Basin. Amer. geophys. Un. Monogr.* **19,** 351–367.

Moore, J. G. & Fabbi, B. P. 1971: An estimate of the juvenile sulfur content of basalt. *Contr. Miner. Petrol.* **33,** 118–127.

Morse, S. A. 1980: *Basalts and phase diagrams.* New York: Springer-Verlag.493 pp.

O'Nions, R. K. & Clarke, D. B. 1972: Comparative trace element geochemistry of Tertiary basalts from Baffin Bay. *Earth planet. Sci. Lett.* **15,** 436–446.

Pálmason, G., Arnórsson, S., Friedleifsson, I. B., Krismannsdóttir, H., Saemundsson, K., Stefánsson, V., Steingrimsson, B., Tómasson, J. & Kristjánsson, L. 1979: The Iceland crust: evidence from drill hole data on structure and processes. *In* Talwani, M., Harrison, C. G. & Hayes, D. E. (edit.) *Deep drilling results in the Atlantic Ocean crust,* 43–65, Maurice Ewing Series 2, American Geophysical Union.

Pauly, H. 1969: White cast iron with cohenite, schreibersite and sulphides from Tertiary basalts on Disko, Greenland. *Meddr dansk geol. Foren.* **19,** 8–26.

Pedersen, A. K. 1973: Report on field work along the north coast of Disko, 1971. *Rapp. Grønlands geol. Unders.* **53,** 21–27.

Pedersen, A. K. 1975: New investigations of the native iron bearing volcanic rocks of Disko, central West Greenland. *Rapp. Grønlands geol. Unders.* **75,** 48–51.

Pedersen, A. K. 1977a: Dyke intrusions along the south coast of Disko. *Rapp. Grønlands geol. Unders.* **81,** 57–67.

Pedersen, A. K. 1977b: Tertiary volcanic geology of the Mellemfjord area, south-west Disko. *Rapp. Grønlands geol. Unders.* **81,** 35–51.

Pedersen, A. K. 1978a: Graphite andesite tuffs resulting from high-Mg tholeiite and sediment interaction; Nûgssuaq, West Greenland. *Bull. geol. Soc. Denmark* **27,** Spec. Iss., 117–130.

Pedersen, A. K. 1978b: Non-stoichiometric magnesian spinels in shale xenoliths from a native iron-bearing andesite at Asuk, Disko, central West Greenland. *Contr. Miner. Petrol.* **67,** 331–340.

Pedersen, A. K. 1979a: A shale buchite xenolith with Al-armalcolite and native iron in a lava from Asuk, Disko, central West Greenland. *Contr. Miner. Petrol.* **69,** 83–94.

Pedersen, A. K. 1979b: Basaltic glass with high-temperature equilibrated immiscible sulphide bodies with native iron from Disko, central West Greenland. *Contr. Miner. Petrol.* **69,** 397–407.

Pedersen, A. K. 1981: Armalcolite-bearing Fe-Ti oxide assemblages in graphite-equilibrated salic volcanic rocks with native iron from Disko, central West Greenland. *Contr. Miner. Petrol.* **77,** 307–324.

Pedersen, A. K. 1985: Lithostratigraphy of the Tertiary Vaigat Formation on Disko, central West Greenland. *Rapp. Grønlands geol. Unders.* **124,** 30 pp.

Philpotts, A. R. 1979: Silicate liquid immiscibility in tholeiitic basalts. *J. Petrol.* **20,** 99–118.

Philpotts, A. R. 1982: Composition of immiscible liquids in volcanic rocks. *Contr. Miner. Petrol.* **80,** 201–218.

Roedder, E. 1978: Silicate liquid immiscibility in magmas and in the system K_2O–FeO–Al_2O_3–SiO_2: an example of serendipity. *Geochim. cosmochim. Acta* **42,** 1597–1617.

Roedder, E. & Weiblen, P. W. 1971: Petrology of silicate melt inclusions Apollo 11 and Apollo 12 and terrestrial equivalents. Proc. Second Lunar Sci. Conf., *Geochim. cosmochim. Acta, Suppl. 2,* **1,** 507–528.

Roedder, E. & Weiblen, P. W. 1972: Petrographic features and petrologic significance of melt inclusions in Apollo 14 and 15 rocks. *Proc. Third Lunar Sci. Conf.* **1,** 251–279.

Roeder, P. L. 1974: Activity of iron and olivine solubility in basaltic liquids. *Earth planet. Sci. Lett.* **23,** 397–410.

Roeder, P. L. 1982: Experimental study of chromite-basaltic liquid equilibrium. Abstract 94. *In: Generation of major basalt types,* IAVCET-IAGC Scientific Assembly, Reykjavik, Iceland 1982.

Roeder, P. L. & Emslie, R. F. 1970: Olivine-liquid equilibrium. *Contr. Miner. Petrol.* **29,** 275–289.

Sack, R. O., Carmichael, I. S. E., Rivers, M. & Ghiorso, M. S. 1980: Ferric-ferrous equilibria in natural silicate liquids at 1 bar. *Contr. Miner. Petrol.* **75,** 369–376.

Schreiber, H. D. 1977: Redox states of Ti, Zr, Hf, Cr, and Eu in basaltic magmas: an experimental study. *Proc. 8th Lunar Sci. Conf.* 1785–1807.

Schreiber, H. D. 1979: Experimental studies of nickel and chromium partitioning into olivine from synthetic basaltic melts. *Proc. 10th Lunar Planet. Sci. Conf.* 509–516.

Schreiber, H. D., Balazs, G. B., Schaffer, A. P. & Jamison, P. L. 1982: Iron metal production in silicate melts through the direct reduction of Fe(II) by Ti(III), Cr(II), and Eu(II). *Geochim. cosmochim. Acta* **46,** 1891–1901.

Schreiber, H. D. & Haskin, L. A. 1976: Chromium in basalts: experimental determination of redox states and partitioning among synthetic silicate phases. *Proc. 7th Lunar Sci. Conf.* 1221–1259.

Sharpe, M. R. 1981: The chronology of magma influxes to the eastern compartment of the Bushveld Complex as exemplified by its marginal border groups. *J. geol. Soc. Lond.* **138,** 307–326.

Sheridan, M. F. 1979: Emplacement of pyroclastic flows: a review. *Geol. Soc. Am. Spec. Pap.* **180,** 125–136.

Shervais, J. W. 1982: Ti–V plots and the petrogenesis of modern and ophiolitic lavas. *Earth planet. Sci. Lett.* **59,** 101–118.

Sigurdsson, H. 1981: First-order major element variation in basalt glasses from the Mid-Atlantic Ridge: 29°N to 73°N. *J. geophys. Res.* **86,** 9483–9502.

Solomon, M. 1963: Counting and sampling errors in modal analysis by point counter. *J. Petrol.* **4,** 367–382.

Sparks, R. S. J., Meyer, P. & Sigurdsson, H. 1980: Density variation amongst mid-ocean ridge basalts: implications for magma mixing and the scarcity of primitive lavas. *Earth planet. Sci. Lett.* **46,** 419–430.

Sparks, R. S. J. & Wilson, L. 1976: A model for the formation of ignimbrite by gravitational column collapse. *J. geol. Soc. London* **132,** 441–452.

Spencer, K. J. & Lindsley, D. H. 1981: A solution model for coexisting iron-titanium oxides. *Am. Miner.* **66,** 1189–1201.

Stolper, E. 1980: A phase diagram for Mid-Ocean ridge basalts: preliminary results and implications for petrogenesis. *Contr. Miner. Petrol.* **74,** 12–27.

Stolper, E. & Walker, D. 1980: Melt density and the average composition of basalt. *Contr. Miner. Petrol.* **74,** 1–12.

Stolper, E., Walker, D. Hager, B. H. & Hays, J. F. 1981: Melt segregation from partially molten source regions: the importance of melt density and source region size. *J. geophys. Res.* **86,** 6261–6271.

Sørensen, I. 1975: X-ray fluorescence spectroscopy at GGU. *Rapp. Grønlands geol. Unders.* **75,** 16–18.

Törnebohm, A. E. 1978: Über die eisenführenden Gesteine von Oivfaq und Assuk in Grönland. *Bih. K. Svenska. VetenskAkad. Handl.* **4**(10), 1–22.

van der Linden, W. J. M. 1975: Crustal attenuation and sea-floor spreading in the Labrador Sea. *Earth planet. Sci. Lett.* **27,** 409–423.

Walker, D. A. & Cameron, W. E. 1983: Boninite primary magmas: evidence from the Cape Vogel Peninsula, PNG. *Contr. Miner. Petrol.* **83,** 150–158.

Walker, D., Shibata, T. & Delong, S. E. 1979: Abyssal tholeiites from the Oceanographer Fracture Zone II. Phase equilibria and mixing. *Contr. Miner. Petrol.* **70,** 111–125.

Walker, G. P. L. & Croasdale, R. 1972: Characteristics of some basaltic pyroclastics. *Bull. volcanol.* **35,** 303–317.

Watson, E. B. 1982: Basalt contamination by continental crust: some experiments and models. *Contr. Miner. Petrol.* **80,** 73–87.

Weaver, C. E. & Pollard, L. D. 1973: *The chemistry of clay minerals.* Dev. Sedimentology 15. Amsterdam: Elsevier, 213 pp.

ISSN 0105 3507

AiO Print Ltd., Odense, Denmark